**Title**

Light-Mediated Control of Polymeric Materials

**Author**

Dolinski, Neil D

**Publication Date**

2019

UNIVERSITY OF CALIFORNIA

Santa Barbara

# Light-Mediated Control of Polymeric Materials

A dissertation submitted in partial satisfaction of the
requirements for the degree Doctor of Philosophy
in Materials

by

Neil D. Dolinski

Committee in charge:

Professor Craig Hawker, Chair

Professor Michael Chabinyc

Professor Glenn Fredrickson

Professor Javier Read de Alaniz

Professor Omar Saleh

March 2019

The dissertation of Neil D. Dolinski is approved.

Michael Chabinyc

Glenn Fredrickson

Javier Read de Alaniz

Omar Saleh

Craig Hawker, Committee Chair

February 2019

# ACKNOWLEDGEMENTS

The work presented in this thesis was a result of several highly collaborative efforts stemming from the Materials Research Laboratory at UCSB, as such I would like to thank my coauthors, listed here:

**Chapter 2:** Zachariah Page, Fabian Eisenreich, Jia Niu, Stefan Hecht, Javier Read de Alaniz, and Craig Hawker

**Chapter 3:** Zachariah Page, Emre Discekici, David Meis, In-Hwan Lee, Glen Jones, Richard Whitfield, Xiangcheng Pan, Blaine McCarthy, Sivaprakash Shanmugam, Veronika Kottisch, Brett Fors, Cyrille Boyer, Garret Miyake, Krzysztof Matyjaszewski, David Haddleton, Javier Read de Alaniz, Athina Anastasaki, and Craig Hawker

**Chapter 4:** Zachariah Page, Ben Callaway, Fabian Eisenreich, Ronnie Garcia, Roberto Chavez, David Bothman, Stefan Hecht, Frank Zok, and Craig Hawker

Of course, I thank all coauthors for other works not featured in this thesis as well as all members of the Hawker group past and present who were always a great source of inspiration and support. Specifically, I would like to acknowledge the input (and friendship) of Zak Page, who was my constant partner in crime in the lab.

I would also like to thank my friends and family, who were always ready to listen and help out whenever they could.

Finally, I would like to thank Craig for giving me the chance to succeed and for serving as an excellent mentor, I couldn’t have asked for a better advisor.

# VITA OF NEIL DOLINSKI

February 2019

## EDUCATION

| | |
|---|---|
| 2013 – 2019 | **University of California Santa Barbara**: Santa Barbara, CA<br>PhD Candidate in Materials (Advisor: Craig Hawker) |
| 2009 – 2013 | **Rutgers University**: New Brunswick, NJ<br>BS Materials Science and Engineering (Advisor: Laura Fabris) |

## PROFESSIONAL EMPLOYMENT

| | |
|---|---|
| 2013 – Present | **GSR**: University of California Santa Barbara<br>Materials Research Lab / California Nanosystems Institute<br>Advisor: Prof. Craig Hawker<br>*photopolymerization, photochromic dyes, in-situ kinetics, polymer gels, polymer rheology, additive manufacturing* |
| 2010 – 2013 | **Undergraduate Research Assistant**: Rutgers University<br>Materials Science and Engineering Department<br>Advisor: Prof. Laura Fabris<br>*morphology control of gold nanoparticles, ligand exchange* |

## PUBLICATIONS

(10) Kaminker, Revital; Callaway, E. Benjamin; **Dolinski, Neil D.**; Barbon, Stephanie M.; Shibata, Masashi; Wang, Hengbin; Hu, Jerry; Hawker, Craig J.* "Solvent-free synthesis of high-performance polyhexahydrotriazine (PHT) thermosets" *Chemistry of* Materials, **2018**, *30*, 8352–8358. DOI:10.1021/acs.chemmater.8b03926

(9) **Dolinski, Neil D.**; Page, Zachariah A.; Discekici, Emre H.; Lee, In-Hwan; Meis, David; Jones, Glen R.; Whitfield, Richard; Pan, Xiangcheng; McCarthy, Blaine G.; Shanmugam, Sivaprakash; Kottisch, Veronika; Fors, Brett P.; Boyer, Cyrille; Miyake, Garret M.; Matyjaszewski, Krzysztof; Haddleton, David M.; Read de Alaniz, Javier; Anastasaki, Athina*; Hawker, Craig J.* "What happens in the dark? Assessing the temporal control of state-of-the-art photo-mediated controlled radical polymerizations." *Journal of Polymer Science Part A: Polymer Chemistry*, **2018**, *57*, 268–273. DOI:10.1002/pola.29247

(8) Narupai, Benjaporn; Page, Zachariah A.; Treat, Nicolas J.; McGrath, Alaina J.; Pester, Christian W.; Discekici, Emre H.; **Dolinski, Neil D.**; Meyers, Gregory F.; Read de Alaniz, Javier; Hawker, Craig J.* "Simultaneous Preparation of Multiple Polymer Brushes under Ambient Conditions using μL Volumes" *Angewandte Chemie Int. Ed.*, **2018**, *57*, 13433–13438. DOI:10.1002/anie.201805534

(7) Hemmer, James R.; Page, Zachariah A.; Clark, Kyle D.; Stricker, Friedrich; **Dolinski, Neil D.**; Hawker, Craig J.; Read de Alaniz, Javier* "Controlling Dark Equilibria and Enhancing DASA Photoswitching Properties Through Carbon Acid Design" *Journal of the American Chemical Society*, **2018**, *140*, 10425–10429. DOI:10.1021/jacs.8b06067

(6) Self, Jeffrey L.; **Dolinski, Neil D.**; Zayas, Manuel S.; Read de Alaniz, Javier; Bates, Christopher M.* "Brønsted-Acid-Catalyzed Exchange in Polyester Dynamic Covalent Networks" *ACS Macro Letters*, **2018**, *7*, 817–821. DOI:10.1021/acsmacrolett.8b00370

(5) **Dolinski, Neil D.**; Page, Zachariah A.; Callaway, E. Benjamin; Eisenreich, Fabian; Garcia, Ronnie V.; Chavez, Roberto; Bothman, David P.; Hecht, Stefan; Zok, Frank W.; Hawker, Craig J.* "Solution Mask Liquid Lithography (SMaLL) for One-Step, Multi-Material 3D Printing." *Advanced Materials*, **2018**, *30*, 1800364. DOI:10.1002/adma.201800364

(4) Niu, Jia; Page, Zachariah A.; **Dolinski, Neil D.**; Anastasaki, Athina; Hsueh, Andy T.; Soh, H. Tom; Hawker, Craig J.* "Rapid Visible Light-Mediated Controlled Aqueous Polymerization with *in situ* Monitoring." *ACS Macro Letters*, **2017**, *6*, 1109–1113. DOI:10.1021/acsmacrolett.7b00587

(3) Ulrich, Sebastian†; Hemmer, James R.†; Page, Zachariah A.; **Dolinski, Neil D.**; Rifaie-Graham, Omar; Bruns, Nico; Hawker, Craig J.; Boesel, Luciano F.*; Read de Alaniz, Javier*. "Visible Light-Responsive DASA-Polymer Conjugates." *ACS Macro Letters*, **2017**, *6*, 738–742. DOI:10.1021/acsmacrolett.7b00350

(2) **Dolinski, Neil D.**†; Page, Zachariah A.*†; Eisenreich, Fabian; Niu, Jia; Hecht, Stefan; Read de Alaniz, Javier; Hawker, Craig J.* "A Versatile Approach for in situ Monitoring of Photoswitches and Photopolymerizations using NMR Spectroscopy." *ChemPhotoChem*, **2017**, *1*, 125–131. DOI:10.1002/cptc.201600045

(1) Hemmer, James R.; Poelma, Saemi O.; Treat, Nicolas; Page, Zachariah A.; **Dolinski, Neil D.**; Diaz, Yvonne J.; Tomlinson, Warren; Clark, Kyle D.; Hooper, Joseph P.; Hawker, Craig J.; Read de Alaniz, Javier*. "Tunable Visible and Near Infrared Photoswitches." *Journal of the American Chemical Society*, **2016**, *138*, 13960–13966. DOI:10.1021/jacs.6b07434

## AWARDS

| | |
|---|---|
| 2018 | Doctoral Student Travel Grant, *UCSB Academic Senate* |
| 2018 | Runner-up Grad Slam, *UCSB Graduate Division* |
| 2017 | CSP Technologies Fellowship in Polymer Research |
| 2017/2018 | Ed Kramer Award for Best Poster Presentation,<br>Materials Research Outreach Program, *MRL UCSB* (x2) |
| 2017/2018/2019 | Dow Materials Institute Travel Fellowship, *MRL UCSB* |
| 2016 | Outstanding Poster Award, *American Chemical Society POLY Division*, ACS National Meeting San Diego |
| 2015 | Interdisciplinary Research Group-I Research Fellowship, *MRL UCSB* |

## FIELD OF STUDY

Major Field: Materials
Studies in Photochemical Approaches to Polymerization with Professor Craig J. Hawker

# ABSTRACT

## Light-Mediated Control of Polymeric Materials

by

Neil D. Dolinski

The synthesis and characterization of precision polymeric materials represents a broad research area with significant value to society. Recently, light-mediated approaches to controlled polymer synthesis have attracted significant interest due to the low cost and tremendous tunability of modern light sources. Through manipulating these various properties (wavelength, intensity, etc), researchers have made considerable progress in controlling a wide range of important polymeric properties such as molecular weight distribution, comonomer composition, and molecular architecture. However, the systems developed to date have largely focused on homogenous targets and have lacked in-depth photophysical interpretation. This dissertation describes the development of an *in-situ* approach to studying light-mediated chemical reactions and efforts to better understand the temporal control of state-of-the-art photopolymerizations. Furthermore, the lessons learned from these studies led to the development of a new approach to 3D printing, wherein specific wavelengths of visible light were used to independently and simultaneously define local materials properties throughout a part in a single step. This breakthrough in additive manufacturing greatly expands the potential of multi-material printing techniques. The findings of these works have broad implications for using light as a tool for the future development of synthetic approaches to advanced polymeric materials.

# TABLE OF CONTENTS

# Chapter 1: Introduction

## Light as a Tool for Synthesis

The use of light as a powerful stimulus to impact properties has been broadly implemented throughout materials chemistry across a wide range of fields. Of particular note is the sustained interest of light as a stimulus for the production and manipulation of soft materials systems, with applications spanning lithography,[1,2] drug delivery,[3,4] adaptable gels,[5,6] and even in the synthesis of well-defined polymer chains.[7,8] The continued interest in photo-controlled approaches to soft materials is largely due to the low cost, tunability, and wide availability of light sources available to researchers. Even in applications where materials could be synthesized through traditional thermally-driven approaches, as in the synthesis of polymers with well-defined molecular weights, light offers new possibilities in terms of its spatiotemporal control, allowing for the development of new materials like patterned polymer brushes with intensity-controlled surface features.[9]

This chapter highlights a variety of background information for key light-driven chemistries, forming a foundation for the work described in Chapters 2–4. Each section serves to recount recent developments in the field, and to give the reader a baseline understanding of the unifying principles presented in the literature. In particular, this chapter covers the basic concepts of photochromic molecules with applications in soft materials systems, the development of photo-mediated controlled radical polymerizations, and the use of light in additive manufacturing.

### Photochromic dyes and Donor Acceptor Stenhouse Adducts

Photochromic dyes, also known as photoswitches, are an interesting class of compounds whose optical properties (color/absorbance) can be manipulated through exposure to light, which induces a change in molecular structure.[10] The primary use for photochromic molecules industrially has been for the production of light-responsive lenses that selectively darken upon exposure to light, typically exposure to the UV component of sunlight inducing lens darkening.[11] However, as this class of molecules has developed, the potential applications of photochromic dyes have expanded dramatically. Some particularly impressive examples have utilized photochromic molecules as chemical sensors,[12] molecular motors,[13] handles for monitoring stress,[14] polymerization catalysts,[15,16] and drug delivery agents.[17] The key characteristic of photoswitches that have enabled their use in these applications is the large change in properties (volume, solubility, charge, *etc*) that occurs during isomerization. This section will discuss the fundamental properties of photochromic molecules and introduce select classes of photochromic dyes of particular importance to this thesis.

Photochromic molecules can be broadly divided into two classes, P-type and T-type, which describe the transition between their isomers. The first of these classes, P-type photoswitches, only undergo isomerization through exposure to light and remain stable in either isomeric form. In contrast, T-type molecules will change in color when exposed to a suitable set of wavelengths but will fade back to their initial state with time. For simplicity in this thesis, even if isomerization can be facilitated by light in both directions, if there is a thermal pathway between states a switch is said to be T-type. Examples of both classes can be seen in **Figure 1.1**, where T-type molecules are denoted by a Δ along one of the reaction arrows. Interestingly, when a photochromic molecule has a stable isomer in the conjugated colored form, the molecule is said to exhibit negative photochromism.[18]

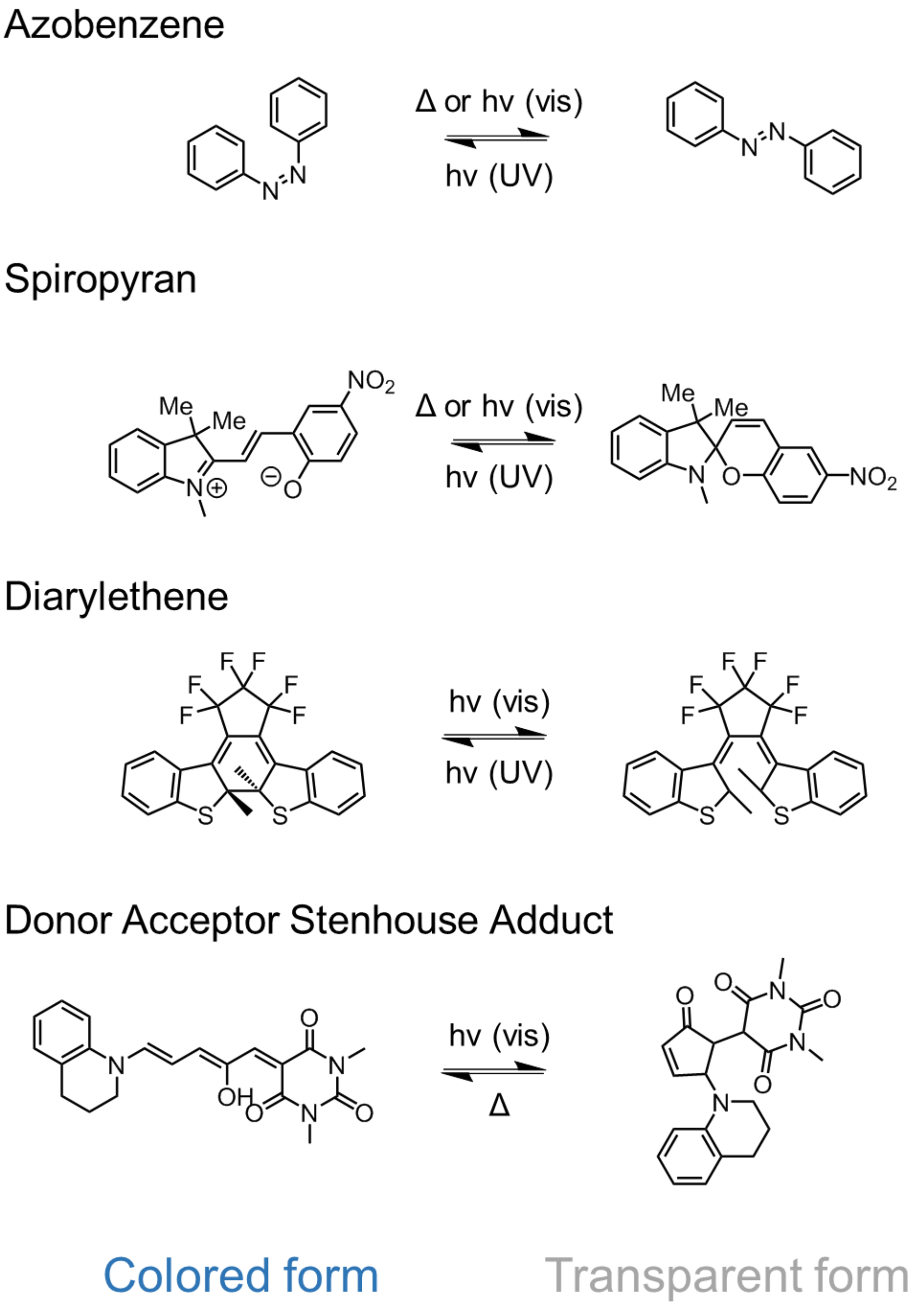

**Figure 1.1:** Select photochromic molecules from popular families. Colored isomers (left) undergo isomerization to a transparent isomer (right). Reactions with a Δ denote T-type photochromes and the directionality dictates the stable isomer.

The families of organic photoswitches discussed thus far have been extensively modified with a variety of chemistries enabling researchers to tune their photophysical behavior and allow for their introduction into materials systems. As expected, by changing the electronics of the molecule through electron donating / withdrawing units, a wide range of optical properties can be manipulated.[19] There are many examples of modifying the electronics to impact absorbance of nearly all classes of photoswitches, however these modifications also serve to directly impact the half-life of T-type switches and the photostationary state (equilibrium of isomeric species under irradiation that arises from overlapping absorbance bands) in both T-type and P-type motifs. Additionally, in certain examples, electronic modification has changed the character of a photoswitch from T-type to P-type.[20,21] Also, examples introducing steric

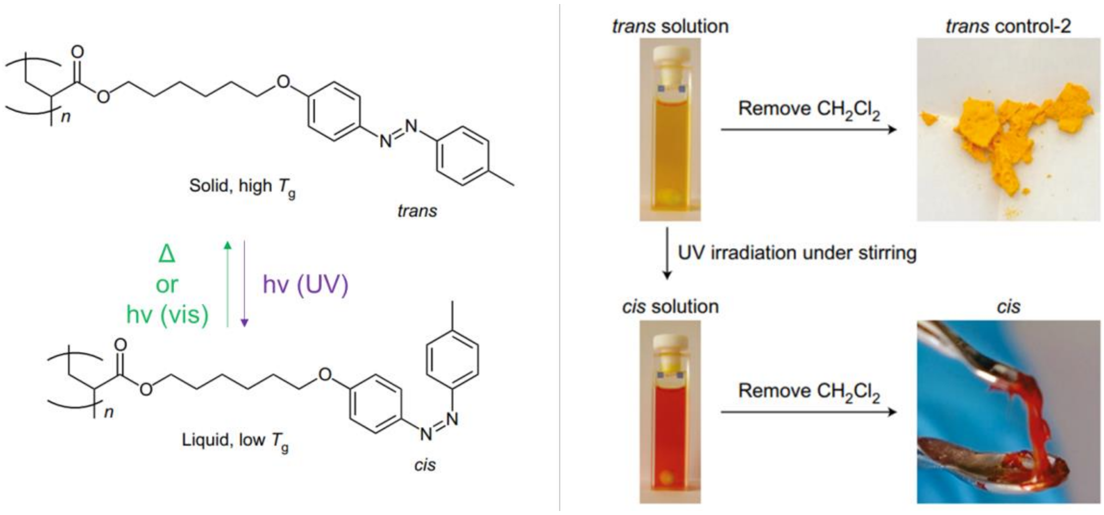

**Figure 1.2**: (left) Chemical structure of an acrylate polymer with pendant azobenzene units that undergo a *trans* to *cis* isomerization upon exposure to light. (right) Solutions of the two isomeric polymers and their isolated properties. The *trans* form remains solid while the *cis* form forms a viscous liquid. Adapted from reference 23 with permission. Copyright 2016, Springer Nature.

bulk near points of bond rotation serve to hinder the thermal back reaction in T-type switches, notably in azobenzene.[22] In diarylethene structures, the addition of a bulky hexafluorocyclopentene unit significantly increases the fatigue resistance of the molecules to repeated isomerization.[23] Additionally, through the installation of reactive handles, photoswitches have been readily tethered to polymer backbones, enabling large changes in bulk properties in polymers upon photoswitching events. As an example, **Figure 1.2** highlights the change of a polymer from glassy/solid to viscous/liquid through the photoswitching of pendant azobenzene units.[24] Given the large breadth of photochromic molecules and the chemical modifications thereof, the remainder of this section will focus on the modification of Donor Acceptor Stenhouse Adducts and their application in polymeric materials.

Donor Acceptor Stenhouse Adducts (DASA) were first synthesized by the Read de Alaniz group in 2014 through the reaction of alkyl amines (donor) with activated furans (acceptor).[25] This first generation of DASA molecules (Gen1) demonstrated many attractive features for photochromic molecules, namely high molar extinction coefficients (~100,000 $M^{-1}$ $cm^{-1}$), negative photochromism, and large changes in molecular volume and solubility upon photoswitching. The high absorptivity of Gen1 DASA was leveraged through the use of DASA as a small molecule thermal sensor embedded in a polybutadiene matrix, allowing for the tracking of the heat generated by a bullet fired through the sample.[26] Additionally, by taking advantage of the strong change in solubility between isomers of Gen1 DASA light-addressable micelles were developed and shown to be effective for drug release.[27] Despite these impressive applications, Gen1 DASA had a limited range of absorbance, which could only be impacted through manipulating the acceptor group.[28] Furthermore, Gen1 DASA molecules could only be switched in highly nonpolar environments such as Toluene, significantly limiting their application.

To address these issues, the second generation of DASA (Gen2) was developed using a variety of conjugated aniline donors.[29] The addition of these tunable donors

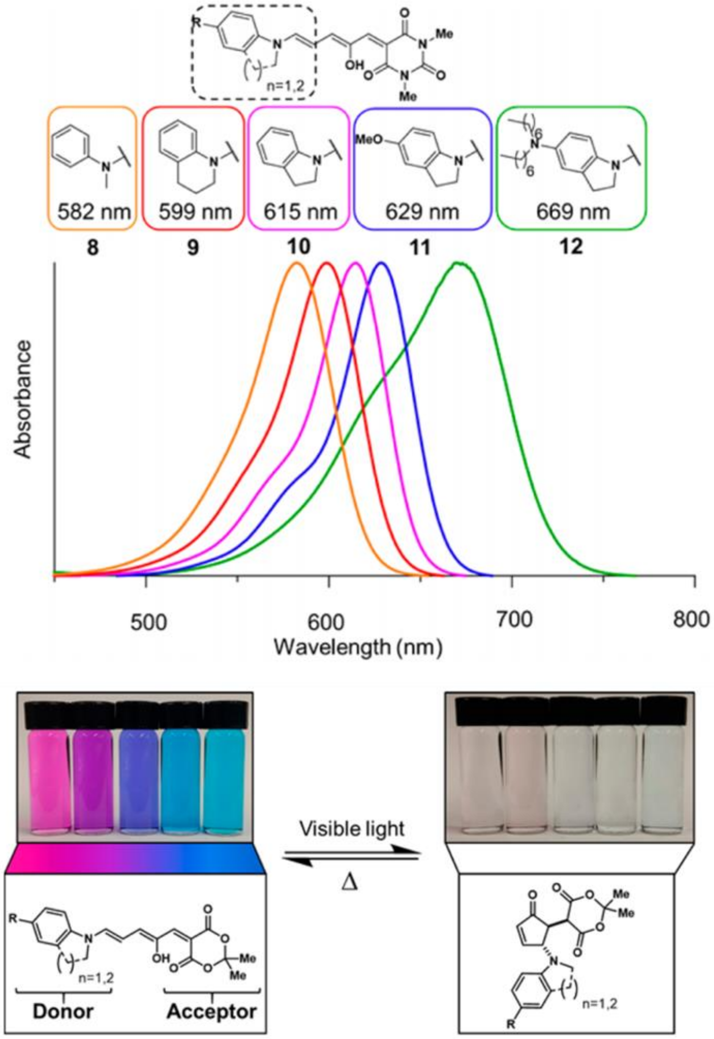

**Figure 1.3**: (top) Chemical structures of the second generation of DASA photoswitches, which can be tuned through the aniline donor resulting a wide range of absorbances. (bottom) Solutions of Gen2 DASA demonstrating the breadth of color made possible with aniline donors. Adapted from reference 28 with permission. Copyright 2016, American Chemical Society.

yielded an impressive range of absorbance, see **Figure 1.3**. Furthermore, Gen2 DASA significantly increased the range of solvents in which photochromism could be demonstrated, which is essential for implementation in materials systems. With these impressive properties in mind, Gen2 DASA was tethered onto polymers to make tunable photochromic polymer films, see **Figure 1.4** for images of these films under several irradiation conditions.[30] Interestingly, after bleaching, the pendant DASA units were unable to revert to their colored triene form until heated above the $T_g$ of the

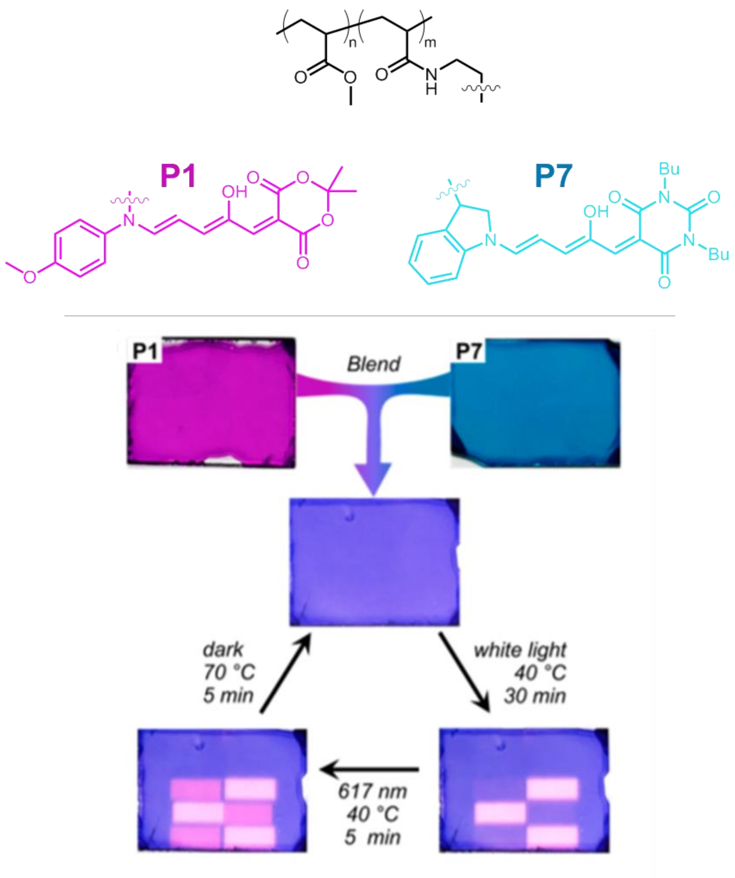

**Figure 1.4**: (top) Chemical structures of copolymers P1 and P7 with distinct tethered DASA moieties at a similar loading (m = 3–4%). (bottom) The result of blending P1 and P7 together to form a film. Each DASA can be individually addressed with different wavelengths of visible light. Adapted from reference 29 with permission. Copyright 2017, American Chemical Society.

polymer matrix. It is hypothesized that the more compact cyclopentenone form of DASA gets trapped upon switching and is unable to ring open until there is sufficient free volume in the system.

Despite the clear advances of Gen2 DASA, several of the synthesized species had low equilibrium ratios of the open, colored form. This limitation was targeted in the introduction of the third generation (Gen3) of DASA. In this iteration, the tunable aniline donors were paired with a series of new acceptor moieties, further increasing the range of switching conditions and newfound control of the equilibrium state of isomerization.[31] Additionally, the Gen3 DASA compounds were demonstrated to undergo switching upon exposure with near infrared light, which is a highly desirable stimulus for biomedical applications.[32]

Despite the rapid advances in the synthesis of DASA compounds, their T-type nature, solvent dependency, and large extinction coefficients make the measurement of their photophysical parameters quite challenging. Given these issues, the primary characterization techniques used for DASA were normalized absorbance spectra and thermal recovery traces, which don’t give the necessary information to calculate important parameters such as quantum yield. In order to measure the photophysical parameters, direct measurement of the ratio of isomers would be necessary during irradiation. To solve this issue, a fiber-coupled Nuclear Magnetic Resonance (NMR) technique was developed, this technique is described fully in Chapter 2.[33]

## Light-Mediated Controlled Radical Polymerizations

The introduction of techniques to control polymer molecular weight, dispersity, and architecture is perhaps one of the most important developments in polymer chemistry. While many approaches to controlled polymerizations have been developed, the simplicity of controlled radical polymerization (CRP) techniques such as nitroxide-mediated polymerization,[34–36] atom transfer radical polymerization (ATRP),[37–39] and reversible addition-fragmentation chain-transfer polymerization (RAFT)[40–43] have enabled researchers to synthesize a remarkably diverse collection of polymers with seemingly limitless variety and ever-increasing complexity. CRP approaches to polymerization differ from free radical polymerizations through the addition of labile ‘mediating’ groups that act to reversibly activate/deactivate the growing chain end of propagating polymer chains, shown schematically in **Figure 1.5**. This process reduces the concentration of radicals in the system, reducing termination events and allowing the polymers to grow at a constant rate, resulting in user-defined molecular weights with low dispersity. In practice, ATRP and RAFT approaches represent the most commonly used procedures for generating controlled radical polymers, these two techniques can be readily differentiated by their mediating group / chain ends; a labile halogen atom (typically Br) vs a thiocarbonylthio (typically trithiocarbonate or benzodithioate) compound for ATRP and RAFT, example structures shown in **Figure 1.5**. Each system has its own advantages and disadvantages, namely RAFT tends to be more robust through a larger variety of monomer families, but the Br chain ends of ATRP have greater flexibility for modification after polymerization. Between these

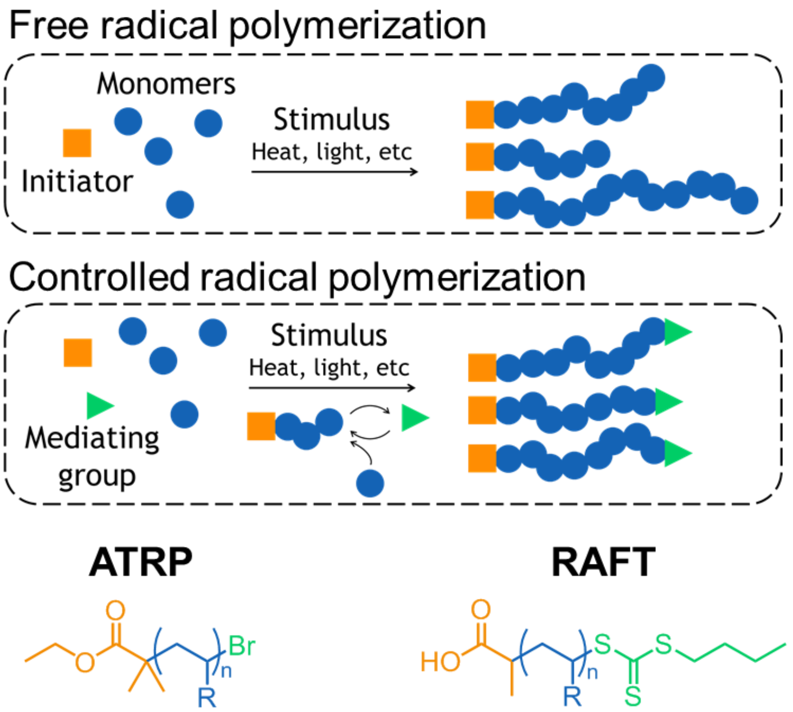

**Figure 1.5**: (top) Schematic representations of free radical and controlled radical polymerizations. Controlled radical polymerizations use a mediating group that reversibly reacts with the growing chain end, resulting in polymers growing at the same rate, yielding narrow molecular weight distributions. (bottom) Sample chemical structures of polymers synthesized using ATRP and RAFT.

techniques, a wide variety of conditions and catalysts have been developed for the successful polymerization of a wide range of monomers in aqueous and organic media. In recent years, great attention has been directed towards the development of CRP approaches regulated by external stimuli[44] such as mechanical force,[45] applied voltage,[46] or light.[47] Of these stimuli, light has emerged as a particularly attractive avenue for externally regulated CRP given the low cost, tunability, and spatiotemporal control offered by modern light sources. In the seminal work by Fors and Hawker, it was demonstrated that ATRP could be mediated by an external light source through a photoredox catalyst, **Figure 1.6**.[47] This advance gave researchers the ability to temporally control polymerizations by simply turning the light ‘off’ to cease polymerization, only starting growth again after subsequent irradiation, **Figure 1.6c**.

Since this report, many additional light-mediated CRP systems were developed, including both metal-free[8,48–50] and more traditional Cu-ligand catalysts[51–54] for ATRP as well as a catalysts for photoinduced electron transfer RAFT (PET-RAFT).[55–58] An abridged timeline of the development of select photo-CRP catalysts is shown in **Figure 1.7**. Between the many newly developed photo-CRP approaches, a wide range of monomer classes and polymer architectures have been synthesized, highlighting the added versatility light-mediated techniques bring to CRP.

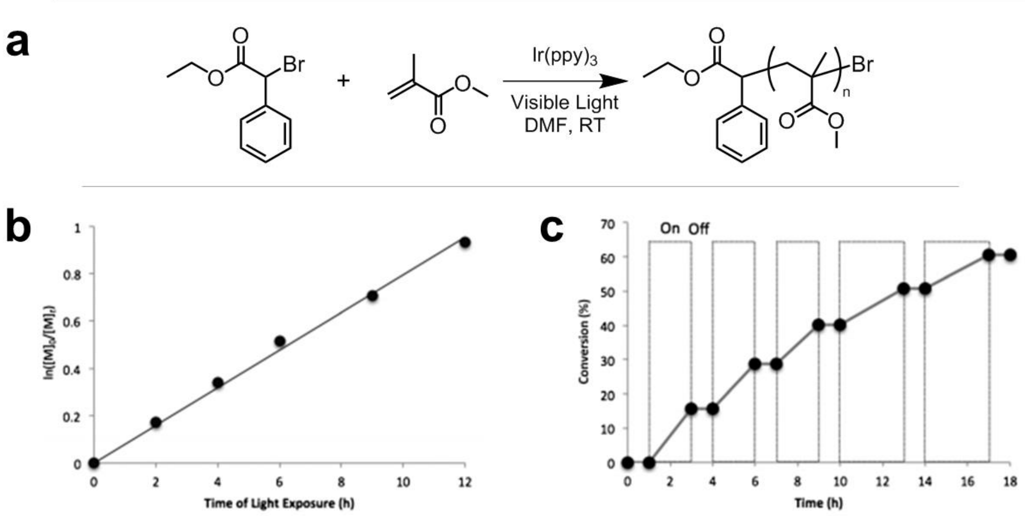

**Figure 1.6**: a) Reaction scheme for the polymerization of methyl methacrylate using Ir(ppy)$_3$ as a catalyst under visible light conditions. b) Demonstration of linear kinetics, implying the radical density is constant throughout the polymerization. c) Demonstration of temporal control of the polymerization through turning the light source ‘on’ and ‘off’ at regular intervals. Adapted from reference 45 with permission. Copyright 2012, John Wiley and Sons.

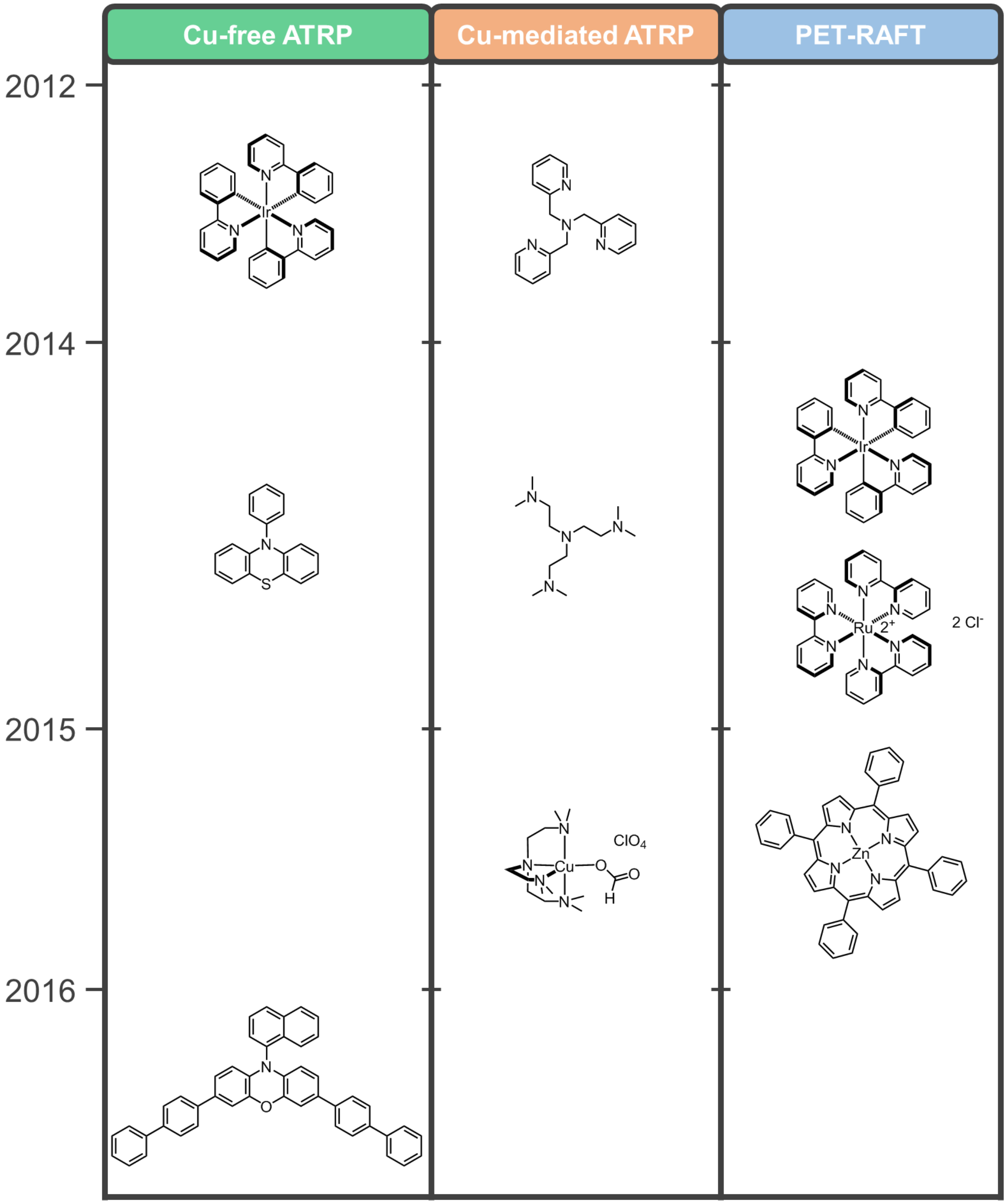

**Figure 1.8**: Timeline of the development of select state-of-the-art photo-mediated controlled radical polymerization systems. These catalytic systems are featured heavily in Chapter 4.

The incorporation of photo-CRP in materials applications largely involves the use of focused / patterned light to spatially define materials properties in systems inaccessible to thermal approaches. This concept has been exploited in the synthesis of a variety of interesting materials, such as polymers grown from the surface of cells,[59] light emitting diodes,[60] materials with spatially defined mechanical properties,[61] and the growth of patterned polymer brushes.[62–64] Perhaps the best demonstrations of the spatial patterning enabled by photo-CRP are surface initiated polymer brushes. A wide range of polymer brushes with high resolution (< 20 microns) have been demonstrated using precisely defined photomasks. By taking advantage of the living nature of the brush growth process, additional monomers can be added to the system after an initial growth step, allowing for the production of features with chemo-selective response or surfaces with precise bottlebrush architectures.[64,65] Along with the development of new catalysts, the procedures for producing patterned polymer brushes have become more user-friendly, enabling the patterning of wafer-scale brushes, **Figure 1.8**.[66]

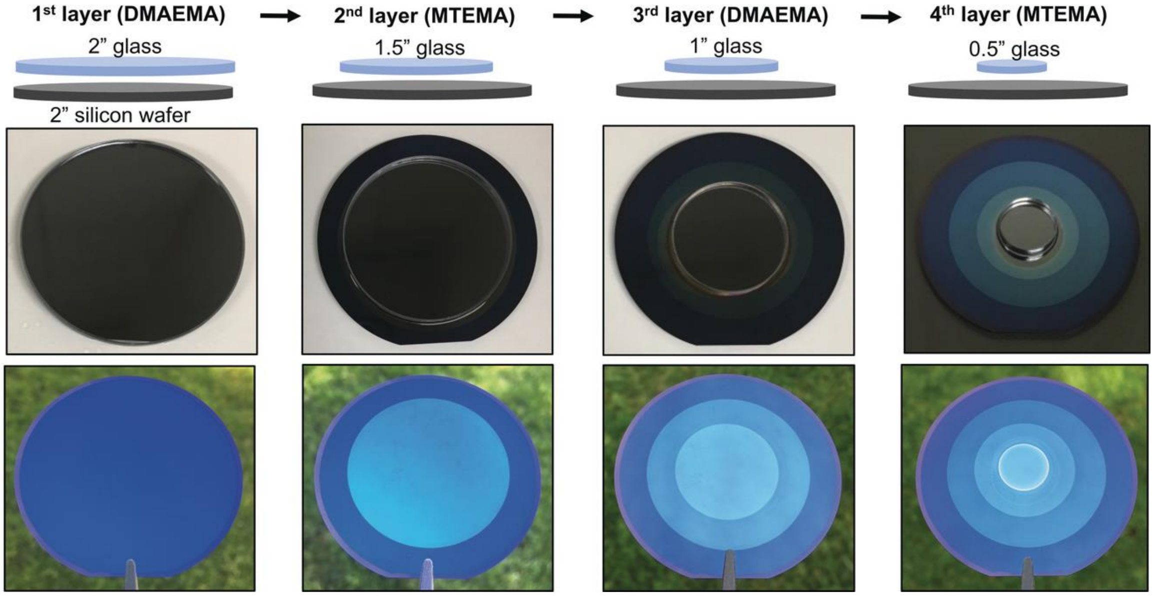

**Figure 1.8**: Series of consecutively grown polymer brushes on a 2" silicon wafer. Circular patterns were templated with a simple glass cover slip. Adapted from reference 64 with permission. Copyright 2018, John Wiley and Sons.

Despite the rapid growth of photo-CRP techniques, there are still several outstanding issues in the field. Throughout the literature, there is evidence of growth occurring during dark periods in temporal studies, but this growth is typically dismissed as experimental error.[67–70] Since this issue is rarely discussed at length, the underlying mechanisms that may or may not be at work during dark periods are left unexplored and can therefore not be successfully addressed in further developments of photo-CRP. Additionally, there are few direct comparisons between photo-CRP systems (constant irradiation conditions, sample volumes, etc), especially between CRP families such as PET-RAFT and metal-free ATRP, despite similar underlying mechanisms. These issues are discussed at length in Chapter 3.[71]

### Light in Additive Manufacturing

Additive manufacturing, or 3D printing, has received growing attention from the scientific community given its ability to rapidly produce materials with a wide range of properties from easily manipulated digital files.[72] As an example, researchers are now able to directly modify a parts underlying mesostructure, allowing for a wide range of interesting materials properties such as impacting local stiffness and selectively patterning Poisson's ratio.[73–75] The vast majority of 3D printing techniques can be split between direct-write and projection approaches. Direct-write techniques such as fused deposition modelling and direct ink writing utilize nozzles or similar sources to extrude molten filaments or inks which solidify at room temperature or upon exposure to a light source that closely follows the printing nozzle. These approaches, especially direct ink writing, have seen considerable attention in recent years given the modular nature of the nozzles and possible ink chemistries. This modularity has resulted in a vast number of printable materials systems from hydrogels[76–79] to highly aligned composites[80–82] capable of remarkable shape changes upon swelling, **Figure 1.9**. Additionally, through the addition of spiropyran units as crosslinkers have enabled the 3D printing of patterned mechanochromic materials.[83] Despite this range of materials, direct-write approaches suffer from poor interfacial connectivity, extremely slow build rates (< 1 cm per hour), and low line resolution. These issues can, in part, be avoided by projection curing techniques such as stereolithography (SLA) and digital light projection (DLP) which will be the focus of this section.

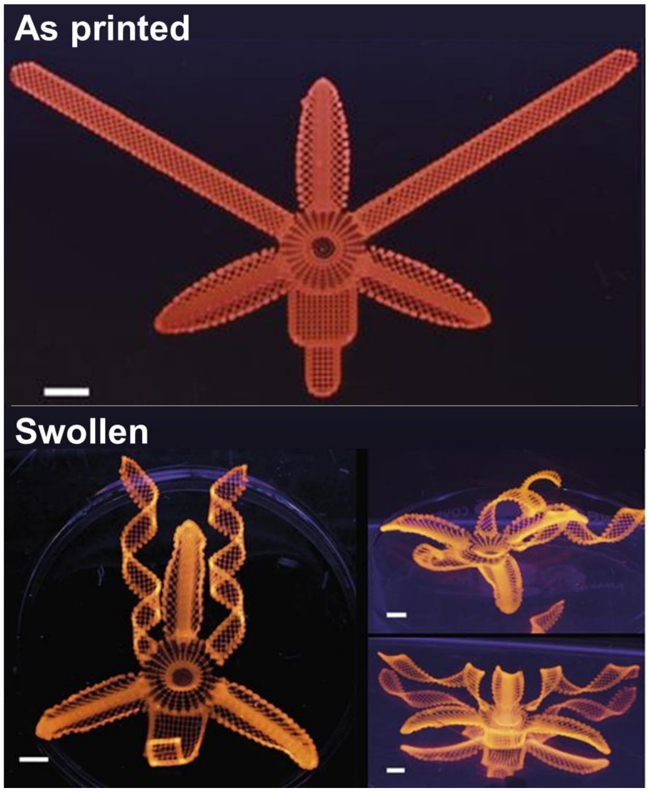

**Figure 1.9**: top) Structure printed with aligned filler particles through direct write printing designed to undergo programmed folding events upon swelling. bottom) Top down and side views of the part upon swelling to form orchid-like patterns. Adapted from reference 78 with permission. Copyright 2016, Springer Nature.

In contrast to direct-write techniques, where each layer is traced out by a moving nozzle, SLA/DLP approaches cure entire layers of resin near simultaneously using a rapidly rastered laser source or projected image. The layer-by-layer curing of DLP techniques is illustrated in **Figure 1.10**, where a part built on a moving stage is lowered into a photocurable resin, at which point a pattern is projected into the resin thereby curing the desired layer, the part is then delaminated from the tank and repositioned for the next layer to be cured. The precise optics of projection 3D printing technique greatly enhance the resolution of parts relative the direct-write techniques, which are limited by nozzle diameter and ink viscosity. In addition to the increased resolution of

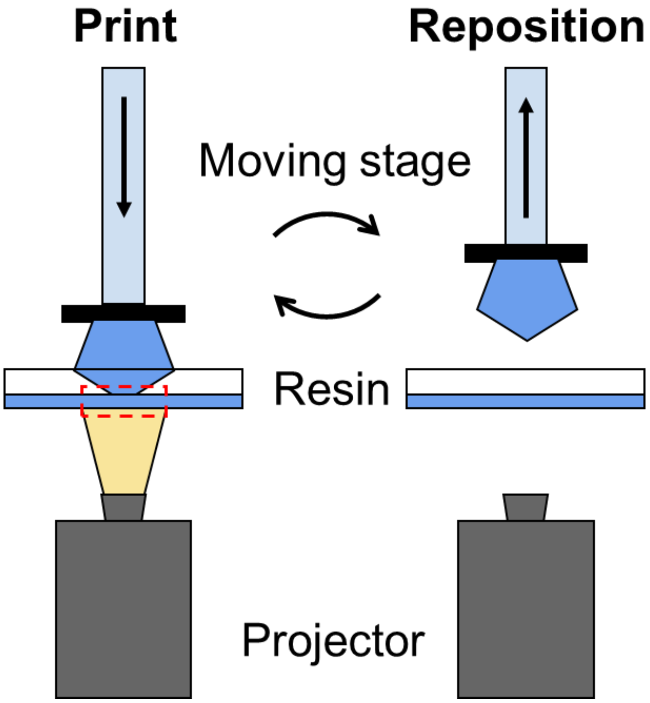

**Figure 1.10**: Schematic of printing process of DLP approaches to 3D printing. (left) A layer is projected into a bath of curable resin and bonded to the growing part. (right) The part is delaminated from the bottom of the tank and repositioned for the next layer to be cured.

SLA and DLP techniques, chemists and engineers have been able to take advantage of light intensity to spatially grade the crosslink density of parts, resulting in local tuning of mechanical properties.[84]

Despite the vastly improved resolution of SLA / DLP, the parts produced by these approaches are plagued by defects between cured layers.[85] The root cause of layering defects in DLP parts is the delamination / repositioning step in printing, which serves to remove the in-progress part from the bottom of the resin tank, resulting in stepwise growth. To remove these defects from 3D printed parts, the layers would have to be continuously cured and removed from the tank in a fluid motion. The first reported continuous approach to 3D printing, called continuous liquid interface production (CLIP), utilized radically-cured resins in conjunction with an oxygen permeable window at the bottom of the tank that set up a thin ‘dead zone’ where radicals were actively consumed, eliminating part lamination.[85] With the issue of lamination eliminated, the in-progress part can be pulled from the resin at a constant rate (hundreds of mm per hour), effectively eliminating layers in the finished product, **Figure 1.11**. In addition to the oxygen-mediated mechanism of CLIP, continuous printing can be accomplished using a high-density immiscible fluid at the bottom of the resin tank to avoid part lamination.

Through the use of clever chemistry and processing techniques, projection approaches have considerable advantages over their direct-write counterparts for the production of single material parts. However, in order to produce parts with multiple chemistries throughout, current projection techniques require their resin tanks to be swapped out mid-print, potentially within a given layer, greatly reducing the build rate.[86,87] Although this approach enables multimaterial printing in projection-style printers, the exchange of resin baths is directly contrary to the notion of continuous printing. For this reason, a majority of multimaterial printing is carried out using multi-nozzle techniques, where discrete inks can be delivered from individual nozzles of specialized microfluidic devices greatly increasing the complexity of multimaterial techniques.[88] To overcome this limitation, new chemistry and processing techniques were developed for continuous 3D printing, which is discussed in Chapter 4.[89]

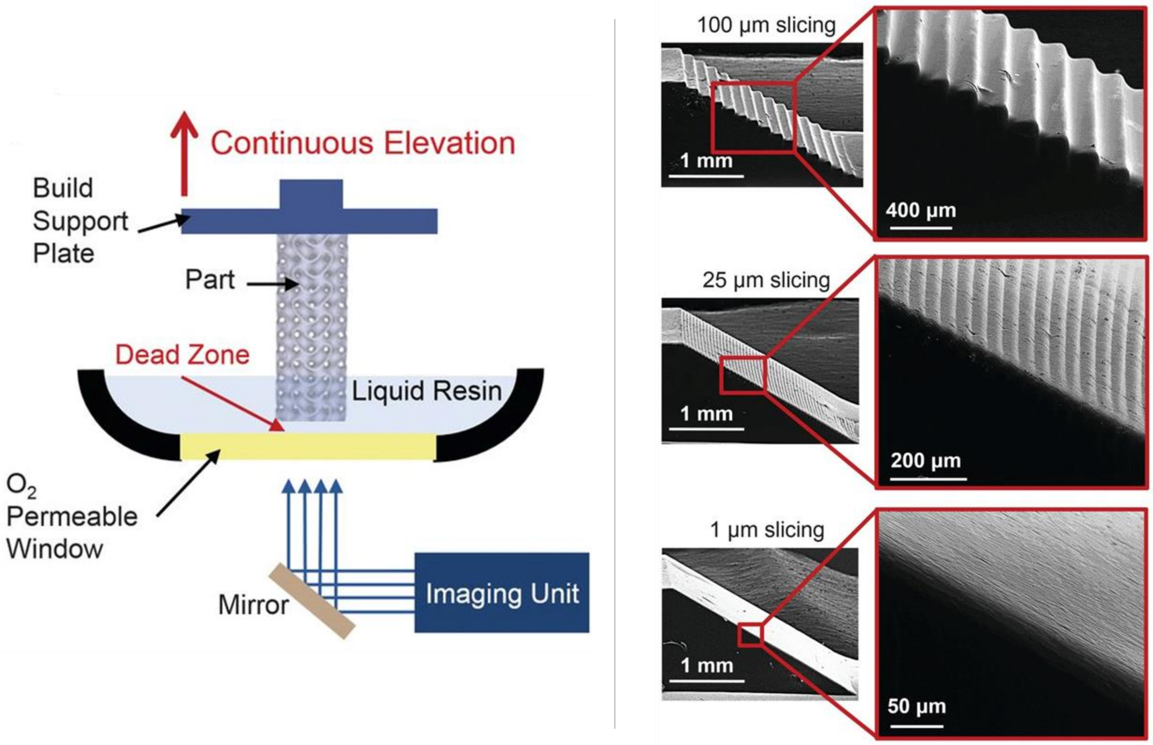

**Figure 1.11**: (left) Schematic of Continuous Liquid Interface Production. (right) The results of different slicing profiles on parts printed with CLIP, at the thinnest setting the part has no signs of layering. The continuous nature of the printing process eliminates layer defects within the printed parts. Adapted from reference 83 with permission. Copyright 2016, AAAS.

## Thesis scope

This thesis describes the development of approaches for the measurement and synthesis of light-mediated precise polymeric materials. Chapter 2 describes the construction of a fiber-coupled Nuclear Magnetic Resonance (NMR) system for *in situ* monitoring of photochemical transformations. Interestingly, the development of this technique was catalyzed by interest in studying photochromic molecules (primarily DASA) in collaboration with the Read de Alaniz group, which lead to the discovery of well-behaved photobleaching fronts in optically dense samples. The fiber-coupled NMR technique was then implemented in studying photo-mediated CRP, which led to a series of studies spanning a wide array of state-of-the-art CRP techniques, the topic of Chapter 3. The core concepts of these chapters, namely photobleaching fronts and photopolymerizations, were then combined to develop a fundamentally new approach to multimaterial 3D printing taking advantage of wavelength-specific chemistries, the topic of Chapter 4. The final chapter gives a brief summary of these works and an outlook on future challenges and opportunities for photochemical monitoring and light-driven additive manufacturing.

## References

(1) Kim, P.; Kwon, K. W.; Park, M. C.; Lee, S. H.; Kim, S. M. Soft Lithography for Microfluidics : A Review. *BioChip J.* **2008**, *2* (1), 1–11.

(2) Pimpin, A.; Srituravanich, W. Review on Micro- and Nanolithography Techniques and Their Applications. *Eng. J.* **2011**, *16* (1), 37–55.

(3) Cho, H. J.; Chung, M.; Shim, M. S. Engineered Photo-Responsive Materials for near-Infrared-Triggered Drug Delivery. *J. Ind. Eng. Chem.* **2015**, *31*, 15–25.

(4) Barhoumi, A.; Liu, Q.; Kohane, D. S. Ultraviolet Light-Mediated Drug Delivery : Principles , Applications , and Challenges. *J. Control. Release* **2015**, *219*, 31–42.

(5) Chen, M.; Gu, Y.; Singh, A.; Zhong, M.; Jordan, A. M.; Biswas, S.; Korley, L. T. J.; Balazs, A. C.; Johnson, J. A. Living Additive Manufacturing: Transformation of Parent Gels into Diversely Functionalized Daughter Gels Made Possible by Visible Light Photoredox Catalysis. *ACS Cent. Sci.* **2017**, *3* (2), 124–134.

(6) Accardo, J. V; Kalow, J. A. Reversibly Tuning Hydrogel Stiffness through Photocontrolled Dynamic Covalent Crosslinks. *Chem. Sci.* **2018**, *9*, 5987–5993.

(7) Chen, M.; Zhong, M.; Johnson, J. A. Light-Controlled Radical Polymerization: Mechanisms, Methods, and Applications. *Chem. Rev.* **2016**, *116* (17), 10167–10211.

(8) Discekici, E. H.; Anastasaki, A.; Alaniz, J. R. De; Hawker, C. J. Evolution and Future Directions of Metal-Free Atom Transfer Radical Polymerization. *Macromolecules* **2018**, *51*, 7421–7434.

(9) Poelma, J. E.; Fors, B. P.; Meyers, G. F.; Kramer, J. W.; Hawker, C. J.

Fabrication of Complex Three-Dimensional Polymer Brush Nanostructures through Light-Mediated Living Radical Polymerization. *Angew. Chemie - Int. Ed.* **2013**, *52* (27), 6844–6848.

(10) Irie, M. Photochromism: Memories and Switches. *Chem. Rev.* **2000**, *100* (5), 1683–1684.

(11) Corns, S. N.; Partington, S. M.; Towns, A. D. Industrial Organic Photochromic Dyes. *Color. Technol.* **2009**, *125*, 249–261.

(12) Qin, M.; Huang, Y.; Li, F.; Song, Y. Photochromic Sensors: A Versatile Approach for Recognition and Discrimination. *J. Mater. Chem. C* **2015**, *3* (36), 9265–9275.

(13) Feringa, B. E. N. L. In Control of Motion : From Molecular Switches to Molecular Motors. *Acc. Chem. Res.* **2001**, *34* (6), 504–513.

(14) Robb, M. J.; Kim, T. A.; Halmes, A. J.; White, S. R.; Sottos, N. R.; Moore, J. S. Regioisomer-Specific Mechanochromism of Naphthopyran in Polymeric Materials. *J. Am. Chem. Soc.* **2016**, *138* (38), 12328–12331.

(15) Eisenreich, F.; Kathan, M.; Dallmann, A.; Ihrig, S. P.; Schwaar, T.; Schmidt, B. M.; Hecht, S. A Photoswitchable Catalyst System for Remote-Controlled (Co)Polymerization in Situ. *Nat. Catal.* **2018**, *1* (7), 516–522.

(16) Fu, C.; Xu, J.; Boyer, C. Photoacid-Mediated Ring Opening Polymerization Driven by Visible Light. *Chem. Commun.* **2016**, *52* (44), 7126–7129.

(17) Tong, R.; Hemmati, H. D.; Langer, R.; Kohane, D. S. Photoswitchable Nanoparticles for Triggered Tissue Penetration and Drug Delivery. *J. Am. Chem. Soc.* **2012**, *134*, 8848–8855.

(18) Aiken, S.; Edgar, R. J. L.; Gabbutt, C. D.; Heron, B. M.; Hobson, P. A. Negatively Photochromic Organic Compounds: Exploring the Dark Side. *Dye. Pigment.* **2018**, *149*, 92–121.

(19) Zhang, J.; Zou, Q.; Tian, H. Photochromic Materials: More than Meets the Eye. *Adv. Mater.* **2013**, *25* (3), 378–399.

(20) Favaro, G.; Mazzucato, U.; Ortica, F.; Smimmo, P. Thermal Reversibility and Bistability in Photochromic Diarylethenes. *Inorganica Chim. Acta* **2007**, *360* (3), 995–999.

(21) Kobatake, S.; Terakawa, Y. Acid-Induced Photochromic System Switching of Diarylethene Derivatives between P- and T-Types. *Chem. Commun.* **2007**, *0*, 1698–1700.

(22) Sadovski, O.; Beharry, A. A.; Zhang, F.; Woolley, G. A. Spectral Tuning of Azobenzene Photoswitches for Biological Applications. *Angew. Chemie - Int. Ed.* **2009**, *48* (8), 1484–1486.

(23) Hanazawa, M.; Sumiya, R.; Horikawa, Y.; Irie. Thermally Irreversible Photochromic Systems. Reversible Photocyclization of 1,2-Bis( 2-Methyl Benzo[b]Thiophen-3-Yl)Perfluorocycloal Kene Derivatives. *J. Chem. Soc., Chem. Commun.* **1992**, *0*, 206–207.

(24) Zhou, H.; Xue, C.; Weis, P.; Suzuki, Y.; Huang, S.; Koynov, K.; Auernhammer, G. K.; Berger, R.; Butt, H. J.; Wu, S. Photoswitching of Glass Transition Temperatures of Azobenzene-Containing Polymers Induces Reversible Solid-to-Liquid Transitions. *Nat. Chem.* **2017**, *9* (2), 145–151.

(25) Helmy, S.; Leibfarth, F. A.; Oh, S.; Poelma, J. E.; Hawker, C. J.; Read de Alaniz,

J. Photoswitching Using Visible Light: A New Class of Organic Photochromic Molecules. *J. Am. Chem. Soc.* **2014**, *136* (23), 8169−8172.

(26) Mason, B. P.; Whittaker, M.; Hemmer, J.; Arora, S.; Harper, A.; Alnemrat, S.; McEachen, A.; Helmy, S.; Read De Alaniz, J.; Hooper, J. P. A Temperature-Mapping Molecular Sensor for Polyurethane-Based Elastomers. *Appl. Phys. Lett.* **2016**, *108* (4).

(27) Poelma, S. O.; Oh, S. S.; Helmy, S.; Knight, A. S.; Burnett, G. L.; Soh, H. T.; Hawker, C. J.; Read De Alaniz, J. Controlled Drug Release to Cancer Cells from Modular One-Photon Visible Light-Responsive Micellar System. *Chem. Commun.* **2016**, *52* (69), 10525–10528.

(28) Helmy, S.; Oh, S.; Leibfarth, F. A.; Hawker, C. J.; Read De Alaniz, J. Design and Synthesis of Donor-Acceptor Stenhouse Adducts: A Visible Light Photoswitch Derived from Furfural. *J. Org. Chem.* **2014**, *79* (23), 11316–11329.

(29) Hemmer, J. R.; Poelma, S. O.; Treat, N.; Page, Z. A.; Dolinski, N. D.; Diaz, Y. J.; Tomlinson, W.; Clark, K. D.; Hooper, J. P.; Hawker, C.; et al. Tunable Visible and Near Infrared Photoswitches. *J. Am. Chem. Soc.* **2016**, *138* (42), 13960–13966.

(30) Ulrich, S.; Hemmer, J. R.; Page, Z. A.; Dolinski, N. D.; Rifaie-Graham, O.; Bruns, N.; Hawker, C. J.; Boesel, L. F.; Read De Alaniz, J. Visible Light-Responsive DASA-Polymer Conjugates. *ACS Macro Lett.* **2017**, *6* (7), 738–742.

(31) Hemmer, J. R.; Page, Z. A.; Clark, K. D.; Stricker, F.; Dolinski, N. D.; Hawker, C. J.; Read de Alaniz, J. Controlling Dark Equilibria and Enhancing Donor-Acceptor Stenhouse Adduct Photoswitching Properties through Carbon Acid

Design. *J. Am. Chem. Soc.* **2018**, *140* (33), 10425–10429.

(32) Luo, S.; Zhang, E.; Su, Y.; Cheng, T.; Shi, C. A Review of NIR Dyes in Cancer Targeting and Imaging. *Biomaterials* **2011**, *32* (29), 7127–7138.

(33) Dolinski, N. D.; Page, Z. A.; Eisenreich, F.; Niu, J.; Hecht, S.; Read de Alaniz, J.; Hawker, C. J. A Versatile Approach for In Situ Monitoring of Photoswitches and Photopolymerizations. *ChemPhotoChem* **2017**, *1* (4), 125–131.

(34) Georges, M. K.; Veregin, R. P. N.; Kazmaier, P. M.; Hamer, G. K. Narrow Molecular Weight Resins by a Free-Radical Polymerization Process. *Macromolecules* **1993**, *26*, 2987–2988.

(35) Hawker, C. J.; Bosman, A. W.; Harth, E.; Copolymers, D. R. New Polymer Synthesis by Nitroxide Mediated Living Radical Polymerizations. *Chem. Rev.* **2001**, *101*, 3661–3688.

(36) Nicolas, J.; Guillaneuf, Y.; Lefay, C.; Bertin, D.; Gigmes, D.; Charleux, B. Nitroxide-Mediated Polymerization. *Prog. Polym. Sci.* **2013**, *38* (1), 63–235.

(37) Kato, M.; Kamigaito, M.; Sawamoto, M.; Higashimura, T. Polymerization of Methyl Methacrylate with the Carbon Tetrachloride/Dichlorotris-(Triphenylphosphine)Ruthenium(II)/ Methylaluminum Bis(2,6-Di-Ferf-Butylphenoxide) Initiating System: Possibility of Living Radical Polymerization. *Macromolecules* **1995**, *28* (5), 1721–1723.

(38) Wang, J.-S.; Matyjaszewski, K. Controlled /“ Living ” Radical Polymerization . Atom Transfer Radical Polymerization in the Presence of Pi-Cl. *J. Am. Chem. Soc.* **1995**, *117* (20), 5614–5615.

(39) Matyjaszewski, K. Atom Transfer Radical Polymerization (ATRP): Current

Status and Future Perspectives. *Macromolecules* **2012**, *45* (10), 4015–4039.

(40) Chiefari, J.; Chong, Y. K. B.; Ercole, F.; Krstina, J.; Jeffery, J.; Le, T. P. T.; Mayadunne, R. T. A.; Meijs, G. F.; Moad, C. L.; Moad, G.; et al. Living Free-Radical Polymerization by Reversible Addition - Fragmentation Chain Transfer : The RAFT Process. *Macromolecules* **1998**, *31* (16), 5559–5562.

(41) Destarac, M.; Charmot, D.; Franck, X.; Zard, S. Z. Dithiocarbamates as Universal Reversible Addition-Fragmentation Chain Transfer Agents. *Macromol. Rapid Commun.* **2000**, *21* (15), 1035–1039.

(42) Keddie, D. J. A Guide to the Synthesis of Block Copolymers Using Reversible-Addition Fragmentation Chain Transfer (RAFT) Polymerization. *Chem. Soc. Rev.* **2014**, *43* (2), 496–505.

(43) Niu, J.; Page, Z. A.; Dolinski, N. D.; Anastasaki, A.; Hsueh, A. T.; Soh, H. T.; Hawker, C. J. Rapid Visible Light-Mediated Controlled Aqueous Polymerization with in Situ Monitoring. *ACS Macro Lett.* **2017**, *6* (10), 1109–1113.

(44) Pan, X.; Fantin, M.; Yuan, F.; Matyjaszewski, K. Externally Controlled Atom Transfer Radical Polymerization. *Chem. Soc. Rev.* **2018**, *47* (14), 5457–5490.

(45) Mohapatra, H.; Kleiman, M.; Esser-Kahn, A. P. Mechanically Controlled Radical Polymerization Initiated by Ultrasound. *Nat. Chem.* **2017**, *9* (2), 135–139.

(46) Magenau, A. J. D.; Strandwitz, N. C.; Gennaro, A.; Matyjaszewski, K. Electrochemically Mediated Atom Transfer Radical Polymerization. *Science.* **2011**, *332*, 81–84.

(47) Fors, B. P.; Hawker, C. J. Control of a Living Radical Polymerization of Methacrylates by Light. *Angew. Chemie - Int. Ed.* **2012**, *51* (35), 8850–8853.

(48) Treat, N. J.; Sprafke, H.; Kramer, J. W.; Clark, P. G.; Barton, B. E.; Read De Alaniz, J.; Fors, B. P.; Hawker, C. J. Metal-Free Atom Transfer Radical Polymerization. *J. Am. Chem. Soc.* **2014**, *136* (45), 16096–16101.

(49) Theriot, J. C.; Lim, C.-H.; Yang, H.; Ryan, M. D.; Musgrave, C. B.; Miyake, G. M. Organocatalyzed Atom Transfer Radical Polymerization Driven by Visible Light. *Science.* **2016**, *352* (6289), 1082–1086.

(50) Pearson, R. M.; Lim, C. H.; McCarthy, B. G.; Musgrave, C. B.; Miyake, G. M. Organocatalyzed Atom Transfer Radical Polymerization Using N-Aryl Phenoxazines as Photoredox Catalysts. *J. Am. Chem. Soc.* **2016**, *138* (35), 11399–11407.

(51) Konkolewicz, D.; Schröder, K.; Buback, J.; Bernhard, S.; Matyjaszewski, K. Visible Light and Sunlight Photoinduced ATRP with Ppm of Cu Catalyst. *ACS Macro Lett.* **2012**, *1* (10), 1219–1223.

(52) Frick, E.; Anastasaki, A.; Haddleton, D. M.; Barner-Kowollik, C. Enlightening the Mechanism of Copper Mediated PhotoRDRP via High-Resolution Mass Spectrometry. *J. Am. Chem. Soc.* **2015**, *137* (21), 6889–6896.

(53) Nikolaou, V.; Anastasaki, A.; Brandford-Adams, F.; Whitfield, R.; Jones, G. R.; Nurumbetov, G.; Haddleton, D. M. Discrete Copper(II)-Formate Complexes as Catalytic Precursors for Photo-Induced Reversible Deactivation Polymerization. *Polym. Chem.* **2016**, *7* (1), 191–197.

(54) Kork, S.; Ciftci, M.; Tasdelen, M. A.; Yagci, Y. Photoinduced Cu(0)-Mediated Atom Transfer Radical Polymerization. *Macromol. Chem. Phys.* **2016**, *217* (6), 812–817.

(55) Xu, J.; Jung, K.; Atme, A.; Shanmugam, S.; Boyer, C. A Robust and Versatile Photoinduced Living Polymerization of Conjugated and Unconjugated Monomers and Its Oxygen Tolerance. *J. Am. Chem. Soc.* **2014**, *136* (14), 5508–5519.

(56) Xu, J.; Jung, K.; Corrigan, N. A.; Boyer, C. Aqueous Photoinduced Living/Controlled Polymerization: Tailoring for Bioconjugation. *Chem. Sci.* **2014**, *5* (Iii), 3568–3575.

(57) Shanmugam, S.; Xu, J.; Boyer, C. Exploiting Metalloporphyrins for Selective Living Radical Polymerization Tunable over Visible Wavelengths. *J. Am. Chem. Soc.* **2015**, *137* (28), 9174–9185.

(58) Xu, J.; Shanmugam, S.; Duong, H. T.; Boyer, C. Organo-Photocatalysts for Photoinduced Electron Transfer-Reversible Addition-Fragmentation Chain Transfer (PET-RAFT) Polymerization. *Polym. Chem.* **2015**, *6* (31), 5615–5624.

(59) Niu, J.; Lunn, D. J.; Pusuluri, A.; Yoo, J. I.; O'Malley, M. A.; Mitragotri, S.; Soh, H. T.; Hawker, C. J. Engineering Live Cell Surfaces with Functional Polymers via Cytocompatible Controlled Radical Polymerization. *Nat. Chem.* **2017**, *9* (6), 537–545.

(60) Page, Z. A.; Narupai, B.; Pester, C. W.; Bou Zerdan, R.; Sokolov, A.; Laitar, D. S.; Mukhopadhyay, S.; Sprague, S.; McGrath, A. J.; Kramer, J. W.; et al. Novel Strategy for Photopatterning Emissive Polymer Brushes for Organic Light Emitting Diode Applications. *ACS Cent. Sci.* **2017**, *3* (6), 654–661.

(61) Cuthbert, J.; Zhang, T.; Biswas, S.; Olszewski, M.; Shanmugam, S.; Fu, T.; Gottlieb, E.; Kowalewski, T.; Balazs, A. C.; Matyjaszewski, K. Structurally

Tailored and Engineered Macromolecular (STEM) Gels as Soft Elastomers and Hard/Soft Interfaces. *Macromolecules* **2018**, *51*, 9184–9191.

(62) Discekici, E. H.; Pester, C. W.; Treat, N. J.; Lawrence, J.; Mattson, K. M.; Narupai, B.; Toumayan, E. P.; Luo, Y.; McGrath, A. J.; Clark, P. G.; et al. Simple Benchtop Approach to Polymer Brush Nanostructures Using Visible-Light-Mediated Metal-Free Atom Transfer Radical Polymerization. *ACS Macro Lett.* **2016**, *5* (2), 258–262.

(63) Pester, C. W.; Narupai, B.; Mattson, K. M.; Bothman, D. P.; Klinger, D.; Lee, K. W.; Discekici, E. H.; Hawker, C. J. Engineering Surfaces through Sequential Stop-Flow Photopatterning. *Adv. Mater.* **2016**, *28* (42), 9292–9300.

(64) Pester, C. W.; Poelma, J. E.; Narupai, B.; Patel, S. N.; Su, G. M.; Mates, T. E.; Luo, Y.; Ober, C. K.; Hawker, C. J.; Kramer, E. J. Ambiguous Anti-Fouling Surfaces: Facile Synthesis by Light-Mediated Radical Polymerization. *J. Polym. Sci. Part A Polym. Chem.* **2016**, *54* (2), 253–262.

(65) Narupai, B.; Poelma, J. E.; Pester, C. W.; Mcgrath, A. J.; Toumayan, E. P.; Luo, Y.; Kramer, J. W.; Clark, P. G.; Ray, P. C.; Hawker, C. J. Hierarchical Comb Brush Architectures via Sequential Light-Mediated Controlled Radical Polymerizations. *J. Polym. Sci. Part A Polym. Chem.* **2016**, *54* (15), 2276–2284.

(66) Narupai, B.; Page, Z. A.; Treat, N. J.; McGrath, A. J.; Pester, C. W.; Discekici, E. H.; Dolinski, N. D.; Meyers, G. F.; Alaniz, J. R. de; Hawker, C. J. Simultaneous Preparation of Multiple Polymer Brushes under Ambient Conditions Using ML Volumes. *Angew. Chemie Int. Ed.* **2018**, *57* (41), 13433–13438.

(67) Reeves, J. A.; Allegrezza, M. L.; Konkolewicz, D. Rise and Fall: Poly (Phenyl Vinyl Ketone) Photopolymerization and Photodegradation under Visible and UV Radiation. *Macromol. Rapid Commun.* **2017**, *38* (13), 1–5.

(68) Anastasaki, A.; Nikolaou, V.; Zhang, Q.; Burns, J.; Samanta, S. R.; Waldron, C.; Haddleton, A. J.; McHale, R.; Fox, D.; Percec, V.; et al. Copper(II)/Tertiary Amine Synergy in Photoinduced Living Radical Polymerization: Accelerated Synthesis of ω-Functional and α,ω-Heterofunctional Poly(Acrylates). *J. Am. Chem. Soc.* **2014**, *136* (3), 1141–1149.

(69) Anastasaki, A.; Nikolaou, V.; Brandford-Adams, F.; Nurumbetov, G.; Zhang, Q.; Clarkson, G. J.; Fox, D. J.; Wilson, P.; Kempe, K.; Haddleton, D. M. Photo-Induced Living Radical Polymerization of Acrylates Utilizing a Discrete Copper(II)-Formate Complex. *Chem. Commun.* **2015**, *51* (26), 5626–5629.

(70) Discekici, E. H.; Anastasaki, A.; Kaminker, R.; Willenbacher, J.; Truong, N. P.; Fleischmann, C.; Oschmann, B.; Lunn, D. J.; Read De Alaniz, J.; Davis, T. P.; et al. Light-Mediated Atom Transfer Radical Polymerization of Semi-Fluorinated (Meth)Acrylates: Facile Access to Functional Materials. *J. Am. Chem. Soc.* **2017**, *139* (16), 5939–5945.

(71) Dolinski, N. D.; Page, Z. A.; Discekici, E. H.; Meis, D.; Lee, I.-H.; Jones, G. R.; Whitfield, R.; Pan, X.; Mccarthy, B. G.; Shanmugam, S.; et al. What Happens in the Dark? Assessing the Temporal Control of Photo-Mediated Controlled Radical Polymerizations. *J. Polym. Sci. Part A Polym. Chem.* **2018**, *57*, 268–273.

(72) Femmer, T.; Flack, I.; Wessling, M. Additive Manufacturing in Fluid Process

Engineering. *Chemie-Ingenieur-Technik* **2016**, *88* (5), 535–552.

(73) Martínez, J.; Dumas, J.; Lefebvre, S. Procedural Voronoi Foams for Additive Manufacturing. *ACM Trans. Graph.* **2016**, *35* (4), 12.

(74) Clausen, A.; Wang, F.; Jensen, J. S.; Sigmund, O.; Lewis, J. A. Topology Optimized Architectures with Programmable Poisson's Ratio over Large Deformations. *Adv. Mater.* **2015**, *27* (37), 5523–5527.

(75) Frenzel, T.; Kadic, M.; Wegener, M. Three-Dimensional Mechanical Metamaterials with a Twist. *Science.* **2017**, *358* (6366), 1027–1032.

(76) Hong, S.; Sycks, D.; Chan, H. F. ai; Lin, S.; Lopez, G. P.; Guilak, F.; Leong, K. W.; Zhao, X. 3D Printing of Highly Stretchable and Tough Hydrogels into Complex, Cellularized Structures. *Adv. Mater.* **2015**, *27* (27), 4034.

(77) Kolesky, D. B.; Truby, R. L.; Gladman, A. S.; Busbee, T. A.; Homan, K. A.; Lewis, J. A. 3D Bioprinting of Vascularized, Heterogeneous Cell-Laden Tissue Constructs. *Adv. Mater.* **2014**, *26* (19), 3124–3130.

(78) Basu, A.; Saha, A.; Goodman, C.; Shafranek, R. T.; Nelson, A. Catalytically Initiated Gel-in-Gel Printing of Composite Hydrogels. *ACS Appl. Mater. Interfaces* **2017**, *9* (46), 40898–40904.

(79) Smith, P. T.; Basu, A.; Saha, A.; Nelson, A. Chemical Modification and Printability of Shear-Thinning Hydrogel Inks for Direct-Write 3D Printing. *Polymer.* **2018**, *152*, 42–50.

(80) Sydney Gladman, A.; Matsumoto, E. A.; Nuzzo, R. G.; Mahadevan, L.; Lewis, J. A. Biomimetic 4D Printing. *Nat. Mater.* **2016**, *15* (4), 413–418.

(81) Collino, R. R.; Ray, T. R.; Fleming, R. C.; Cornell, J. D.; Compton, B. G.; Begley,

M. R. Deposition of Ordered Two-Phase Materials Using Microfluidic Print Nozzles with Acoustic Focusing. *Extrem. Mech. Lett.* **2016**, *8*, 96–106.

(82) Kokkins, D.; Schaffner, M.; Studart, A. R. Multimaterial Magnetically Assisted 3D Printing of Composite Materials. *Nat. Commun.* **2015**, *6*, 8643.

(83) Peterson, G. I.; Larsen, M. B.; Ganter, M. A.; Storti, D. W.; Boydston, A. J. 3D-Printed Mechanochromic Materials. *ACS Appl. Mater. Interfaces* **2015**, *7* (1), 577–583.

(84) Peterson, G. I.; Schwartz, J. J.; Zhang, D.; Weiss, B. M.; Ganter, M. A.; Storti, D. W.; Boydston, A. J. Production of Materials with Spatially-Controlled Cross-Link Density via Vat Photopolymerization. *ACS Appl. Mater. Interfaces* **2016**, *8* (42), 29037–29043.

(85) Tumbleston, J. R.; Shirvanyants, D.; Ermoshkin, N.; Janusziewicz, R.; Johnson, A. R.; Kelly, D.; Chen, K.; Pinschmidt, R.; Rolland, J. P.; Ermoshkin, A.; et al. Continuous Liquid Interface Production of 3D Objects. *Science.* **2015**, *347* (6228), 1349–1352.

(86) Choi, J.; Kim, H.; Wicker, R. Multi-Material Stereolithography. *J. Mater. Process. Tech.* **2011**, *211* (3), 318–328.

(87) Ge, Q.; Sakhaei, A. H.; Lee, H.; Dunn, C. K.; Fang, N. X.; Dunn, M. L. Multimaterial 4D Printing with Tailorable Shape Memory Polymers. *Sci. Rep.* **2016**, *6* (1), 31110.

(88) Hardin, J. O.; Ober, T. J.; Valentine, A. D.; Lewis, J. A. Microfluidic Printheads for Multimaterial 3D Printing of Viscoelastic Inks. *Adv. Mater.* **2015**, *27* (21), 3279–3284.

(89) Dolinski, N. D.; Page, Z. A.; Callaway, E. B.; Eisenreich, F.; Garcia, R. V; Chavez, R.; Bothman, D. P.; Hecht, S.; Zok, F. W.; Hawker, C. J. Solution Mask Liquid Lithography ( SMaLL ) for One-Step , Multimaterial 3D Printing. **2018**, *1800364*, 1–6.

# Chapter 2: Fiber-coupled NMR: a versatile approach for *in situ* monitoring of photoswitches and photopolymerizations

This chapter was originally published in *ChemPhotoChem*.
Reproduced with permission from *ChemPhotoChem* **2017**, 1, 4, 125–131.

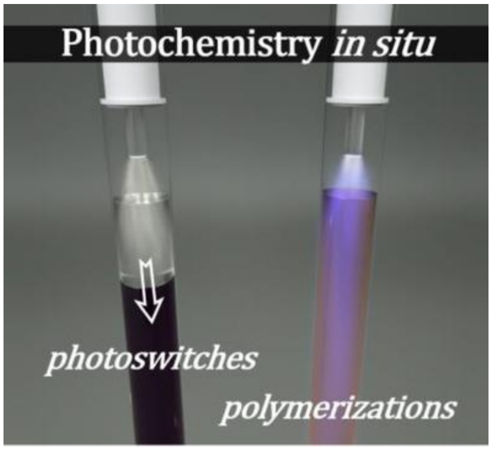

A simple, inexpensive, and modular method to directly illuminate NMR samples for *in situ* analysis of photochemical transformations is reported. The versatility of this technique is demonstrated by analyzing the light-induced propagating front for small-molecule photoswitches and the kinetics of photocontrolled living radical polymerizations. *In situ* measurements allow oxygen-sensitive and rapid photoevents to be studied in detail, leading to reliable determination of photoswitching quantum yields and polymerization rates. By systematically tuning light intensity, a direct relationship between propagation rate and intensity is revealed. Of particular note is the facile translation of the conditions identified through this NMR analysis to analogous benchtop experiments with insight into the nature of the photoreactive species.

---

See Acknowledgments (page iii) for full author list.

Photochemical transformations encompass a wide variety of reactions, including deprotection, acid/base generation, dehalogenation, isomerization, and polymerization, where the absorption and conversion of photon energy is central.[1] Over the past decade, the design of new photochemical switches[2–16] and photopolymerization processes[17–25] has led to functional platforms with applications in actuators, sensing, biology, catalysis, and electronics. A key to these advances has been insight into the mechanism and pathway of the photochemical processes with the most commonly utilized techniques to probe these reactions being ultraviolet-visible (UV/vis) absorption,[15,26] real-time Fourier transform (near) infrared (RT-FT(N)IR) absorption,[25,27,28] and nuclear magnetic resonance (NMR)[8,22,23,29,30] spectroscopies. Although operating effectively at different concentrations, important criteria to consider for each technique include: 1) utilization of probe radiation outside the active range of the system under observation, 2) modular external stimuli (for example temperature and light intensity), 3) technical simplicity and low cost, and 4) high resolution with fast acquisition times (on the order of seconds).

UV/vis-based strategies utilize ultraviolet and visible light as a probe, which is often within the active energy window for stimulating the photochemical process under study, making it undesirable as a monitoring method (especially for sensitive systems). Similarly, RT-FT(N)IR absorption does not provide a high degree of detailed structural information and the desired signals may be diluted by those from overlapping solvent absorption. In contrast, NMR spectroscopy is a common, versatile, and rapid technique, which provides detailed information about molecular structure and composition and uses non-invasive radio frequencies as a probe. Although successful for conventional thermal reactions, a number of issues still persist with employing NMR procedures for the study of photochemical processes. These include relatively high concentrations of NMR experiments (mM range) as compared to UV/vis absorption spectroscopy (μM range), along with manual transfer of a photochemical reaction mixture, or an aliquot thereof, to an NMR tube. As for FT(N)IR approaches, this is time consuming and provides a dataset limited by transfer rate as opposed to measurement acquisition. Moreover, removing aliquots from a reaction can lead to contamination (e.g., oxygen) and continually decreases the volume of the system. Alternatively, direct illumination and monitoring has been accomplished within an NMR spectrometer, either by installing a light source inside the instrument or using an optical fiber, which typically requires probe modification or a coaxial glass insert, respectively.[31–43] The use of light-coupled optical fibers with NMR spectroscopy has distinct advantages from the standpoint of technical simplicity, compatibility with a wide radiation range (UV–IR), and relatively low cost (compared to probe modifications). Apart from traditional coaxial capillary inserts, “pencil tip” inserts[41,42] and fiber-tip etching procedures[31,36] have been utilized to provide uniform light distribution within the NMR measurement zone, but does not lead to the formation of a propagating reaction front needed to determine photoswitch isomerization quantum yield ($\Phi$; see below). However, etching of delicate optical fibers requires harsh conditions, such as the use of hydrofluoric acid, and can be difficult to reproduce, while coaxial capillary inserts often lead to reduced sensitivity.

Herein we report a simple NMR-based technique to monitor photochemical transformations *in situ* using inexpensive and universal optical-fiber inserts, coupled with modular, computer-controlled LED irradiation. To illustrate the utility of this strategy, the $\Phi$ of two photochromic small molecules, a donor–acceptor Stenhouse adduct (DASA)[2,3,26,44–48] as well as a diarylethene (DAE),[5] were determined from optically dense propagating fronts. Complementing the small-molecule studies, this new technique was also used to analyze several light-driven controlled polymerizations, leading to kinetic insights and a detailed understanding of molecular weight, structure, and dispersity evolution with conversion.[25,49–58] These examples showcase the versatility and potential impact of our method on the broad field of photochemistry.

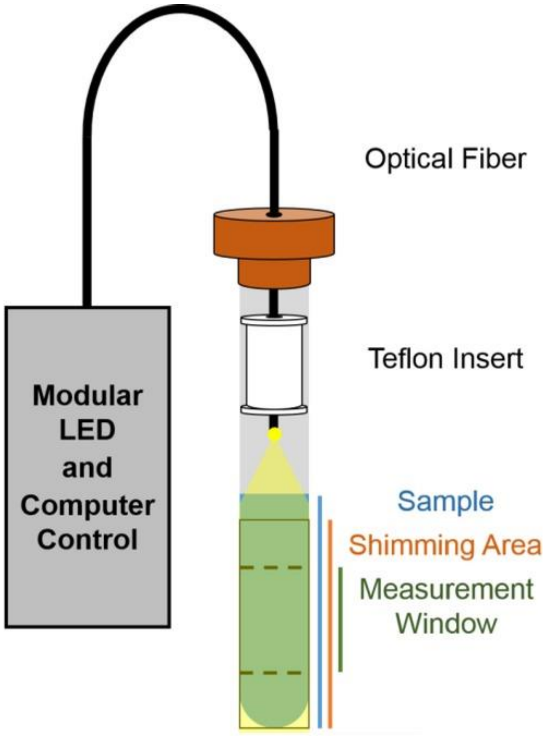

**Figure 2.1:** Schematic representation of the LED system and insert used to uniformly illuminate NMR samples. The setup includes a computer-controlled driver, fiber-coupled LED (with specified wavelength), multimode optical fiber, a Teflon insert for fiber centering, and a standard 5 mm NMR tube.

In this work, a length of optical fiber connected to modular LEDs (Thorlabs) with controllable intensity, is centered over an NMR sample and used to collect real-time data on photochemical transformations. Initial attempts to irradiate samples without centering the fiber tip gave irreproducible results due to non-uniform illumination. To remedy this, a small universal Teflon insert, designed to fit standard 5 mm NMR tubes, allowed for the tip of the optical fiber to be centered directly above the sample, thereby ensuring uniform lateral irradiation during measurement (an engineering drawing of the Teflon insert is provided in **Figure A1** in Appendix A). As compared to typical glass coaxial inserts, the reusable Teflon inserts can be fabricated with simple machinery to keep cost to a minimum and have the added benefit of being both mechanically and chemically robust. Additionally, the LEDs used to illuminate the samples are modular, having tunable light intensities for wavelengths spanning from the deep-UV to far-IR regions, suitable for a wide range of photochemical processes (**Figure 2.1**). The light intensity of the LEDs was controlled by modulating the current output of a commercial LED driver and provided an intensity range from 4 to 66 mW cm$^{-2}$, 4 to 114 mW cm$^{-2}$, 8 to 140 mW cm$^{-2}$, and 6 to 68 mW cm$^{-2}$ for the warm-white (4000 K, $\lambda$≈400–800 nm), violet (405 nm), blue (470 nm), and green (530 nm) LEDs used in these studies, respectively (see **Figure A2** for LED profiles and intensities). Additionally, a LabVIEW program was written to control the light intensity of the LED as well as control light “on” and “off” times for cycling experiments.

Donor–acceptor Stenhouse adducts (DASAs) represent a new class of “negative” or “reverse” photochromes and were selected for initial study due to their high molar absorptivity ($\epsilon$≈100,000 M$^{-1}$ cm$^{-1}$) in the visible range of the spectrum and characteristic $^{1}$H NMR signal shifts upon photoisomerization (**Figure 2.2**).[2,3,48] These features allow the two forms of the DASA switches, that is, the colored “open” triene **1** and the colorless “closed” cyclopentenone **2**, to be identified and tracked throughout the process. Importantly, during the measurement employing irradiation with visible light, it is only the colored form **1**, but not its colorless valence tautomer **2**, which absorbs and thus only ring closure is taking place. Briefly, a 10 mM toluene solution of the open tetrahydroquinoline (THQ) barbituric acid derivative **1** was irradiated using a white LED (46 mW cm$^{-2}$) through the optical fiber/Teflon insert with a circa 2 mm gap between the tip of the fiber and the top of the DASA solution (**Figure 2.2B**; absorption profile **Figure A3**; thermal equilibration **Figure A4**). Due to the high optical density of **1**, 99.9 % of the white light coming from the optical fiber tip is absorbed within the first 10 µm of the solution, with photoisomerization to colorless **2** allowing for the light to progressively penetrate deeper into the solution, generating a front that propagates in a linear fashion over time. This regular propagation rate suggests that the solvent and tube act as an efficient “waveguide” (**Figure A5**), retaining uniform light intensity throughout the measurement. The samples were measured in the dark for two scans (30 s scan$^{-1}$), followed by illumination, with the resulting photochemical transformation being tracked over time by integrating the *N*-methyl protons of the barbituric acid, which shift from $\delta$=3.22 and 3.08 ppm ($H_A$) in **1** to 2.99 and 2.76 ppm ($H_B$) in **2** (**Figure 2.2C**; the full $^{1}$H NMR spectrum is given in **Figure A6**). Plotting the relative fraction of **1** revealed three distinct regions: 1) buffering, where the front has not entered into the measurement window; 2) active, where photoswitching occurs in the measurement window; and 3) post-active, where the front has passed through the measurement window. Notably, a linear front is observed as it moves through the measurement window, in good agreement with video analysis (represented as *X*'s in **Figure 2.3B** and showed as still images in **Figure 2.2B**). The utility of this method was also demonstrated by analyzing front-propagation kinetics with respect to the effective power (considering only light absorbed by **1**). Simple tuning of the LED provided a comprehensive range of irradiation powers to be effectively studied, resulting in a linear relationship from about 4 to 54 mW cm$^{-2}$.

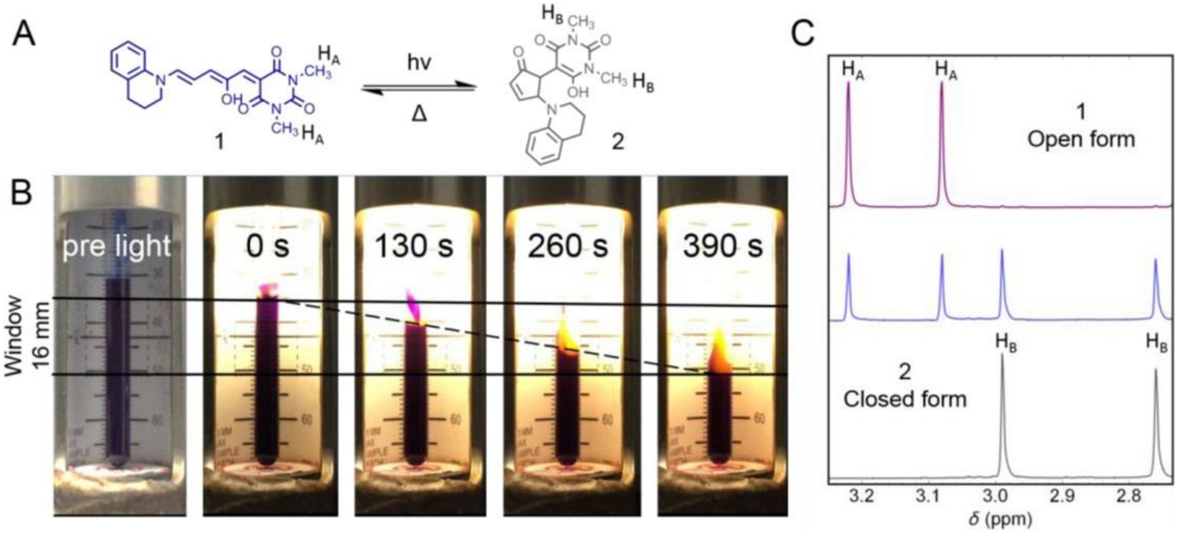

**Figure 2.2:** DASA photoswitching in an NMR tube. A) Chemical structures for tetrahydroquinoline barbituric acid DASA in the open, colored triene form **1** and the closed, colorless cyclopentenone form **2**. B) An optically dense sample of **1** in toluene (10 mM) forming a switching front upon exposure to white light from above (46 mW cm$^{-2}$) that is linear with time. C) $^1$H NMR signals from diagnostic methyl signals of the DASA molecule, used for tracking photoconversion.

Given the complete disappearance of absorption bands in the visible region, these materials follow the equation developed by Pearlstein and Terrones[59] describing idealized photoinitiation fronts from perfectly bleaching molecules [Eq. 1]:

$$S[z,t] = [1 - e^{-\alpha C_o z}(1 - e^{\Phi I_o \alpha t})]^{-1} \qquad (1)$$

where $\alpha$ is the molar extinction coefficient, $C_0$ is the initial concentration, $z$ is the position, $I_0$is the incident photon flux at the surface, $\Phi$ is the quantum yield, and $t$ is time. Though diffusion is not accounted for in Equation (1), numerical solutions for the governing equations yield nearly identical results to those expected for typical small-molecule diffusion coefficients.[60] For solutions where $\alpha$ and $C_0$ are sufficiently large, as is the case for the DASA samples measured here, the front velocity ($V$) simplifies to the following form [Eq. 2]:

$$V = \frac{\Phi I_o}{C_o} \qquad (2)$$

This behavior is independent of the exact $\alpha$ value, which is advantageous given the difficulty associated with measuring $\alpha$ for transient photoswitches (e.g., thermodynamic state not in the colored form). As seen in **Figure 2.3**, the front speed is linear with intensity as predicted by Equation (2). Therefore, the slope of this line can be used to estimate the $\Phi$ value of the switch, which for **1** was found to be 0.15, and opens up interesting questions regarding the associated consequences of DASA structure, solvent polarity, and surrounding temperature on $\Phi$.[26] To the best of our knowledge, this is the first reported use of the above equations for the determination of $\Phi$ for a photoswitchable molecule. To affirm the accuracy of this technique, a classic diarylethene photoswitch (DAE), 1,2-bis[2-methylbenzo[*b*]thiophen-3-yl]-3,3,4,4,5,5-hexafluoro-1-cyclopentene, with a known $\Phi$ (about 0.3)[61–63] was measured (the structure, absorption profile, and $^1$H NMR spectra given in **Figures A3** and **A7**). The previously used white LED was exchanged with a 530 nm LED and photoisomerization of the colored closed form to the colorless open form of DAE in toluene at different light intensities was monitored inside the NMR spectrometer to determine a series of front velocities. A $\Phi$ value of 0.30 for the ring-opening reaction was obtained, which is consistent with literature reports.[61–63] Given the simplicity of the governing equation, Equation (2), this NMR-based method offers significant potential for the rapid screening of otherwise difficult-to-analyze photochromic compounds.[64] In addition, the method is particularly useful for negative photochromic systems, also known as T-type, since NMR allows for convenient measurements at low temperatures, at which the thermal back reaction of the colorless metastable form is slow/negligible.

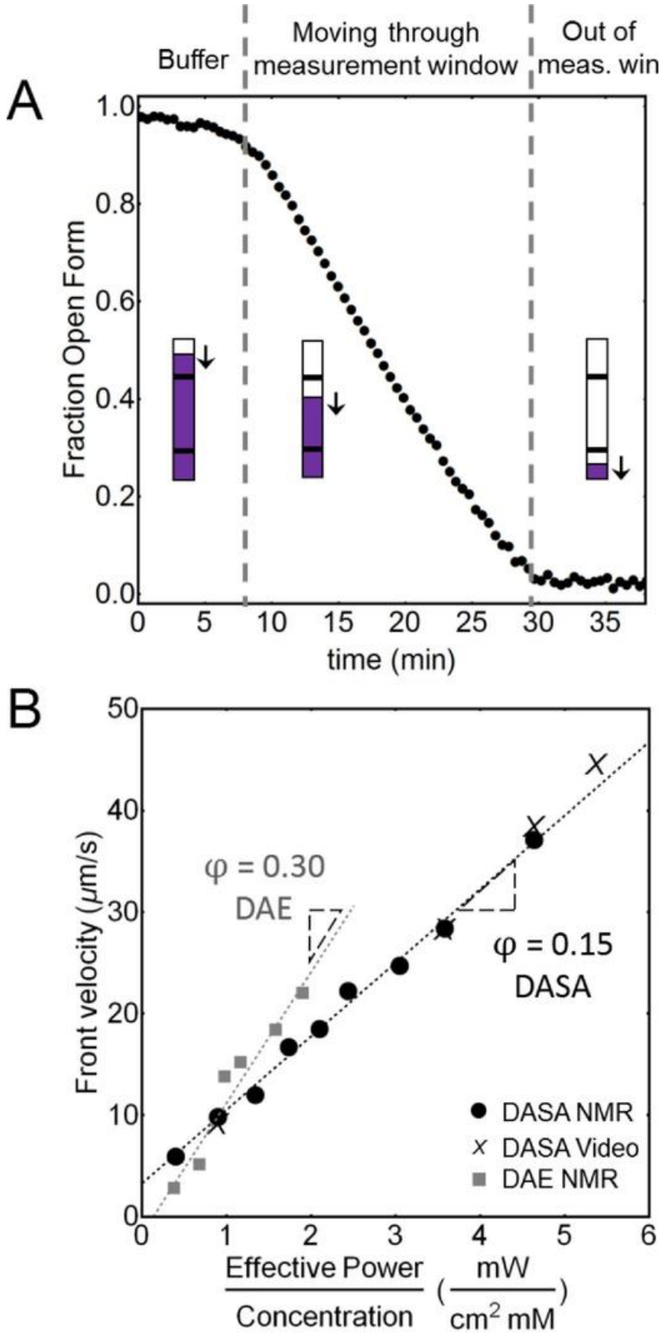

**Figure 2.3:** Monitoring front propagation of a DASA and DAE photoswitch using white and green (530 nm) light, respectively. A) Representative analysis of DASA front propagation with NMR spectroscopy, annotated in three sections: a buffering region, where the front has not entered into the measurement window; an active region, where the front is measured; and a post-active region, where the front has passed through the measurement window. B) Plotting the front velocity versus light power used to switch the sample yields a linear relationship, with the slope equal to $\Phi$ when plotted against photon flux (see Equation (2) and Figure A8).

To further demonstrate the versatility of this technique, several light-driven controlled polymerization systems were subsequently studied (**Figure 2.4A**; NMR spectra provided for all systems in **Figures A9–A11**). Unlike traditional, uncontrolled, polymerizations (such as free radical or polycondensation polymerizations) the use of a controlled or "living" polymerization provides easy access to specifically targeted chain lengths, architectures, and block copolymers by using a reversible capping agent (e.g., chain transfer agent (CTA) or redox-active halogen atom) to maintain a low concentration of reactive radical chain ends. As light-mediated polymerization techniques have received growing attention in recent years, the ability to quickly and accurately screen kinetic behavior is of significant utility to the field.[1,17,20]

Traditionally, methods involving the repeated aliquoting of samples for analysis are used to monitor polymerizations, especially photopolymerizations. This limits the number and distribution of data points, potentially introducing unwanted oxygen, or significantly reducing sample volume, any one of which can skew polymerization kinetic results. A major advantage of this fiber-coupled NMR technique is that a single sample can be monitored *in situ* without perturbing the reaction environment. Such *in situ* monitoring allows facile access to polymerization features such as 1) log-linear propagation rate ($k_p$) over time, 2) temporal control with light "on"/"off" cycles and 3) analysis of the increase in degree of polymerization (DP) with conversion. Finally, it is shown how the ultimate dispersity (Đ) of the polymer chains can be predicted at low conversion by monitoring the CTA.

The photoinduced electron transfer/reversible addition–fragmentation chain transfer (PET-RAFT) polymerization of methyl acrylate (MA) with tris(2,2′-

bipyridyl)dichlororuthenium(II) [Ru(bpy)$_3$Cl$_2$] as the photocatalyst and 2-(butylthiocarbonothioylthio)-2-methylpropionic acid (BTPA) as the CTA was initially chosen for its fast polymerization rate,[25] which would make analysis using traditional techniques challenging (**Figure 2.4A**). As shown in **Figure 2.4B** for light intensities of 8, 35, and 140 mW cm$^{-2}$, the polymerizations exhibited linear growth rates over time, which is expected for controlled, living polymerizations. Increasing the light intensity leads to faster rates of polymerization with $k_p$ values of 0.9, 2.2, and 4.8 h$^{-1}$ being measured for light intensities of 8, 35, and 140 mW cm$^{-2}$, respectively.[25] To translate these measurements to a typical benchtop-scale, batch reaction, a constant light intensity (140 mW cm$^{-2}$) was used with the scale of the polymerization ranging from 0.1 to 3.0 g of MA (**Figure A12**). Significantly, similar $k_p$ values and monomer conversion were observed between the *in situ* NMR experiments and the benchtop polymerizations with both systems showing a correlation between reaction scale and light intensity. This suggests facile transfer of $k_p$ values determined in a small-scale NMR experiment to large-scale batch processes under known irradiation intensities.

Temporal control is a particularly sought-after feature that has been achieved with living photopolymerizations, where aliquots are again traditionally used to monitor chain growth during cycles of light “on” and “off”. Two PET-RAFT systems and one photo-atom transfer radical polymerization (photo-ATRP) system were therefore monitored using this *in situ* NMR strategy and rich kinetic data was acquired during automated “on”/“off” cycling (**Figure 2.4C**). Systems examined were: i) MA, [Ru(bpy)$_3$Cl$_2$] (87 ppm relative to the monomer), and BTPA with 470 nm

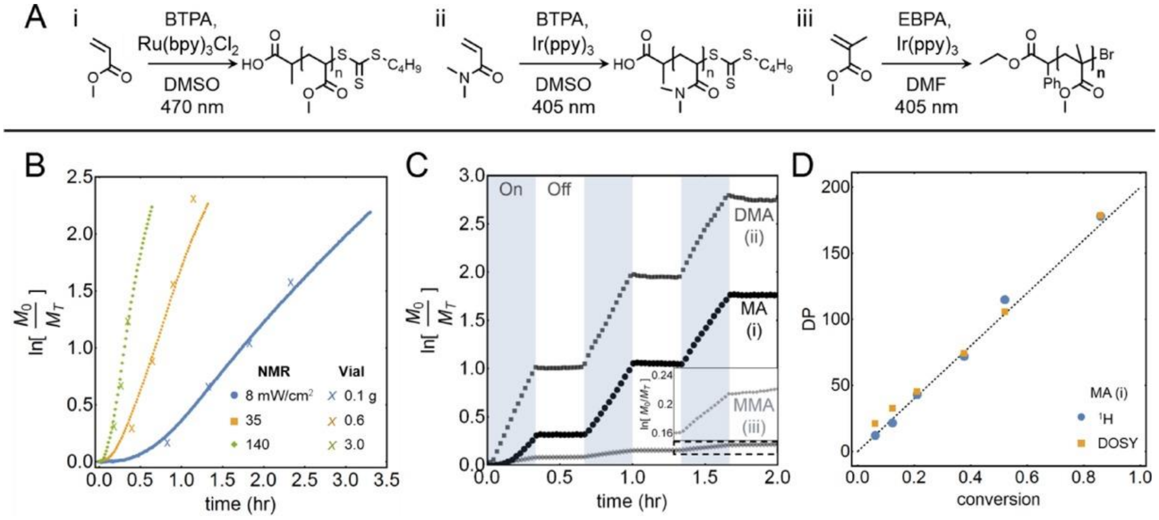

**Figure 2.4:** Monitoring controlled photopolymerization kinetics. A) Reaction scheme for polymerization of i) MA by PET-RAFT, ii) DMA by PET-RAFT, and iii) MMA by photo-ATRP. Kinetic traces of all three polymerization systems are shown in Figure A13. B) Kinetic plot of MA conversion over time at three light intensities, where *X*symbols represent aliquots from representative benchtop reactions at three different scales of monomer, using the highest light intensity. The *X*'s have been shifted to account for the inhibition time present in the NMR samples due to oxygen contamination. C) A series of "on"/"off" plots showing detailed temporal control of (i), (ii), and (iii) where the light intensity and cycles were digitally controlled. D) Degree of polymerization versus conversion determined by $^1$H (blue circles) and DOSY (orange squares) NMR, as well as a theoretical line for (i) targeting a DP of 200.

illumination at 35 mW cm$^{-2}$; ii) *N,N*-dimethylacrylamide (DMA), tris[2-phenylpyridinato-C$^2$,*N*]-iridium(III) [Ir(ppy)$_3$] (66 ppm relative to monomer), and BTPA with 405 nm illumination at 23 mW cm$^{-2}$; and iii) methyl methacrylate (MMA), [Ir(ppy)$_3$] (66 ppm relative to the monomer), and ethyl α-bromophenylacetate illumination at 114 mW cm$^{-2}$ (**Figure 2.4C**). Impressive temporal control is observed for all three systems, where rapid polymerizations halt when the light is turned "off" and begin again within 18 sec of the light being turned "on"; notably, with the same $k_p$ values for each "on" cycle ($k_p$=2.04, 2.92, and 0.13 h$^{-1}$ for MA, DMA, and MMA, respectively).

For "living" polymerizations, DP versus conversion is a linear relationship, and as a final measure of "control" this was determined for PET-RAFT of MA using 1D and

2D NMR spectroscopy (**Figure 2.4D**). $^1$H NMR spectroscopy was used to determine both DP and conversion by comparing the integration of polymer backbone protons and either the polymer chain-end proton located α to the carboxylic acid (for DP) or vinyl monomer protons (for conversion; see **Figures A9-A11**). Six time points were taken and a plot of DP versus conversion revealed a linear relationship, indicative of a "living" polymerization (**Figure 2.4D**). Moreover, diffusion-ordered spectroscopy (DOSY) was used to determine DP relative to poly(methyl methacrylate) (PMMA) standards and show the compatibility of this technique with 2D NMR spectroscopy. Diffusion coefficients (D) were measured during six "off" cycles and interpolated in a PMMA calibration curve to determine DP (corresponding details are given in Appendix A, see **Table A1** and **Figures A14 and A15**). The results again show a linear relationship, with the data being consistent with that obtained from 1D NMR spectroscopy. The ability to monitor photopolymerizations in real time using 1D and 2D NMR spectroscopy is a powerful combination, and can be used to provide additional information from a single photopolymerization sample, including intrinsic viscosity ($\eta$), weight average molecular weight ($M_w$), and Đ.[65,66]

One of the unique advantages of NMR analysis is the ability to identify and monitor specific molecular entities in reaction mixtures. In this case, the $^1$H NMR signals from the CTA were visible and on insertion of one or more acrylate units, a distinct change in the chemical shift ($\delta$), in particular for the proton located α to the trithiocarbonate group ($H_C$ to $H_D$), is observed (**Figure 2.5**). Complete reaction of the CTA leading to the trithiocarbonate chain ends of the growing polymers (that is, initiation) is an important aspect for RAFT, as the rate of initiation must greatly exceed propagation for a controlled/living polymerization. Fast consumption of the CTA leads to narrower Đ and a more controlled process. Upon examination of the NMR spectra for the polymerization, described in **Figure 2.4B**, the conversion at which all CTA was incorporated into the monomer chain ends increased with catalyst loading from 13, to 16, to 20 % for 44, 87 and 175 ppm (relative to monomer), respectively (marked by *X* symbols in **Figure 2.5B**). Table 2.1 shows the molecular weight and Đ data obtained from gel permeation chromatography (GPC). As predicted, the increased catalyst loadings, which had higher conversion for complete CTA incorporation, have a larger Đ value, increasing from 1.14 to 1.24, and 1.30 for 44, 87, and 175 ppm catalyst loadings, respectively (**Figure A16**). The ability to simply measure these trends with high-molecular-weight precision is made possible by this technique and is the first time a photomediated controlled polymerization process has been monitored in real time using NMR spectroscopy.

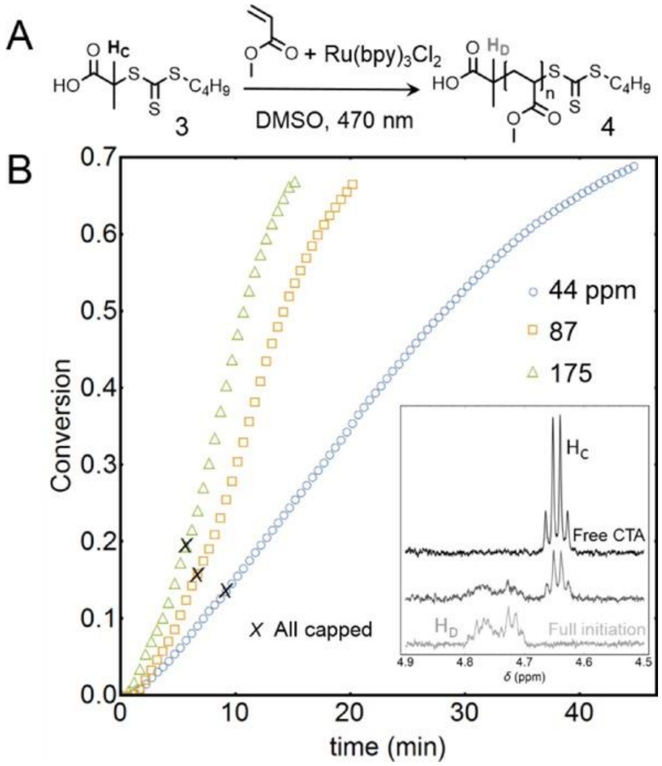

**Figure 2.5:** Monitoring CTA incorporation at different catalyst loadings relative to monomer. A) Reaction scheme denoting the observable chemical shift when going from the intact small molecule ($H_C$) to the fully incorporated CTA ($H_D$). B) Plots of conversion versus time, with the point of full CTA incorporation marked with an X. Inset: NMR signals used to determine CTA conversion.

**Table 2.1:** Results from the CTA study shown in Figure 2.5. Polymerizations were carried out to 70 % monomer conversion in all cases and molecular weights and dispersities were measured using GPC in chloroform relative to polystyrene standards.

| [Ru(bpy)$_3$Cl$_2$] [ppm] | Time [min] | $M_n$[a] [kDa] | $M_p$[a] [kDa] | Đ |
|---|---|---|---|---|
| 44 | 45 | 9.7 | 11.1 | 1.14 |
| 87 | 21 | 8.5 | 10.7 | 1.24 |
| 175 | 15 | 8.3 | 11.3 | 1.30 |

## Conclusions

In summary, a method to monitor photochemical transformations with *in situ* NMR spectroscopy using fiber-coupled LEDs and reusable Teflon inserts was presented. Observing the front propagation of optically dense DASA and DAE photoswitch solutions led to a unique way of determining reaction quantum yields, while rich kinetic data on PET-RAFT of MA revealed different levels of polymerization "control" as well as a relative prediction for dispersity of the growing polymer chains. By removing the requirement for obtaining aliquots to monitor reactions in a rather invasive manner, our direct and non-invasive technique serves to streamline researchers' efforts to analyze new photochemical processes. As shown here, basic one-dimensional NMR spectroscopy can be insightful with this novel illumination technique being easily used in combination with two-dimensional NMR spectroscopy to provide more complex structural, compositional, and dynamic information. It is anticipated that this method will be beneficial for future developments in both small molecule and polymer photochemistry.

## References

(1) Corrigan, N.; Shanmugam, S.; Xu, J.; Boyer, C. Photocatalysis in Organic and Polymer Synthesis. *Chem. Soc. Rev.* **2016**, *45* (22), 6165–6212.

(2) Helmy, S.; Oh, S.; Leibfarth, F. A.; Hawker, C. J.; Read De Alaniz, J. Design and Synthesis of Donor-Acceptor Stenhouse Adducts: A Visible Light Photoswitch Derived from Furfural. *J. Org. Chem.* **2014**, *79* (23), 11316–11329.

(3) Helmy, S.; Leibfarth, F. A.; Oh, S.; Poelma, J. E.; Hawker, C. J.; Read de Alaniz, J. Photoswitching Using Visible Light: A New Class of Organic Photochromic Molecules. *J. Am. Chem. Soc.* **2014**, *136* (23), 8169−8172.

(4) Brieke, C.; Rohrbach, F.; Gottschalk, A.; Mayer, G.; Heckel, A. Light-Controlled Tools. *Angew. Chemie - Int. Ed.* **2012**, *51* (34), 8446–8476.

(5) Irie, M.; Fukaminato, T.; Matsuda, K.; Kobatake, S. Photochromism of Diarylethene Molecules and Crystals: Memories, Switches, and Actuators. *Chem. Rev.* **2014**, *114* (24), 12174–12277.

(6) Bandara, H. M. D.; Burdette, S. C. Photoisomerization in Different Classes of Azobenzene. *Chem. Soc. Rev.* **2012**, *41* (5), 1809–1825.

(7) Olejniczak, J.; Carling, C. J.; Almutairi, A. Photocontrolled Release Using One-Photon Absorption of Visible or NIR Light. *J. Control. Release* **2015**, *219*, 18–30.

(8) Mallo, N.; Brown, P. T.; Iranmanesh, H.; MacDonald, T. S. C.; Teusner, M. J.; Harper, J. B.; Ball, G. E.; Beves, J. E. Photochromic Switching Behaviour of Donor-Acceptor Stenhouse Adducts in Organic Solvents. *Chem. Commun.* **2016**, *52* (93), 13576–13579.

(9) Szymański, W.; Beierle, J. M.; Kistemaker, H. A. V.; Velema, W. A.; Feringa, B. L. Reversible Photocontrol of Biological Systems by the Incorporation of Molecular Photoswitches. *Chem. Rev.* **2013**, *113* (8), 6114–6178.

(10) Kawata, S.; Kawata, Y. Three-Dimensional Optical Data Storage Using Photochromic Materials. *Chem. Rev.* **2000**, *100* (5), 1777–1788.

(11) Russew, M. M.; Hecht, S. Photoswitches: From Molecules to Materials. *Adv. Mater.* **2010**, *22* (31), 3348–3360.

(12) Bléger, D.; Hecht, S. Visible-Light-Activated Molecular Switches. *Angew. Chemie - Int. Ed.* **2015**, *54* (39), 11338–11349.

(13) Orgiu, E.; Samorì, P. 25th Anniversary Article: Organic Electronics Marries Photochromism: Generation of Multifunctional Interfaces, Materials, and Devices. *Adv. Mater.* **2014**, *26* (12), 1827–1844.

(14) Göstl, R.; Senf, A.; Hecht, S. Remote-Controlling Chemical Reactions by Light: Towards Chemistry with High Spatio-Temporal Resolution. *Chem. Soc. Rev.* **2014**, *43* (6), 1982–1996.

(15) Klajn, R. Spiropyran-Based Dynamic Materials. *Chem. Soc. Rev.* **2014**, *43* (1), 148–184.

(16) Zhang, J.; Zou, Q.; Tian, H. Photochromic Materials: More than Meets the Eye. *Adv. Mater.* **2013**, *25* (3), 378–399.

(17) Theriot, J. C.; Lim, C.-H.; Yang, H.; Ryan, M. D.; Musgrave, C. B.; Miyake, G. M. Organocatalyzed Atom Transfer Radical Polymerization Driven by Visible Light. *Science.* **2016**, *352* (6289), 1082–1086.

(18) Chen, M.; Johnson, J. A. Improving Photo-Controlled Living Radical

Polymerization from Trithiocarbonates through the Use of Continuous-Flow Techniques. *Chem. Commun.* **2015**, *51* (31), 6742–6745.

(19) Zhao, Y.; Zhang, S.; Wu, Z.; Liu, X.; Zhao, X.; Peng, C. H.; Fu, X. Visible-Light-Induced Living Radical Polymerization (LRP) Mediated by (Salen)Co(II)/TPO at Ambient Temperature. *Macromolecules* **2015**, *48* (15), 5132–5139.

(20) Pan, X.; Malhotra, N.; Simakova, A.; Wang, Z.; Konkolewicz, D.; Matyjaszewski, K. Photoinduced Atom Transfer Radical Polymerization with Ppm-Level Cu Catalyst by Visible Light in Aqueous Media. *J. Am. Chem. Soc.* **2015**, *137* (49), 15430–15433.

(21) Shanmugam, S.; Xu, J.; Boyer, C. Light-Regulated Polymerization under Near-Infrared / Far-Red Irradiation Catalyzed by Bacteriochlorophyll A. *Angew. Chemie Int. Ed.* **2016**, *55*, 1036–1040.

(22) Kermagoret, A.; Wenn, B.; Debuigne, A.; Jérôme, C.; Junkers, T.; Detrembleur, C. Improved Photo-Induced Cobalt-Mediated Radical Polymerization in Continuous Flow Photoreactors. *Polym. Chem.* **2015**, *6* (20), 3847–3857.

(23) Treat, N. J.; Sprafke, H.; Kramer, J. W.; Clark, P. G.; Barton, B. E.; Read De Alaniz, J.; Fors, B. P.; Hawker, C. J. Metal-Free Atom Transfer Radical Polymerization. *J. Am. Chem. Soc.* **2014**, *136* (45), 16096–16101.

(24) Fors, B. P.; Hawker, C. J. Control of a Living Radical Polymerization of Methacrylates by Light. *Angew. Chemie - Int. Ed.* **2012**, *51* (35), 8850–8853.

(25) Xu, J.; Jung, K.; Boyer, C. Oxygen Tolerance Study of Photoinduced Electron Transfer–Reversible Addition–Fragmentation Chain Transfer (PET-RAFT) Polymerization Mediated by Ru(Bpy) $_3$ Cl $_2$. *Macromolecules* **2014**, *47* (13),

4217–4229.

(26) Lerch, M. M.; Wezenberg, S. J.; Szymanski, W.; Feringa, B. L. Unraveling the Photoswitching Mechanism in Donor-Acceptor Stenhouse Adducts. *J. Am. Chem. Soc.* **2016**, *138* (20), 6344–6347.

(27) Chiou, B.-S.; Khan, S. A. Real-Time FTIR and *in Situ* Rheological Studies on the UV Curing Kinetics of Thiol-Ene Polymers. *Macromolecules* **1997**, *30* (23), 7322–7328.

(28) Shi, S.; Allonas, X.; Croutxé-Barghorn, C.; Chemtob, A. Activation of the Sol-Gel Process by Visible Light-Emitting Diodes (LEDs) for the Synthesis of Inorganic Films. *New J. Chem.* **2015**, *39* (7), 5686–5693.

(29) Tait, K. M.; Parkinson, J. A.; Gibson, D. I.; Richardson, P. R.; Ebenezer, W. J.; Hutchings, M. G.; Jones, A. C. Structural Characterisation of the Photoisomers of Reactive Sulfonated Azo Dyes by NMR Spectroscopy and DFT Calculations. *Photochem. Photobiol. Sci.* **2007**, *6* (9), 1010–1018.

(30) Evans, R. A.; Hanley, T. L.; Skidmore, M. A.; Davis, T. P.; Such, G. K.; Yee, L. H.; Ball, G. E.; Lewis, D. A. The Generic Enhancement of Photochromic Dye Switching Speeds in a Rigid Polymer Matrix. *Nat. Mater.* **2005**, *4* (3), 249–253.

(31) Kuprov, I.; Hore, P. J. Uniform Illumination of Optically Dense NMR Samples. *J. Magn. Reson.* **2004**, *171* (1), 171–175.

(32) Feldmeier, C.; Bartling, H.; Magerl, K.; Gschwind, R. M. LED-Illuminated NMR Studies of Flavin-Catalyzed Photooxidations Reveal Solvent Control of the Electron-Transfer Mechanism. *Angew. Chemie - Int. Ed.* **2015**, *54* (4), 1347–1351.

(33) Kolmer-Anderl, N.; Kolmer, A.; Thiele, C. M.; Rehahn, M. Exploration of the Photodegradation of Naphtho[2,3-g] Quinoxalines and Pyrazino[2,3-b]Phenazines. *Chem. - A Eur. J.* **2016**, *22* (15), 5277–5287.

(34) Kind, J.; Kaltschnee, L.; Leyendecker, M.; Thiele, C. M. Distinction of Trans-Cis Photoisomers with Comparable Optical Properties in Multiple-State Photochromic Systems-Examining a Molecule with Three Azobenzenes via in Situ Irradiation NMR Spectroscopy. *Chem. Commun.* **2016**, *52* (84), 12506–12509.

(35) Geftakis, S.; Ball, G. E. Direct Observation of a Transition Metal Alkane Complex, CpRe(CO)2(Cyclopentane), Using NMR Spectroscopy [7]. *J. Am. Chem. Soc.* **1998**, *120* (38), 9953–9954.

(36) Feldmeier, C.; Bartling, H.; Riedle, E.; Gschwind, R. M. LED Based NMR Illumination Device for Mechanistic Studies on Photochemical Reactions – Versatile and Simple, yet Surprisingly Powerful. *J. Magn. Reson.* **2013**, *232*, 39–44.

(37) Mills, A.; O’Rourke, C. In Situ, Simultaneous Irradiation and Monitoring of a Photocatalyzed Organic Oxidation Reaction in a TiO2-Coated NMR Tube. *J. Org. Chem.* **2015**, *80* (20), 10342–10345.

(38) Bliumkin, L.; Dutta Majumdar, R.; Soong, R.; Adamo, A.; Abbatt, J. P. D.; Zhao, R.; Reiner, E.; Simpson, A. J. Development of an in Situ NMR Photoreactor to Study Environmental Photochemistry. *Environ. Sci. Technol.* **2016**, *50* (11), 5506–5516.

(39) Kuprov, I.; Goez, M.; Abbott, P. A.; Hore, P. J. Design and Performance of a

Microsecond Time-Resolved Photo-Chemically Induced Dynamic Nuclear Polarization Add-on for a High-Field Nuclear Magnetic Resonance Spectrometer. *Rev. Sci. Instrum.* **2005**, *76* (8), 1–7.

(40) Callies, R.; Altenburger, R.; Mayer, A.; Grimme, L. H.; Leibfritz, D. A New Illumination System for in Vivo NMR Spectroscopy. *J. Magn. Reson.* **1990**, *90* (3), 561–566.

(41) Kühn, T.; Schwalbe, H. Monitoring the Kinetics of Ion-Dependent Protein Folding by Time-Resolved NMR Spectroscopy at Atomic Resolution. *J. Am. Chem. Soc.* **2000**, *122* (26), 6169–6174.

(42) Wirmer, J.; Kühn, T.; Schwalbe, H. Millisecond Time Resolved Photo-CIDNP NMR Reveals a Non-Native Folding Intermediate on the Ion-Induced Refolding Pathway of Bovine α-Lactalbumin. *Angew. Chemie - Int. Ed.* **2001**, *40* (22), 4248–4251.

(43) Wolff, C.; Kind, J.; Schenderlein, H.; Bartling, H.; Feldmeier, C.; Gschwind, R. M.; Biesalski, M.; Thiele, C. M. Studies of a Photochromic Model System Using NMR with Ex-Situ and in-Situ Irradiation Devices. *Magn. Reson. Chem.* **2016**, *54* (6), 485–491.

(44) Mason, B. P.; Whittaker, M.; Hemmer, J.; Arora, S.; Harper, A.; Alnemrat, S.; McEachen, A.; Helmy, S.; Read De Alaniz, J.; Hooper, J. P. A Temperature-Mapping Molecular Sensor for Polyurethane-Based Elastomers. *Appl. Phys. Lett.* **2016**, *108* (4).

(45) Singh, S.; Friedel, K.; Himmerlich, M.; Lei, Y.; Schlingloff, G.; Schober, A. Spatiotemporal Photopatterning on Polycarbonate Surface through Visible

Light Responsive Polymer Bound DASA Compounds. *ACS Macro Lett.* **2015**, *4* (11), 1273–1277.

(46) Poelma, S. O.; Oh, S. S.; Helmy, S.; Knight, A. S.; Burnett, G. L.; Soh, H. T.; Hawker, C. J.; Read De Alaniz, J. Controlled Drug Release to Cancer Cells from Modular One-Photon Visible Light-Responsive Micellar System. *Chem. Commun.* **2016**, *52* (69), 10525–10528.

(47) Balamurugan, A.; Lee, H. A Visible Light Responsive On–Off Polymeric Photoswitch for the Colorimetric Detection of Nerve Agent Mimics in Solution and in the Vapor Phase. *Macromolecules* **2016**, *49* (7), 2568–2574.

(48) Hemmer, J. R.; Poelma, S. O.; Treat, N.; Page, Z. A.; Dolinski, N. D.; Diaz, Y. J.; Tomlinson, W.; Clark, K. D.; Hooper, J. P.; Hawker, C.; et al. Tunable Visible and Near Infrared Photoswitches. *J. Am. Chem. Soc.* **2016**, *138* (42), 13960–13966.

(49) Fu, C.; Xu, J.; Kokotovic, M.; Boyer, C. One-Pot Synthesis of Block Copolymers by Orthogonal Ring-Opening Polymerization and PET-RAFT Polymerization at Ambient Temperature. *ACS Macro Lett.* **2016**, *5* (4), 444–449.

(50) Shanmugam, S.; Xu, J.; Boyer, C. Exploiting Metalloporphyrins for Selective Living Radical Polymerization Tunable over Visible Wavelengths. *J. Am. Chem. Soc.* **2015**, *137* (28), 9174–9185.

(51) Xu, J.; Shanmugam, S.; Boyer, C. Organic Electron Donor-Acceptor Photoredox Catalysts: Enhanced Catalytic Efficiency toward Controlled Radical Polymerization. *ACS Macro Lett.* **2015**, *4* (9), 926–932.

(52) Yeow, J.; Xu, J.; Boyer, C. Polymerization-Induced Self-Assembly Using Visible

Light Mediated Photoinduced Electron Transfer-Reversible Addition-Fragmentation Chain Transfer Polymerization. *ACS Macro Lett.* **2015**, *4* (9), 984–990.

(53) Jung, K.; Xu, J.; Zetterlund, P. B.; Boyer, C. Visible-Light-Regulated Controlled/Living Radical Polymerization in Miniemulsion. *ACS Macro Lett.* **2015**, *4* (10), 1139–1143.

(54) Shanmugam, S.; Xu, J.; Boyer, C. Photoinduced Electron Transfer-Reversible Addition-Fragmentation Chain Transfer (PET-RAFT) Polymerization of Vinyl Acetate and N-Vinylpyrrolidinone: Kinetic and Oxygen Tolerance Study. *Macromolecules* **2014**, *47* (15), 4930–4942.

(55) Xu, J.; Shanmugam, S.; Duong, H. T.; Boyer, C. Organo-Photocatalysts for Photoinduced Electron Transfer-Reversible Addition-Fragmentation Chain Transfer (PET-RAFT) Polymerization. *Polym. Chem.* **2015**, *6* (31), 5615–5624.

(56) Yeow, J.; Sugita, O. R.; Boyer, C. Visible Light-Mediated Polymerization-Induced Self-Assembly in the Absence of External Catalyst or Initiator. *ACS Macro Lett.* **2016**, *5* (5), 558–564.

(57) Corrigan, N.; Xu, J.; Boyer, C. A Photoinitiation System for Conventional and Controlled Radical Polymerization at Visible and NIR Wavelengths. *Macromolecules* **2016**, *49* (9), 3274–3285.

(58) Shanmugam, S.; Xu, J.; Boyer, C. Utilizing the Electron Transfer Mechanism of Chlorophyll a under Light for Controlled Radical Polymerization. *Chem. Sci.* **2015**, *6* (2), 1341–1349.

(59) Terrones, G.; Pearlstein, A. J. Effects of Optical Attenuation and Consumption

of a Photobleaching Initiator on Local Initiation Rates in Photopolymerizations. *Macromolecules* **2001**, *34* (10), 3195–3204.

(60) Miller, G. A.; Gou, L.; Narayanan, V.; Scranton, A. B. Modeling of Photobleaching for the Photoinitiation of Thick Polymerization Systems. *J. Polym. Sci. Part A Polym. Chem.* **2002**, *40* (6), 793–808.

(61) Uchida, K.; Tsuchida, E.; Aoi, Y.; Nakamura, S.; Irie, M. Substitution Effect on the Coloration Quantum Yield of a Photochromic Bisbenzothienylethene. *Chem. Lett.* **1999**, *28* (1), 63–64.

(62) Sumi, T.; Takagi, Y.; Yagi, A.; Morimoto, M.; Irie, M. Photoirradiation Wavelength Dependence of Cycloreversion Quantum Yields of Diarylethenes. *Chem. Commun.* **2014**, *50* (30), 3928–3930.

(63) Ishibashi, Y.; Umesato, T.; Fujiwara, M.; Une, K.; Yoneda, Y.; Sotome, H.; Katayama, T.; Kobatake, S.; Asahi, T.; Irie, M.; et al. Solvent Polarity Dependence of Photochromic Reactions of a Diarylethene Derivative As Revealed by Steady-State and Transient Spectroscopies. *J. Phys. Chem. C* **2016**, *120* (2), 1170–1177.

(64) Note: As a General Guide, an Absorbance Value over 2000 a.u. Should Be Used to Assure a Linear Front and Minimal Penetration Depth, Giving Access to Equation (2).

(65) Li, W.; Chung, H.; Daeffler, C.; Johnson, J. A.; Grubbs, R. H. Application Of1H DOSY for Facile Measurement of Polymer Molecular Weights. *Macromolecules* **2012**, *45* (24), 9595–9603.

(66) Viéville, J.; Tanty, M.; Delsuc, M. A. Polydispersity Index of Polymers Revealed by DOSY NMR. *J. Magn. Reson.* **2011**, *212* (1), 169–173.

# Chapter 3: What happens in the dark? Assessing the temporal control of photo-mediated controlled radical polymerizations

This chapter was originally published in the *Journal of Polymer Science Part A*. Reproduced with permission from *J. Polym. Sci. Part A: Polym. Chem.* **2019**, 57, 3, 268–273. Copyright 2019, John Wiley and Sons

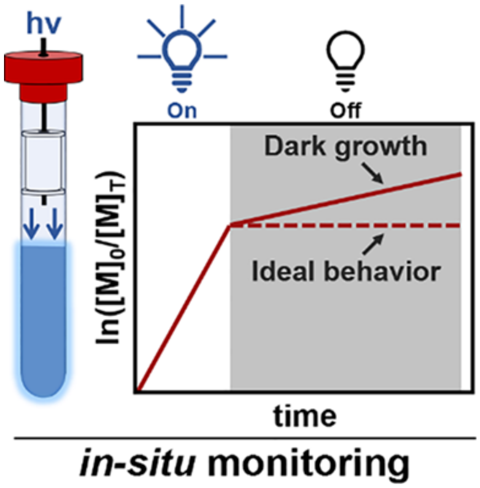

A signature of photo-mediated controlled polymerizations is the ability to modulate the rate of polymerization by turning the light source ‘on’ and ‘off.’ However, in many reported systems, growth can be reproducibly observed during dark periods. In this study, emerging photo-mediated controlled radical polymerizations are evaluated with *in situ* $^1$H NMR monitoring to assess their behavior in the dark. Interestingly, it is observed that Cu-mediated systems undergo long-lived, linear growth during dark periods in organic media.

---

See Acknowledgments (page iii) for full author list.

The utility and sweeping impact of controlled radical polymerization (CRP) has fundamentally changed the direction of polymer synthesis. By enabling the accurate control of molecular weight, architecture, and dispersity (Đ) for a wide variety of functional monomers, the facile synthesis of complex polymeric materials such as extended multiblocks[1], surface-modified nanoparticles[2,3], and bioconjugates[4–6] is now possible. Recently, the use of external stimuli, such as light[7,8], reducing agents[9], applied voltage[10], and mechanical forces[11] to mediate CRP processes has further increased the usefulness and impact of CRP.[12] Of these stimuli, light is particularly attractive, as it is environmentally benign and highly tunable.[13–15] Numerous examples of photo-mediated controlled radical polymerization (photo-CRP) have recently been developed, including Cu-mediated reversible-deactivation radical polymerization (Cu-mediated RDRP)[16–19], Cu-free atom transfer radical polymerization (Cu-free ATRP)[8,17,20–22], and photo induced electron transfer-reversible addition-fragmentation chain transfer (PET-RAFT).[23,24] These systems operate over a wide variety of wavelengths and employ a variety of catalysts to polymerize different monomer classes,[25–27] with the broad scope of these systems leading to the development of well-defined, functional materials. Notable examples include patterned polymer brushes[28,29], organic light-emitting diodes[30], soft gels[31,32], and complex polymer architectures[33,34].

In photo-CRP, temporal control is typically demonstrated through sequential ‘on’ - ‘off’ cycles. This cycling is performed by irradiating the reaction mixture, polymerization then initiates/propagates, followed by a ‘dark’ period

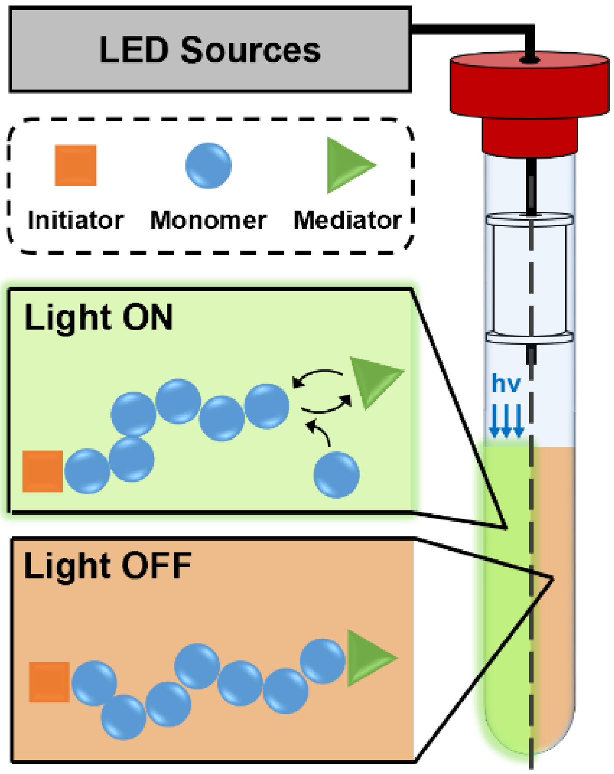

**Figure 3.1**: Schematic of the *in situ* fiber-coupled NMR system showing idealized schemes for photo-CRP in active ('on') and dormant ('off') states.

where, in an ideal scenario, no additional conversion takes place. However, for many reported photo-CRP systems, a small yet reproducible amount of polymer growth can be observed during the 'off' cycles.[22,35–39] This apparent growth has been attributed to several factors, from experimental error to residual active catalyst. While the kinetics of growth and the presence of side reactions has been extensively studied for 'on' periods[5,40,41], no systematic examination of the polymerization reaction during the 'off' or 'dark' periods has been conducted.

To address this challenge and provide insight into photo-CRP processes, a recently developed *in situ* NMR spectroscopy method is utilized to evaluate temporal control for a selection of widely studied photo-CRP processes (see **Figure 3.1** and **Figure B1** for a representative schematic and photograph of the setup).[42]

Compared to conventional sampling methods, this approach is uniquely suited for studying temporal control of photo-CRPs, allowing accurate modulation of irradiation intensity and wavelength through the combination of LEDs and fiber optics. In addition, *in situ* coupling with NMR spectroscopy permits rapid and repeated measurements to be taken without invasive sampling of the polymerization reaction. As a result, accurate polymerization kinetics can be obtained in both the ‘on’ and ‘off’ states.

In this study, PET-RAFT, Cu-free ATRP, and Cu-mediated RDRP systems were selected as representative examples of photo-CRP methods. To facilitate an unbiased comparison across techniques, irradiation conditions were held constant (equivalent photon flux) and polymerization conditions, such as monomer concentration and targeted degree of polymerization, were fixed at 33 wt% and DP=150. Temporal control experiments were also carried out with equal ‘on’ and ‘off’ times targeting conversions of ~40% with an initial ‘off’ period conducted to establish a baseline before exposure to light. To show the general trends of a given technique, a representative catalyst/ligand combination will be discussed, however full data for all catalysts studied is available in Appendix B.

**Scheme 1:** Simplified mechanisms reported for a) PET-RAFT / Cu-free ATRP and b) Cu-mediated RDRP. See review by Johnson and co-workers[13] for in-depth discussions of the above photo-CRP mechanisms.

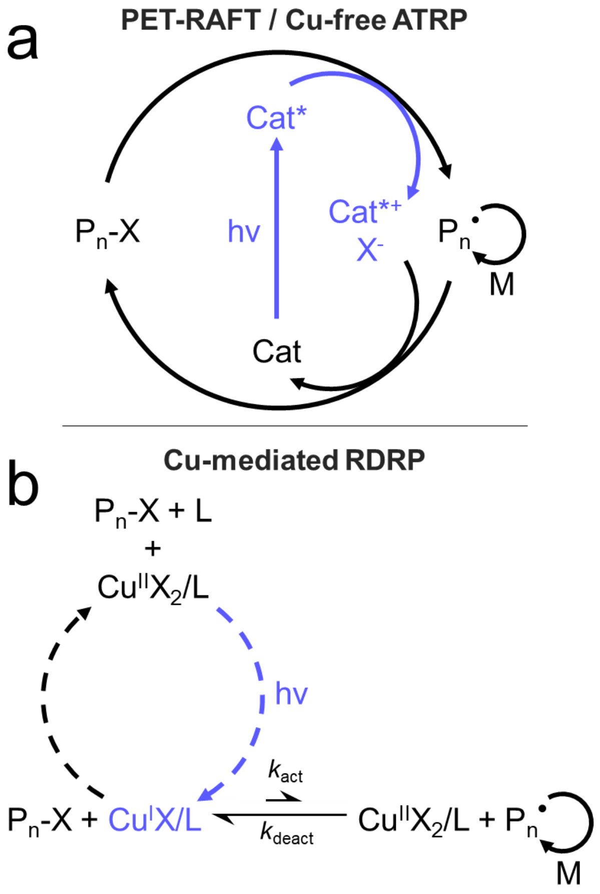

As they both utilize the photocatalyst as an electron transfer agent, the initial systems chosen for study were PET-RAFT and Cu-free ATRP, Scheme 1a.[43] Under traditional PET-RAFT conditions, the polymerization of methyl acrylate (MA) in DMSO was examined, (**Figure 3.2a**) and after an inhibition period attributed to residual oxygen being consumed,[24,44,45] the polymerization demonstrated linear kinetics with significant deviation from linearity only observed at high monomer conversions (**Figure 3.2b**). As expected, the polymerization of methyl methacrylate (MMA) under Cu-free ATRP conditions (**Figure 3.3a**) was slower than the polymeri-

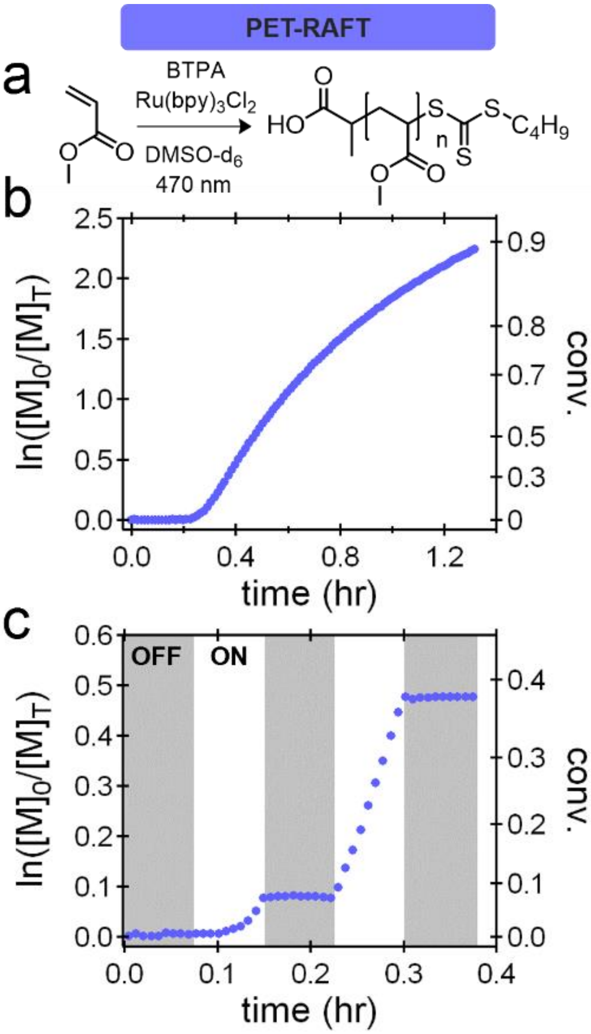

**Figure 3.2:** a) PET-RAFT conditions for the polymerization of methyl acrylate (MA) using 470 nm light and tris(2,2′-bipyridyl)dichlororuthenium(II) hexahydrate. b) Kinetic plots of the polymerizations at a fixed photon flux. c) Temporal control experiments for the PET-RAFT demonstrate ideal temporal control.

zation of MA by PET-RAFT due to the increased $k_p$ values. However, in both the PET-RAFT and Cu-free ATRP experiments, linear kinetics with little to no deviation were observed up to conversions of 30–40%. To simplify comparison, this conversion range was thereby targeted in the temporal control studies (**Figure 3.2c**, **3.3c**). Significantly, for all PET-RAFT and Cu-free ATRP systems studied, high

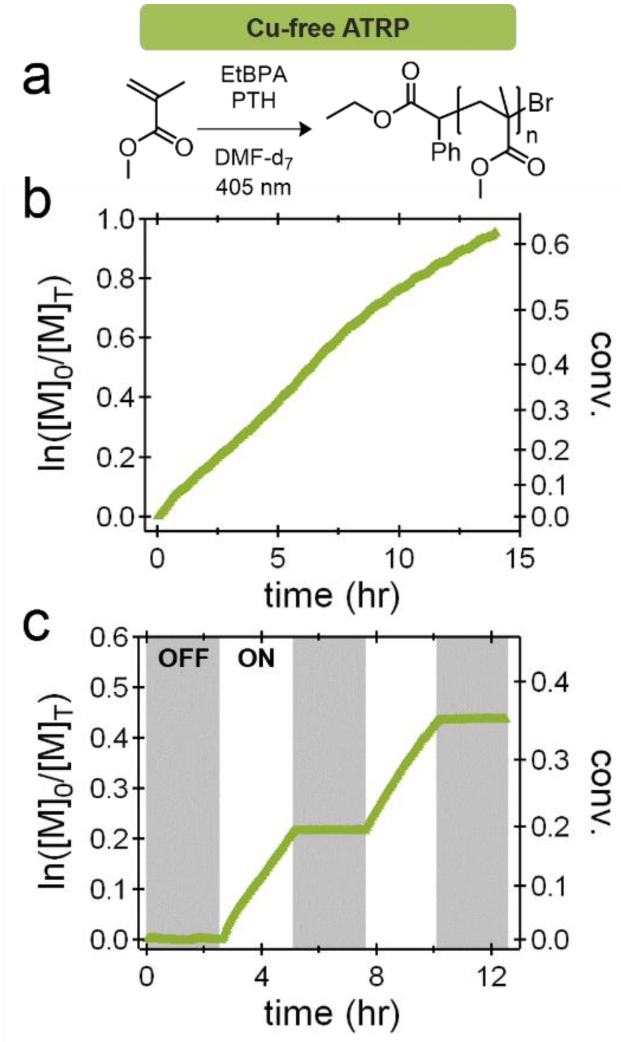

**Figure 3.3:** a) Cu-free ATRP conditions for the polymerization of methyl methacrylate (MMA) using 405 nm light and 10-phenylphenothiazine. b) Kinetic plots of the polymerizations at a fixed photon flux. c) Temporal control experiments for the Cu-free ATRP reactions demonstrate ideal temporal control.

fidelity is observed with no observable conversion being measured during the ‘dark’ period.

Unlike PET-RAFT and Cu-free ATRP, which directly drive polymerization through light-driven electron transfer events, Cu-mediated RDRP in a secondary fashion, generating active Cu(I) from inactive Cu(II), potentially leaving residual catalytic Cu(I) in solution after irradiation has stopped, Scheme 1b. To examine this behavior and compare Cu-mediated RDRP to both PET-RAFT and Cu-free ATRP, $Me_6$TREN

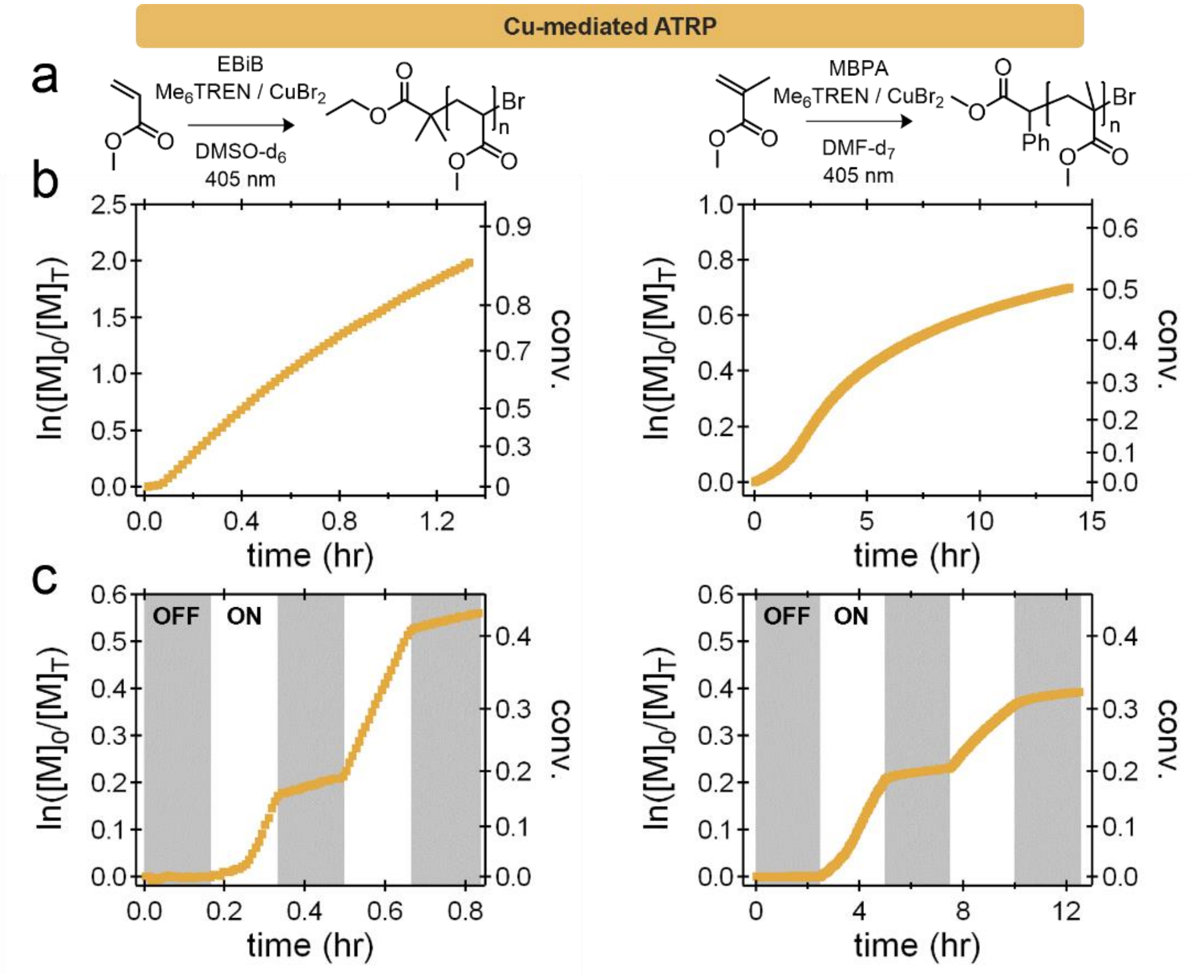

**Figure 3.4**: a) Cu-mediated RDRP conditions for the polymerization of MA and MMA using $CuBr_2$ and tris[2-(dimethylamino)ethyl]amine ($Me_6TREN$). b) Kinetic plots of the polymerizations at a fixed photon flux. c) Temporal control experiments wherein distinct linear growth during dark periods after initial irradiation are observed for both polymerizations (~10–15% of the ‘on‘ rate).

and $CuBr_2$ were employed in the polymerization of both MA and MMA (**Figure 3.4a**). Although there are differences in the overall behavior of the polymerization of MA and MMA compared to the PET-RAFT and Cu-free ATRP examples, namely a lack of inhibition for MA and evidence of severe termination for MMA, both systems show linear kinetics up to monomer conversions of ~30–40% (**Figure 3.4b**).

For both MA and MMA, significant differences were observed during ‘off’ periods (**Figure 3.4c**). While the initial ‘dark’ periods did not result in any monomer conversion, the Cu-mediated systems exhibited substantial polymer growth during the subsequent ‘dark’ periods (~5–10% of the ‘on’ rate in both the MA and MMA systems). Interestingly, upon extending the dark window from ~10 minutes to ~5 hours, linear polymerization kinetics in the ‘off’ state are still observed. Even at high conversions, the Cu catalyst was active with linear kinetics being observed (86 to 91%) despite being in an ‘off’ or ‘dark’ period for 3.5 hours (**Figure B24**). These results suggest that during the ‘off’ periods a significant amount of Cu(I) (initially produced by reduction of Cu(II)) remains in solution and is responsible for polymer growth through a conventional ATRP mechanism, rather than a photo-mediated ATRP process. To further investigate the temporal control of Cu-mediated RDRP systems, the dark periods were extended for different Cu/ligand pairs ($Me_6TREN$ and TPMA). The equilibrium constants for $Me_6TREN$ and TPMA are reported in the literature, and it has been shown that TPMA has a $K_{ATRP}$ value approximately an order of magnitude lower than $Me_6TREN$.[46] After initial irradiation to similar conversions, both systems did show growth during the ‘dark’ period. However, $Me_6TREN$ displays a considerably higher rate of conversion (approximately an order of magnitude) when compared to the corresponding TPMA system (**Figure 3.5**). This result illustrates that Cu-mediated RDRP in organic media does not exhibit ideal temporal control for any of the conditions/ligands studied due to the unwanted presence and extended lifetime of CuBr during 'dark' periods.

To improve the temporal control of Cu- mediated polymerizations, we envisage that a system must exhibit rapid consumption of residual Cu(I) catalyst during the 'off' cycles. Aqueous systems are subject to high equilibrium constants,[47,48] and the concentration of Cu(I) should therefore decrease rapidly during 'dark' periods, translating to increased temporal control relative to the corresponding organic systems. As a control, Cu-mediated RDRP of poly(ethylene glycol) methyl ether acrylate (PEGA, $M_n$ = 480) using $Me_6TREN/CuBr_2$ was conducted in organic and aqueous media (**Figure 3.6**). In analogy with the Cu-mediated polymerization of MA

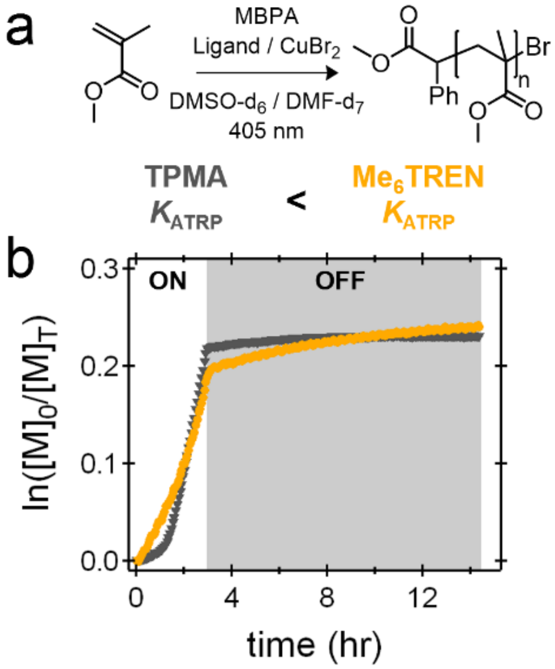

**Figure 3.5**: Kinetics of MMA polymerizations using $Me_6TREN/CuBr_2$ (DMF-$d_7$) and $TPMA/CuBr_2$ (DMSO-$d_6$) photosystems at equal loadings. $Me_6TREN$ undergoes more growth in the dark period due to its higher activity ($K_{ATRP}$).

in DMSO, a linear increase in conversion for PEGA occurs during an extended ‘dark’ period of ~5 hours after initial irradiation (**Figure 3.6b**). To achieve a comparable controlled polymerization of PEGA in water, the copper loading was increased 5x relative to that used in DMSO.[48] Interestingly, after irradiation with 365 nm light, rapid polymerization continued for 2 hours in the dark (though in a non-linear fashion) before decreasing to undetectable levels. Importantly, the polymerization continued upon further irradiation, highlighting that the end groups were still active and implying that the active Cu(I) was consumed during the ‘off’ period, presumably by conversion to Cu(II). While this aqueous system demonstrated the potential for improved temporal control compared to a similar polymerization in organic media, significant monomer conversion does occur in the ‘dark’ after turning off the light source. In an attempt to increase fidelity further, it was hypothesized that a lower amount of initial $CuBr_2$ would generate less residual catalyst, which could then be deactivated more rapidly in the absence of light. In order to maintain control with a reduced amount of $CuBr_2$, NaBr was therefore added to the polymerization mixture.[48] Indeed, under these conditions, nearly immediate cessation of the polymerization was observed upon switching the light ‘off,’ leading to a high degree of temporal control. These results highlight the importance of mechanistic understanding in the development of strategies for temporal control of Cu-mediated CRP processes.

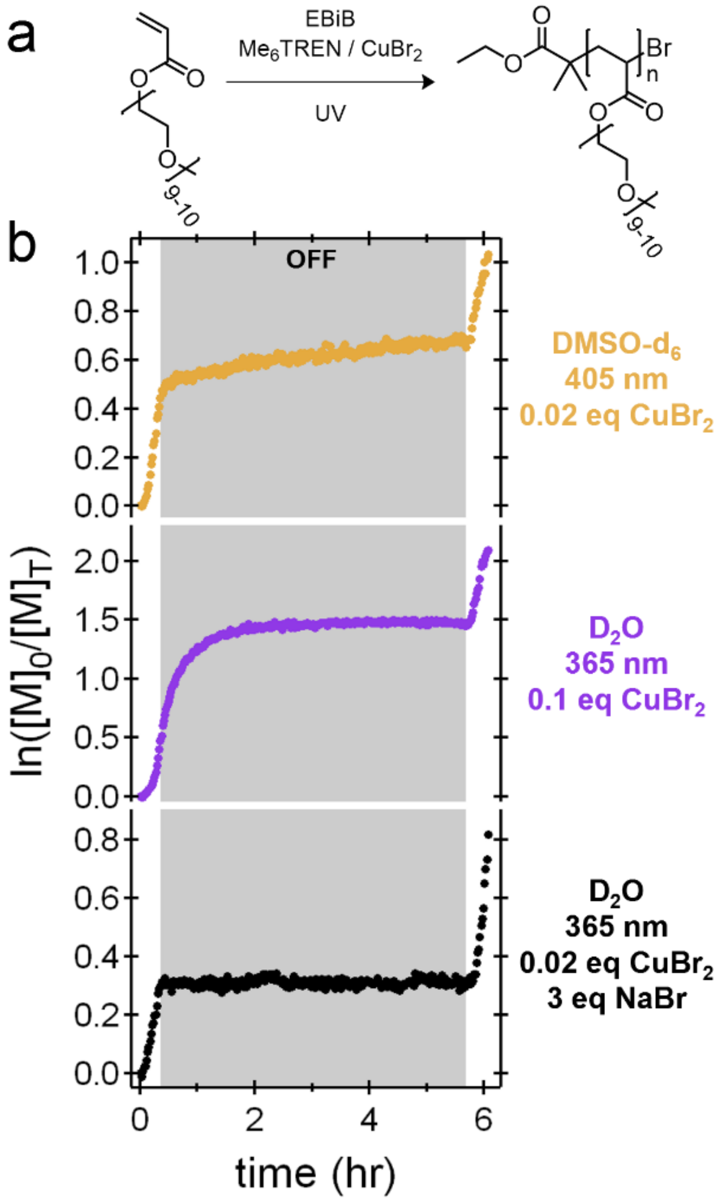

**Figure 3.6**: a) General reaction scheme for polymerization of poly(ethylene glycol) methyl ether acrylate (PEGA) macromonomers. b) Temporal experiments for PEGA polymerized in DMSO (top), water at an elevated Cu concentration (middle), and water with a reduced Cu content and NaBr (bottom). Only the reduced Cu-concentration aqueous polymerization shows ideal temporal behavior.

## Conclusions

In summary, a modular *in situ* NMR technique was utilized to investigate monomer conversion during the ‘on’ and ‘off’ cycles for a selection of photo-CRP procedures. Temporal control during metal-free ATRP and PET-RAFT was demonstrated to have high fidelity and little to no conversion during ‘dark’ periods. In direct contrast, Cu-mediated polymerizations conducted in DMSO showed significant growth during ‘off’ cycles, which is attributed to the increased lifetime of residual Cu(I) catalyst after initial photoactivation. The use of aqueous conditions (low Cu(II) concentration and added NaBr) quickly consumes the residual catalytic species and alleviates this problem. This allows well-controlled polymers with no observable ‘dark’ growth to be obtained. However, it should be noted that these conditions cannot currently be broadly generalized with understanding and improving the temporal control in Cu-mediated polymerizations in organic media being an area of future focus. The findings of non-ideal temporal behaviour herein also illustrate the necessity for employing long ‘off’ periods when studying temporal control to ensure measurement fidelity and accuracy.

## References

(1) Chuang, Y. M.; Ethirajan, A.; Junkers, T. Photoinduced Sequence-Controlled Copper-Mediated Polymerization: Synthesis of Decablock Copolymers. *ACS Macro Lett.* **2014**, *3* (8), 732–737.

(2) Skaff, H.; Emrick, T. Reversible Addition Fragmentation Chain Transfer (RAFT) Polymerization from Unprotected Cadmium Selenide Nanoparticles. *Angew. Chemie - Int. Ed.* **2004**, *43* (40), 5383–5386.

(3) Babin, J.; Lepage, M.; Zhao, Y. “Decoration” of Shell Cross-Linked Reverse Polymer Micelles Using ATRP: A New Route to Stimuli-Responsive Nanoparticles. *Macromolecules* **2008**, *41* (4), 1246–1253.

(4) Niu, J.; Lunn, D. J.; Pusuluri, A.; Yoo, J. I.; O’Malley, M. A.; Mitragotri, S.; Soh, H. T.; Hawker, C. J. Engineering Live Cell Surfaces with Functional Polymers via Cytocompatible Controlled Radical Polymerization. *Nat. Chem.* **2017**, *9* (6), 537–545.

(5) Niu, J.; Page, Z. A.; Dolinski, N. D.; Anastasaki, A.; Hsueh, A. T.; Soh, H. T.; Hawker, C. J. Rapid Visible Light-Mediated Controlled Aqueous Polymerization with in Situ Monitoring. *ACS Macro Lett.* **2017**, *6* (10), 1109–1113.

(6) Xu, J.; Jung, K.; Corrigan, N. A.; Boyer, C. Aqueous Photoinduced Living/Controlled Polymerization: Tailoring for Bioconjugation. *Chem. Sci.* **2014**, *5* (9), 3568–3575.

(7) Shi, Y.; Liu, G.; Gao, H.; Lu, L.; Cai, Y. Effect of Mild Visible Light on Rapid Aqueous RAFT Polymerization of Water-Soluble Acrylic Monomers at

Ambient Temperature: Initiation and Activation. *Macromolecules* **2009**, *42* (12), 3917–3926.

(8) Fors, B. P.; Hawker, C. J. Control of a Living Radical Polymerization of Methacrylates by Light. *Angew. Chemie - Int. Ed.* **2012**, *51* (35), 8850–8853.

(9) Jakubowski, W.; Matyjaszewski, K. Activator Generated by Electron Transfer for Atom Transfer Radical Polymerization. *Macromolecules* **2005**, *38* (10), 4139–4146.

(10) Magenau, A. J. D.; Strandwitz, N. C.; Gennaro, A.; Matyjaszewski, K. Electrochemically Mediated Atom Transfer Radical Polymerization. *Science.* **2011**, *332*, 81–84.

(11) Mohapatra, H.; Kleiman, M.; Esser-Kahn, A. P. Mechanically Controlled Radical Polymerization Initiated by Ultrasound. *Nat. Chem.* **2017**, *9* (2), 135–139.

(12) Pan, X.; Fantin, M.; Yuan, F.; Matyjaszewski, K. Externally Controlled Atom Transfer Radical Polymerization. *Chem. Soc. Rev.* **2018**, *47* (14), 5457–5490.

(13) Chen, M.; Zhong, M.; Johnson, J. A. Light-Controlled Radical Polymerization: Mechanisms, Methods, and Applications. *Chem. Rev.* **2016**, *116* (17), 10167–10211.

(14) Pan, X.; Tasdelen, M. A.; Laun, J.; Junkers, T.; Yagci, Y.; Matyjaszewski, K. Photomediated Controlled Radical Polymerization. *Prog. Polym. Sci.* **2016**, *62*, 73–125.

(15) Corrigan, N.; Shanmugam, S.; Xu, J.; Boyer, C. Photocatalysis in Organic and Polymer Synthesis. *Chem. Soc. Rev.* **2016**, *45* (22), 6165–6212.

(16) Konkolewicz, D.; Schröder, K.; Buback, J.; Bernhard, S.; Matyjaszewski, K.

Visible Light and Sunlight Photoinduced ATRP with Ppm of Cu Catalyst. *ACS Macro Lett.* **2012**, *1* (10), 1219–1223.

(17) Kork, S.; Ciftci, M.; Tasdelen, M. A.; Yagci, Y. Photoinduced Cu(0)-Mediated Atom Transfer Radical Polymerization. *Macromol. Chem. Phys.* **2016**, *217* (6), 812–817.

(18) Frick, E.; Anastasaki, A.; Haddleton, D. M.; Barner-Kowollik, C. Enlightening the Mechanism of Copper Mediated PhotoRDRP via High-Resolution Mass Spectrometry. *J. Am. Chem. Soc.* **2015**, *137* (21), 6889–6896.

(19) Nikolaou, V.; Anastasaki, A.; Brandford-Adams, F.; Whitfield, R.; Jones, G. R.; Nurumbetov, G.; Haddleton, D. M. Discrete Copper( <scp>ii</Scp> )-Formate Complexes as Catalytic Precursors for Photo-Induced Reversible Deactivation Polymerization. *Polym. Chem.* **2016**, *7* (1), 191–197.

(20) Treat, N. J.; Sprafke, H.; Kramer, J. W.; Clark, P. G.; Barton, B. E.; Read De Alaniz, J.; Fors, B. P.; Hawker, C. J. Metal-Free Atom Transfer Radical Polymerization. *J. Am. Chem. Soc.* **2014**, *136* (45), 16096–16101.

(21) Theriot, J. C.; Lim, C.-H.; Yang, H.; Ryan, M. D.; Musgrave, C. B.; Miyake, G. M. Organocatalyzed Atom Transfer Radical Polymerization Driven by Visible Light. *Science.* **2016**, *352* (6289), 1082–1086.

(22) Pearson, R. M.; Lim, C. H.; McCarthy, B. G.; Musgrave, C. B.; Miyake, G. M. Organocatalyzed Atom Transfer Radical Polymerization Using N-Aryl Phenoxazines as Photoredox Catalysts. *J. Am. Chem. Soc.* **2016**, *138* (35), 11399–11407.

(23) Shanmugam, S.; Xu, J.; Boyer, C. Photoinduced Electron Transfer-Reversible Addition-Fragmentation Chain Transfer (PET-RAFT) Polymerization of Vinyl

Acetate and N-Vinylpyrrolidinone: Kinetic and Oxygen Tolerance Study. *Macromolecules* **2014**, *47* (15), 4930–4942.

(24) Fu, Q.; Xie, K.; McKenzie, T. G.; Qiao, G. G. Trithiocarbonates as Intrinsic Photoredox Catalysts and RAFT Agents for Oxygen Tolerant Controlled Radical Polymerization. *Polym. Chem.* **2017**, *8* (9), 1519–1526.

(25) Kottisch, V.; Michaudel, Q.; Fors, B. P. Cationic Polymerization of Vinyl Ethers Controlled by Visible Light. *J. Am. Chem. Soc.* **2016**, *138* (48), 15535–15538.

(26) Michaudel, Q.; Kottisch, V.; Fors, B. P. Cationic Polymerization: From Photoinitiation to Photocontrol. *Angew. Chemie - Int. Ed.* **2017**, *56* (33), 9670–9679.

(27) Michaudel, Q.; Chauviré, T.; Kottisch, V.; Supej, M. J.; Stawiasz, K. J.; Shen, L.; Zipfel, W. R.; Abruña, H. D.; Freed, J. H.; Fors, B. P. Mechanistic Insight into the Photocontrolled Cationic Polymerization of Vinyl Ethers. *J. Am. Chem. Soc.* **2017**, *139* (43), 15530–15538.

(28) Poelma, J. E.; Fors, B. P.; Meyers, G. F.; Kramer, J. W.; Hawker, C. J. Fabrication of Complex Three-Dimensional Polymer Brush Nanostructures through Light-Mediated Living Radical Polymerization. *Angew. Chemie - Int. Ed.* **2013**, *52* (27), 6844–6848.

(29) Discekici, E. H.; Pester, C. W.; Treat, N. J.; Lawrence, J.; Mattson, K. M.; Narupai, B.; Toumayan, E. P.; Luo, Y.; McGrath, A. J.; Clark, P. G.; et al. Simple Benchtop Approach to Polymer Brush Nanostructures Using Visible-Light-Mediated Metal-Free Atom Transfer Radical Polymerization. *ACS Macro Lett.* **2016**, *5* (2), 258–262.

(30) Page, Z. A.; Narupai, B.; Pester, C. W.; Bou Zerdan, R.; Sokolov, A.; Laitar, D. S.; Mukhopadhyay, S.; Sprague, S.; McGrath, A. J.; Kramer, J. W.; et al. Novel Strategy for Photopatterning Emissive Polymer Brushes for Organic Light Emitting Diode Applications. *ACS Cent. Sci.* **2017**, *3* (6), 654–661.

(31) Chen, M.; Gu, Y.; Singh, A.; Zhong, M.; Jordan, A. M.; Biswas, S.; Korley, L. T. J.; Balazs, A. C.; Johnson, J. A. Living Additive Manufacturing: Transformation of Parent Gels into Diversely Functionalized Daughter Gels Made Possible by Visible Light Photoredox Catalysis. *ACS Cent. Sci.* **2017**, *3* (2), 124–134.

(32) Daniel, W. F. M.; Burdyńska, J.; Vatankhah-varnoosfaderani, M.; Matyjaszewski, K.; Paturej, J.; Rubinstein, M.; Dobrynin, A. V; Sheiko, S. S. Solvent-Free , Supersoft and Superelastic Bottlebrush Melts and Networks. **2016**, *15* (November 2015), 183–190.

(33) Chen, M.; MacLeod, M. J.; Johnson, J. A. Visible-Light-Controlled Living Radical Polymerization from a Trithiocarbonate Iniferter Mediated by an Organic Photoredox Catalyst. *ACS Macro Lett.* **2015**, *4* (5), 566–569.

(34) Wenn, B.; Martens, A. C.; Chuang, Y.-M.; Gruber, J.; Junkers, T. Efficient Multiblock Star Polymer Synthesis from Photo-Induced Copper-Mediated Polymerization with up to 21 Arms. *Polym. Chem.* **2016**, 2720–2727.

(35) Tasdelen, M. A.; Uygun, M.; Yagci, Y. Photoinduced Controlled Radical Polymerization in Methanol. *Macromol. Chem. Phys.* **2010**, *211* (21), 2271–2275.

(36) Reeves, J. A.; Allegrezza, M. L.; Konkolewicz, D. Rise and Fall: Poly (Phenyl Vinyl Ketone) Photopolymerization and Photodegradation under Visible and

UV Radiation. *Macromol. Rapid Commun.* **2017**, *38* (13), 1–5.

(37) Anastasaki, A.; Nikolaou, V.; Zhang, Q.; Burns, J.; Samanta, S. R.; Waldron, C.; Haddleton, A. J.; McHale, R.; Fox, D.; Percec, V.; et al. Copper(II)/Tertiary Amine Synergy in Photoinduced Living Radical Polymerization: Accelerated Synthesis of ω-Functional and α,ω-Heterofunctional Poly(Acrylates). *J. Am. Chem. Soc.* **2014**, *136* (3), 1141–1149.

(38) Anastasaki, A.; Nikolaou, V.; Brandford-Adams, F.; Nurumbetov, G.; Zhang, Q.; Clarkson, G. J.; Fox, D. J.; Wilson, P.; Kempe, K.; Haddleton, D. M. Photo-Induced Living Radical Polymerization of Acrylates Utilizing a Discrete Copper(II)-Formate Complex. *Chem. Commun.* **2015**, *51* (26), 5626–5629.

(39) Discekici, E. H.; Anastasaki, A.; Kaminker, R.; Willenbacher, J.; Truong, N. P.; Fleischmann, C.; Oschmann, B.; Lunn, D. J.; Read De Alaniz, J.; Davis, T. P.; et al. Light-Mediated Atom Transfer Radical Polymerization of Semi-Fluorinated (Meth)Acrylates: Facile Access to Functional Materials. *J. Am. Chem. Soc.* **2017**, *139* (16), 5939–5945.

(40) McKenzie, T. G.; Costa, L. P. da M.; Fu, Q.; Dunstan, D. E.; Qiao, G. G. Investigation into the Photolytic Stability of RAFT Agents and the Implications for Photopolymerization Reactions. *Polym. Chem.* **2016**, *7* (25), 4246–4253.

(41) Ryan, M. D.; Pearson, R. M.; French, T. A.; Miyake, G. M. Impact of Light Intensity on Control in Photoinduced Organocatalyzed Atom Transfer Radical Polymerization. *Macromolecules* **2017**, *50* (12), 4616–4622.

(42) Dolinski, N. D.; Page, Z. A.; Eisenreich, F.; Niu, J.; Hecht, S.; Read de Alaniz, J.; Hawker, C. J. A Versatile Approach for In Situ Monitoring of Photoswitches and Photopolymerizations. *ChemPhotoChem* **2017**, *1* (4), 125–131.

(43) Theriot, J. C.; Miyake, G. M.; Boyer, C. A. N,N‐Diaryl Dihydrophenazines as Photoredox Catalysts for PET-RAFT and Sequential PET-RAFT/O-ATRP. *ACS Macro Lett.* **2018**, *7*, 662–666.

(44) Xu, J.; Jung, K.; Atme, A.; Shanmugam, S.; Boyer, C. A Robust and Versatile Photoinduced Living Polymerization of Conjugated and Unconjugated Monomers and Its Oxygen Tolerance. *J. Am. Chem. Soc.* **2014**, *136* (14), 5508–5519.

(45) Gormley, A. J.; Yeow, J.; Ng, G.; Conway, Ó.; Boyer, C.; Chapman, R. An Oxygen-Tolerant PET-RAFT Polymerization for Screening Structure–Activity Relationships. *Angew. Chemie - Int. Ed.* **2018**, *57* (6), 1557–1562.

(46) Wang, Y.; Kwak, Y.; Buback, J.; Buback, M.; Matyjaszewski, K. Determination of ATRP Equilibrium Constants under Polymerization Conditions. *ACS Macro Lett.* **2012**, *1* (12), 1367–1370.

(47) Simakova, A.; Averick, S. E.; Konkolewicz, D.; Matyjaszewski, K. Aqueous ARGET ATRP. *Macromolecules* **2012**, *45* (16), 6371–6379.

(48) Jones, G. R.; Whitfield, R.; Anastasaki, A.; Haddleton, D. M. Aqueous Copper(II) Photoinduced Polymerization of Acrylates: Low Copper Concentration and the Importance of Sodium Halide Salts. *J. Am. Chem. Soc.* **2016**, *138* (23), 7346–7352.

# Chapter 4: Solution Mask Liquid Lithography (SMaLL) for One-Step, Multimaterial 3D Printing

This chapter was originally published in *Advanced Materials*.
Reproduced with permission from *Adv. Mater.* **2018**, 30, 31, 1800364.

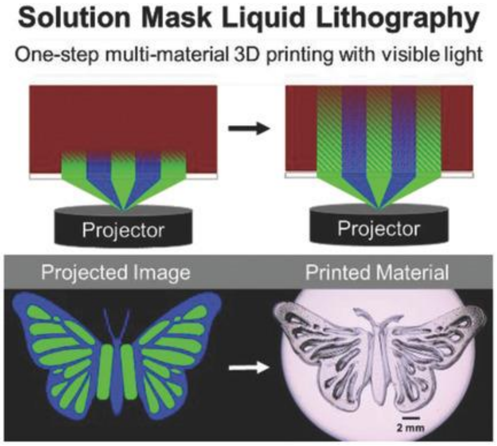

A novel methodology for printing 3D objects with spatially resolved mechanical and chemical properties is reported. Photochromic molecules are used to control polymerization through coherent bleaching fronts, providing large depths of cure and rapid build rates without the need for moving parts. The coupling of these photoswitches with resin mixtures containing orthogonal photocrosslinking systems allows for simultaneous and selective curing of multiple networks, providing access to 3D-objects with chemically and mechanically distinct domains. The power of this approach is showcased through the one-step fabrication of bioinspired soft joints and mechanically reinforced “brick-and-mortar” structures.

---

See Acknowledgments (page iii) for full author list.

The ability to rapidly convert digital designs into 3D-objects through direct printing is revolutionizing fundamental scientific discovery and commercial fabrication of industrial materials.[1–6] While traditional systems print objects using a single starting material, multi-material printing has emerged as a particularly attractive avenue to design advanced materials with unique properties (e.g., polymer-polymer composites). This interest is inspired by natural systems where numerous examples of hierarchical multi-material structures have been observed, including wood, nacre, and abalone shells. In these systems, synergy between domains with disparate properties leads to significant mechanical enhancement, providing, for example, strong and lightweight objects.[7,8] The ability to produce synthetic systems based on these biological motifs would significantly impact the 3D printing field, enabling access to desirable engineering properties, such as crack resistance, impact toughness, *etc*. To-date, a major challenge in realizing this goal has been the development of resins incorporating multiple photochemical reactions that allows for spatial resolution and orthogonal crosslinking. The ability to control these independent processes would permit hierarchical structures with mechanically distinct and orientated domains (*e.g.*, stiff/flexible) to be fabricated.

To address this challenge, techniques have recently emerged for 3D-printing of a variety of soft multi-material objects based on diverse building blocks, such as composite structures of polymer matrices with aligned filler particles, mixtures of soft and hard curing resins, and hydrogels containing live cells. This structural diversity impacts applications ranging from soft robotics to tissue engineering.[8–18] Currently, the printing of these multi-material systems is accomplished using complex equipment with multiple single component inks, resins, or thermoplastic filaments. An additional challenge with these systems is the tendency to fail at the various material interfaces due to undesirable mechanical anisotropy.[3] In overcoming these shortcomings, Boydston[19], Lefebvre[20], and Lewis[21] have developed strategies to 3D print materials with multiple mechanical responses using single resin stocks, thereby eliminating inter-material layering. These state-of-the-art examples use greyscale irradiation for mechanical gradation[19], programmable anisotropy of foams[20], and two-layer direct ink writing for selective swelling[21]. However, the reliance on a single curing reaction limits the range of chemical and mechanical properties that can be achieved for these systems. The development of a rapid and continuous multi-material printing methodology using resins based on multiple, orthogonal crosslinking reactions (*i.e.*, radical/cationic curing) is therefore highly desirable.

The present work describes the development of orthogonal photochemistries that undergo independent crosslinking/photoswitching reactions upon irradiation with different wavelengths of visible light. The ability to selectively control reactions based on wavelength[22] allows materials with diverse, and spatially defined chemical and mechanical properties to be prepared. The approach, termed Solution Mask Liquid Lithography (SMaLL), takes advantage of coherent photobleaching fronts arising from the use of mixtures of photochromic molecules (solution masks), to provide rapid build rates, large depths of cure, excellent feature resolution, and 3D-objects with no layering defects.

Traditional light-driven 3D printing systems employ dye molecules (*i.e.*, Sudan dyes[23]) to improve resolution and control cure rate. However, light attenuation from these dyes severely reduces cure efficiency and limits penetration depth, resulting in a thin zone of crosslinking, and necessitating the use of moving stages for part production. The layered objects produced in this manner have pronounced defects, interfacial weakness, and corresponding non-isotropic materials properties. To overcome this inherent limitation with traditional dyes, visible photochromic switches were examined as a novel strategy to control 3D-printing. Initially, the photochromic switch (**1**) absorbs light and inhibits the independent photoinitiating system, thereby "masking" the initiator and retarding cure. Photoswitching to the corresponding nonabsorbing (*e.g.*, colorless) isomer (**2**) then occurs, resulting in a bleaching front that moves through the solution, activating the photosensitizers and allowing the curing/crosslinking process to occur through the depth of the resin. From initial experiments it was observed that irradiating optically dense photochromic solutions, see **Figure 4.1a**, with collimated light leads to rapid and linear photobleaching fronts that, consistent with previous reports,[24–26] follow **Equation 1**,

$$V = \frac{\Phi I_o}{C_o} \qquad (1)$$

where V is the front velocity, Φ is the photobleaching quantum yield, and $C_o$ is the concentration of photochromic dye. This provides excellent contrast between irradiated and non-irradiated areas, yielding desirable confinement of light. Critical to the success of SMaLL is selection of a photochromic switch with an absorption profile that masks one or more photosensitizers (**Figure 4.1b**).[27–30] Diarylethenes were therefore selected as an ideal photochromic platform due to their chemical stability and widely tunable photophysical properties (absorption profile, quantum yield, *etc.*).[31–33]

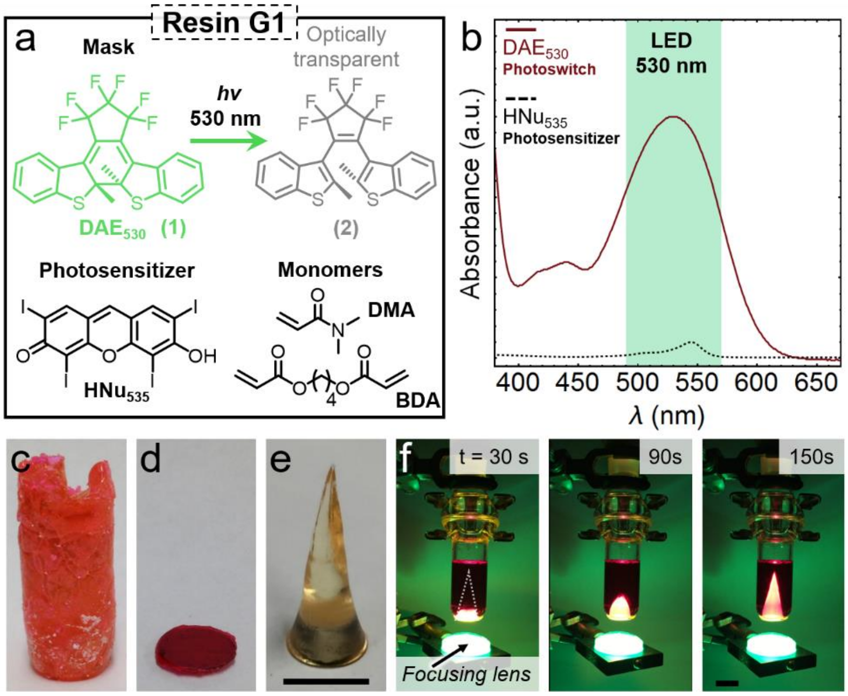

**Figure 4.1.** a) Ring-opening transformation of the photochromic switch, $DAE_{530}$, from a colored to optically transparent form upon irradiation with 530 nm light; b) Absorbance spectra of $DAE_{530}$ and $HNu_{535}$ showing overlapping profiles; c) printing in the absence of dye or photoswitch; d) printing in the presence of a non-bleaching control dye (Sudan IV) and e) Object printed with photoswitch and SMaLL; f) Timelapse photographs of the SMaLL printing process. (1 cm scale bars)

To demonstrate the performance of SMaLL, a resin (**G1**) comprised of *N*,*N*-dimethyl acrylamide (DMA) as the monomer, 1,4-butanediol diacrylate (BDA) as the cross-linker, a xanthene-derivative as the photosensitizer ($HNu_{535}$), and a diarylethene photoswitch, 1,2-bis(2-methyl-1-benzothiophen-3-yl)perfluorocyclopentene ($DAE_{530}$), as the mask was prepared and exposed to collimated green light ($\lambda_{max}$ ≈ 530 nm). As predicted by Equation 1, the front propagates through the resin with time in a linear fashion. This provides a large depth of cure (> 6 cm, see **Figure C14** and **C16**) with collimated light being necessary to maintain features over this scale (> 1 cm) due to focusing issues. This is in direct contrast to the uncontrolled polymerization observed in the absence of any dye or thin cures due to traditional, non-bleaching, dyes when exposed to 530 nm light (**Figure 4.1c-d**). Spatial confinement in the lateral dimension with SMaLL was further illustrated by exposure of resin, **G1**, to collimated green light through a focusing lens. Significantly, curing traced the focal envelope of the lens leading to the formation of a cone shaped 3D-object (**Figure 4.1e-f**). Notably, the growth of this cone, ~2.2 cm in height, requires no moving parts and occurs with a build rate of ~50 cm/hr, using a narrow band collimated green LED (450 mW/cm$^2$). To print a cone of the same dimensions *via* a state-of-the-art UV-based inkjet printing methodology requires a build time of greater than 1 hour at a build rate of ~2 cm/hr. Additionally, pairing SMaLL resins with a projector enabled the production of parts with a lateral resolution of approximately 100 microns (**Figure C17**), on par with commercial printers. This comparison clearly demonstrates the versatility of SMaLL as a rapid, low-cost continuous 3D printing process.

A key feature of SMaLL is the continuous nature of the process which has the potential to alleviate layering issues and non-isotropic properties. Initial examination of the surface morphology of 3D-objects produced by either SMaLL or traditional stereolithographic (SLA) techniques clearly shows the ability to produce featureless objects using SMaLL. Scanning electron microscopy (SEM) analysis of the object surfaces and cross-sections correlate closely with profilometry studies, highlighting the clear layering defects from SLA printing and the layerless nature of SMaLL (**Figure 4.2 and Figure C18–C22**). To further verify the isotropic nature of the structures afforded by SMaLL, a cube sample with 8 mm sides was printed and the mechanical properties of the object interrogated along multiple faces with nanoindentation.[34] For this sample, similar mechanical values ($H$ = 75 ± 5 MPa; $E$ = 1.85 ± 0.05 GPa) were obtained irrespective of the face measured (**Figure C25**), indicating uniform curing in all directions, and critically, isotropic properties.[3,35]

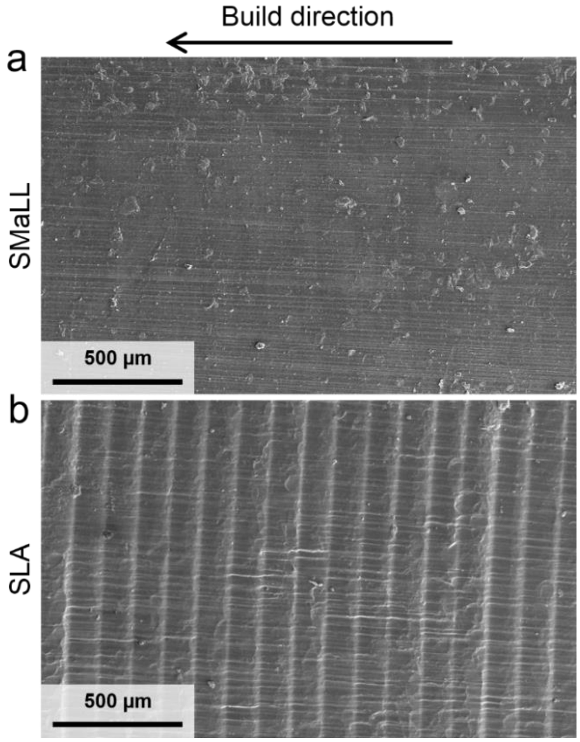

**Figure 4.2.** Scanning electron micrographs of "as printed" surfaces for cones printed by a) SMaLL and b) stereolithographic printing (SLA).

In expanding the range of materials compatible with SMaLL, different resin formulations were examined based on changing monomers, wavelength of irradiation (470 nm *vs.* 530 nm) and crosslinking chemistry (radical *vs*. cationic) (**Figure 4.3a**). Substitution of the original monomer pair (DMA and BDA) with methyl acrylate (MA) as the monomer, and tetra(ethylene glycol) diacrylate (TEGDA) as the crosslinker, while keeping the same photosensitizer ($HNu_{535}$), photoswitch ($DAE_{530}$) and light source ($\lambda_{max}$ = 530 nm) results in a significantly softer material, **G2** (500 ± 5 kPa), when compared to the original resin **G1** (1.6 ± 0.3 GPa). An even greater variation in properties is realized when the curing chemistry is changed from a radical to a cationic process. To accomplish this, camphorquinone (CQ), which is capable of inducing both radical and cationic polymerizations, was examined as the photosensitizer. As the $\lambda_{max}$ for CQ is ~470 nm, a different photoswitch, 1,2-bis(3-methyl-1-benzothiophen-2-yl)perfluorocyclopentene ($DAE_{470}$), with an absorbance profile that masks CQ was also employed. Irradiation with blue (470 nm) light now allows efficient cationic crosslinking of an epoxy-based resin, **B1,** containing (3-ethyloxetan-3-yl)methanol (OXA) and 3,4-epoxycyclohexylmethyl 3,4-epoxycyclohexanecarboxylate (ECC). Alternatively, a vinyl-based resin **B2** could also be formulated from butyl acrylate (BA) and TEGDA under the same photoswitch/photosensitizer pair, leading to radical curing. These blue-cured resins, **B1** and **B2**, were shown to have substantially different mechanical properties, with **B1** being stiff ($E \approx 3.5 \pm 0.6$ GPa) and **B2** giving soft and compliant materials ($E \approx 100 \pm 15$ kPa) (**Figure 4.3b-c**). This dual radical/cationic curing with CQ and the ~4 orders of magnitude variation in moduli clearly highlights the versatility of SMaLL as a methodology to print 3D-objects with a range of mechanical properties through wavelength selective activation of commercially viable monomer systems. Additionally, it was demonstrated that SMaLL resins can be used in conjunction with a moving stage to afford 3D objects with increasing complexity, which suggests facile integration into preexisting dynamic 3D printing technologies (e.g., SLA) (**Figure C23**).

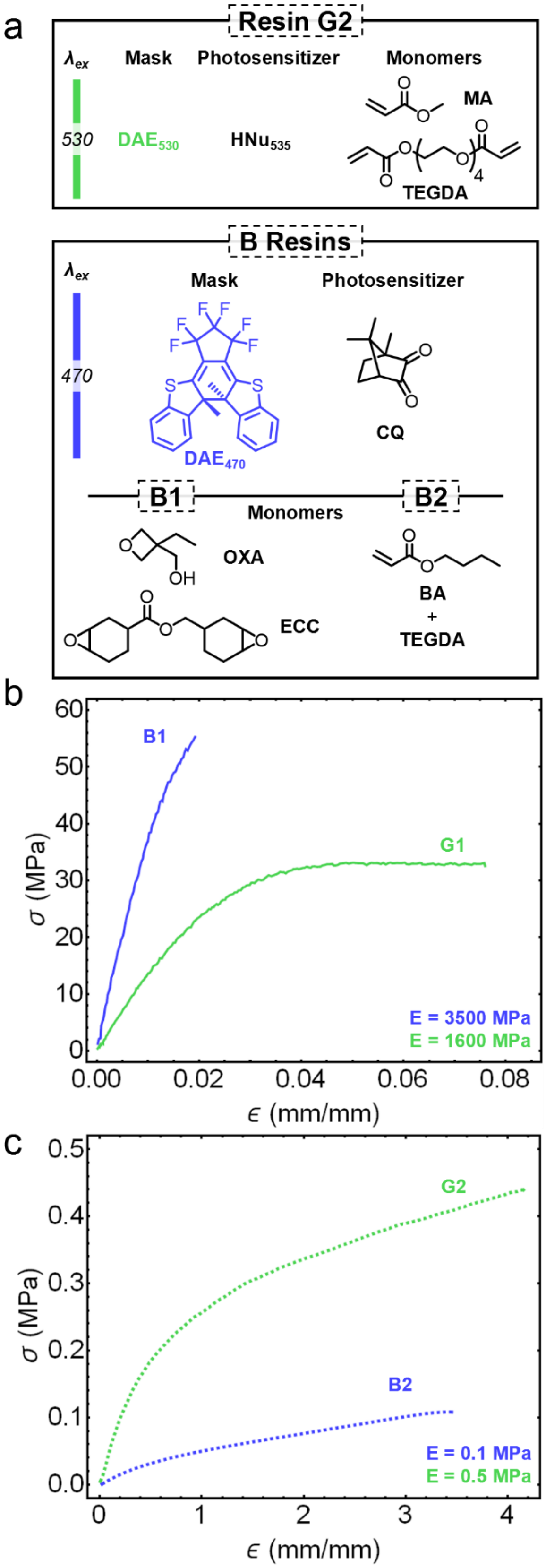

**Figure 4.3.** Various resin formulations and resultant tensile mechanical properties. a) Chemical structures for the resin components in **G2**, **B1**, and **B2;** b) Stress strain plots of stiff samples cured using green (**G1**) and blue (**B1**) light (using digital image correlation); c) Stress strain plots of flexible samples cured using green (**G2**) and blue (**B2**) light.

To generate multi-material 3D-objects with predefined and spatially resolved chemical and mechanical domains, resins **G2** and **B1** were combined in a 1 to 3 ratio (**G2**:**B1**), resulting in a resin containing multiple monomers (MA and OXA), crosslinkers (TEGDA and ECC), photosensitizers ($HNu_{535}$ and CQ), and masks ($DAE_{530}$ and $DAE_{470}$) (full resin formulation details included in Appendix C). With this formulation, wavelength-selective photocuring could be achieved. Initially, irradiation with blue light led to the formation of an interpenetrating network with undesirable microphase separation, indicated by an opaque product. To address this issue, a small amount (~2.5 wt%) of dual-functional monomer, (3-ethyloxetan-3-yl)methyl acrylate (OXA-A), was introduced to the formulation, leading to hybrid acrylate/epoxy (radical/cationic) curing and covalent coupling between the different networks, arresting phase separation.[36] In contrast to irradiation with blue light (470 nm), exposure to green light (530 nm) led to acrylate (radical- only) curing and a substantially different material, schematically shown in **Figure 4.4a**. Specifically, the blue cured material had a modulus 5 orders of magnitude greater than the same initial resin formulation cured with green light, while the green cured samples had an elongation at break that was approximately 200 times longer than the dual crosslinked systems prepared via irradiated with blue light (**Figure C30**).

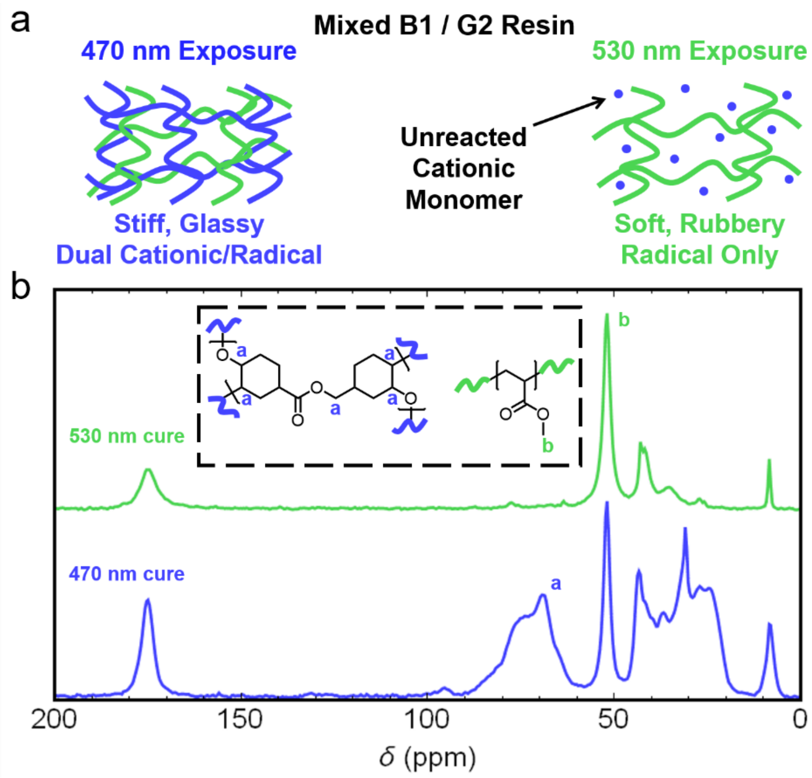

**Figure 4.4:** a) Schematic of resulting network structure when the resin combination, **B1** and **G2**, is exposed to blue or green (470 or 530 nm) light: blue exposure leads to dual radical and cationic curing, while green exposure results in only radical crosslinking; b) Solid state $^{13}$C CP-MAS NMR spectra of blue and green cured samples after washing to remove residual monomer.

To further characterize the chemical selectivity of SMaLL, solid-state $^{13}$C-NMR spectroscopy (CP-MAS) was performed on purified multi-material samples prepared from 1:1 **B1**(epoxy):**G2**(acrylate) resin mixtures. As seen in **Figure 4.4b**, no epoxy signals centered at 70 ppm were observed for the sample cured with 530 nm green light, indicating excellent orthogonality and wavelength-selectivity for cationic crosslinking, while irradiation with 470 nm blue light revealed resonances for both the epoxy and vinyl networks. This striking disparity in properties, achievable from a single photocurable resin mixture using irradiation with different wavelengths, provides an avenue toward spatially resolved objects with 3-dimensionally defined domains of tailored chemical and mechanical composition.

For multi-material design, bio-inspired systems containing hierarchical patterns of materials with dissimilar properties were then targeted for evaluating the range of sub-structures that SMaLL could print.[7,8] Two motifs found in natural systems that are challenging for 3D printing are soft joints and brick-and-mortar structures.[37,38]

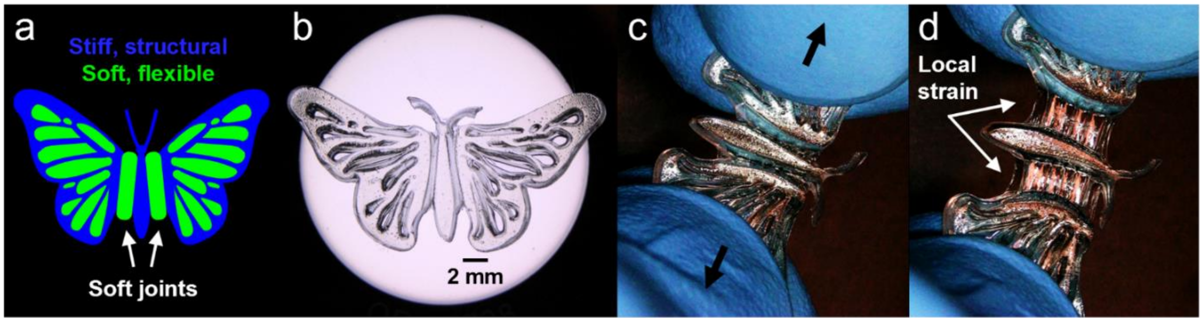

**Figure 4.5.** Demonstration of soft joints with SMaLL multi-material printing. a) Digital butterfly design with blue areas correlating to stiff sections and green areas to soft joints; b) Optical micrograph of the dried butterfly sample; c) Butterfly specimen stretched outward from the body, d) showing selective straining in the soft joints.

The potential of soft joint fabrication using SMaLL was initially demonstrated through the fabrication of a butterfly template having stiff and structural "wings" and "body" separated by soft and flexible joints (**Figure 4.5**). Significantly, this bio-inspired 3D-printed object could be fabricated in a single step from the 3:1 **B1**:**G2** resin mixture in only 10 minutes. Upon application of tension to the "wings," local strain and flexing is observed selectively in the flexible, acrylate-based joint regions while the body and wings remain rigid due to the stiff epoxy domains (white arrows **Figure 4.5d**). The bonding between material interfaces in these one-step SMaLL objects also leads to robust mechanical fatigue resistance with repeated cycling and stretching (> 100% strain) providing impressive energy dissipation and having no discernable impact on these soft joints, which highlights the benefits of linking mechanically distinct domains in 3D printing (**Figure C31**). Furthermore, under extreme strains, failure does not occur at the interface, illustrating the beneficial interwoven nature of the multi-material objects (**Figure C32**).

The versatility of SMaLL was further demonstrated via the fabrication of brick-and-mortar structures with unique mechanical properties that inhibit crack propagation and fracture. To illustrate the toughening of multi-material objects containing hard bricks in a continuous soft matrix, a design of stiff (blue) bowties embedded in a matrix of elastic (green) material was printed in a single step using the same 3:1 B1:G2 resin (**Figure 4.6**). Once dried, the printed object shows intermaterial spacing of 200 microns, which allows the individual bricks to interdigitate (**Figure C33**). Under tension, it was note-worthy to observe that the straining of the elastic matrix causes the stiff bowties to lock against one another, resulting in novel synergistic interactions when compared to objects fabricated from the individual starting materials. As a result, the bricks “lock” and the path of crack propagation is tortuous (**Figure C34**), following the mortar-bowtie interface (**Figure 4.6e**), with the toughness nearly doubling from the point of initial failure (~39 kJ/m3) to the point of ultimate failure (~77 kJ/m3). In contrast, when the stiff domains are removed the resulting structure is ~2 orders of magnitude less stiff and shows no post-failure toughening, which illustrates the synergistic multi-material properties that are now accessible using SMaLL.

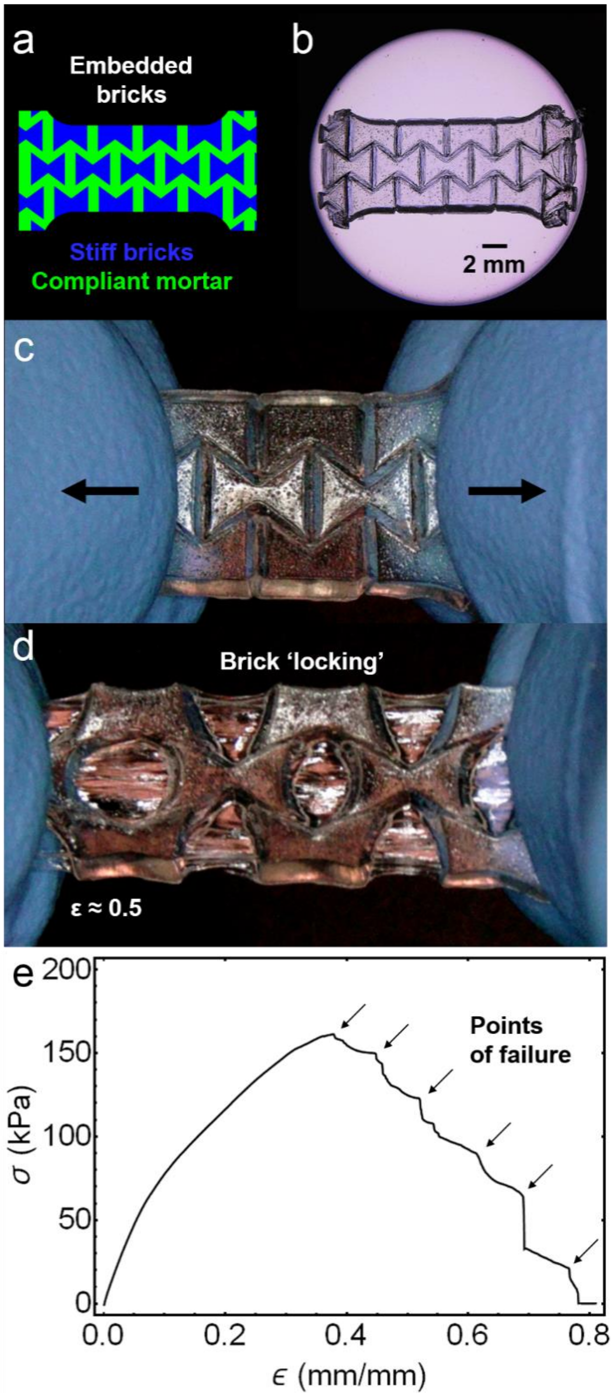

**Figure 4.6.** Multi-material printing of brick-and-mortar structures: a) Digital image with blue bowties correlating to stiff regions within a compliant green matrix; b) Optical micrograph of a dried dogbone sample; c,d) Optical micrographs of the sample before and after applied tension, showing 'locking' behavior between bowtie 'bricks'; e) Tensile measurement of the bowtie sample with toughening due to the sacrificial breaking of soft mortar between the stiff bricks (failures denoted by arrows).

## Conclusions

In summary, we have developed a novel 3D printing method, SMaLL, for the fabrication of unique structures with mechanically and chemically distinct regions. By using tunable, visible wavelength photoswitches, in combination with orthogonal crosslinking reactions, a single resin formulation can be employed for the facile, one-step printing of complex, bio-inspired structures. Performance and build rates were significantly enhanced compared to traditional techniques such as SLA. The fabrication of soft joints and brick-and-mortar architectures showcases the utility of SMaLL for printing novel all-polymer composites with well-defined regions of different mechanical and chemical properties. Ongoing research includes the in-depth characterization of multi-material interfaces produced by SMaLL and the optimization of multi-material resin curing using dynamic printing processes to access more advanced hierarchical 3D structures.

# References

(1) Bartlett, N. W.; Tolley, M. T.; Overvelde, J. T. B.; Weaver, J. C.; Mosadegh, B.; Bertoldi, K.; M.Whitesides, G.; Wood, R. J. A 3D-Printed, Functionally Graded Soft Robot Powered by Combustion. *Science.* **2015**, *349* (6244), 161–166.

(2) Ligon, S. C.; Liska, R.; Stampfl, J.; Gurr, M.; Mülhaupt, R. Polymers for 3D Printing and Customized Additive Manufacturing. *Chem. Rev.* **2017**, *117* (15), 10212–10290.

(3) Tumbleston, J. R.; Shirvanyants, D.; Ermoshkin, N.; Janusziewicz, R.; Johnson, A. R.; Kelly, D.; Chen, K.; Pinschmidt, R.; Rolland, J. P.; Ermoshkin, A.; et al. Continuous Liquid Interface Production of 3D Objects. *Science.* **2015**, *347* (6228), 1349–1352.

(4) Parra-Cabrera, C.; Achille, C.; Kuhn, S.; Ameloot, R. 3D Printing in Chemical Engineering and Catalytic Technology: Structured Catalysts, Mixers and Reactors. *Chem. Soc. Rev.* **2017**.

(5) Shusteff, M.; Browar, A. E. M.; Kelly, B. E.; Henriksson, J.; Weisgraber, T. H.; Panas, R. M.; Fang, N. X.; Spadaccini, C. M. One-Step Volumetric Additive Manufacturing of Complex Polymer Structures. *Sci. Adv.* **2017**, *3* (12), eaao5496.

(6) Poelma, J.; Rolland, J. Rethinking Digital Manufacturing with Polymers. *Science.* **2017**, *358* (6369), 1384–1386.

(7) X. Gu, G.; Su, I.; Sharma, S.; Voros, J. L.; Qin, Z.; Buehler, M. J. Three-Dimensional-Printing of Bio-Inspired Composites. *J. Biomech. Eng.* **2016**, *138* (2), 021006.

(8) Studart, A. R. Additive Manufacturing of Biologically-Inspired Materials. *Chem. Soc. Rev.* **2016**, *45* (2), 359–376.

(9) Compton, B. G.; Lewis, J. A. 3D-Printing of Lightweight Cellular Composites. *Adv. Mater.* **2014**, *26* (34), 5930–5935.

(10) Kolesky, D. B.; Truby, R. L.; Gladman, A. S.; Busbee, T. A.; Homan, K. A.; Lewis, J. A. 3D Bioprinting of Vascularized, Heterogeneous Cell-Laden Tissue Constructs. *Adv. Mater.* **2014**, *26* (19), 3124–3130.

(11) Yang, H.; Leow, W. R.; Wang, T.; Wang, J.; Yu, J.; He, K.; Qi, D.; Wan, C.; Chen, X. 3D Printed Photoresponsive Devices Based on Shape Memory Composites. *Adv. Mater.* **2017**, *1701627*, 1–7.

(12) Wang, L.; Lau, J.; Thomas, E. L.; Boyce, M. C. Co-Continuous Composite Materials for Stiffness, Strength, and Energy Dissipation. *Adv. Mater.* **2011**, *23* (13), 1524–1529.

(13) Ober, T. J.; Foresti, D.; Lewis, J. A. Active Mixing of Complex Fluids at the Microscale. *Proc. Natl. Acad. Sci.* **2015**, *112* (40), 12293–12298.

(14) Collino, R. R.; Ray, T. R.; Fleming, R. C.; Cornell, J. D.; Compton, B. G.; Begley, M. R. Deposition of Ordered Two-Phase Materials Using Microfluidic Print Nozzles with Acoustic Focusing. *Extrem. Mech. Lett.* **2016**, *8*, 96–106.

(15) Hardin, J. O.; Ober, T. J.; Valentine, A. D.; Lewis, J. A. Microfluidic Printheads for Multimaterial 3D Printing of Viscoelastic Inks. *Adv. Mater.* **2015**, *27* (21), 3279–3284.

(16) Ge, Q.; Sakhaei, A. H.; Lee, H.; Dunn, C. K.; Fang, N. X.; Dunn, M. L. Multimaterial 4D Printing with Tailorable Shape Memory Polymers. *Sci. Rep.*

**2016**, *6* (1), 31110.

(17) Peterson, G. I.; Larsen, M. B.; Ganter, M. A.; Storti, D. W.; Boydston, A. J. 3D-Printed Mechanochromic Materials. *ACS Appl. Mater. Interfaces* **2015**, *7* (1), 577–583.

(18) Hong, S.; Sycks, D.; Chan, H. F. ai; Lin, S.; Lopez, G. P.; Guilak, F.; Leong, K. W.; Zhao, X. 3D Printing of Highly Stretchable and Tough Hydrogels into Complex, Cellularized Structures. *Adv. Mater.* **2015**, *27* (27), 4034.

(19) Peterson, G. I.; Schwartz, J. J.; Zhang, D.; Weiss, B. M.; Ganter, M. A.; Storti, D. W.; Boydston, A. J. Production of Materials with Spatially-Controlled Cross-Link Density via Vat Photopolymerization. *ACS Appl. Mater. Interfaces* **2016**, *8* (42), 29037–29043.

(20) Martínez, J.; Dumas, J.; Lefebvre, S. Procedural Voronoi Foams for Additive Manufacturing. *ACM Trans. Graph.* **2016**, *35* (4), 12.

(21) Sydney Gladman, A.; Matsumoto, E. A.; Nuzzo, R. G.; Mahadevan, L.; Lewis, J. A. Biomimetic 4D Printing. *Nat. Mater.* **2016**, *15* (4), 413–418.

(22) Fu, C.; Xu, J.; Boyer, C. Photoacid-Mediated Ring Opening Polymerization Driven by Visible Light. *Chem. Commun.* **2016**, *52* (44), 7126–7129.

(23) Rogers, C. I.; Qaderi, K.; Woolley, A. T.; Nordin, G. P. 3D Printed Microfluidic Devices with Integrated Valves. *Biomicrofluidics* **2015**, *9* (1).

(24) Terrones, G.; Pearlstein, A. J. Effects of Optical Attenuation and Consumption of a Photobleaching Initiator on Local Initiation Rates in Photopolymerizations. *Macromolecules* **2001**, *34* (10), 3195–3204.

(25) Miller, G. A.; Gou, L.; Narayanan, V.; Scranton, A. B. Modeling of

Photobleaching for the Photoinitiation of Thick Polymerization Systems. *J. Polym. Sci. Part A Polym. Chem.* **2002**, *40* (6), 793–808.

(26) Dolinski, N. D.; Page, Z. A.; Eisenreich, F.; Niu, J.; Hecht, S.; Read de Alaniz, J.; Hawker, C. J. A Versatile Approach for In Situ Monitoring of Photoswitches and Photopolymerizations. *ChemPhotoChem* **2017**, *1* (4), 125–131.

(27) Corrigan, N.; Shanmugam, S.; Xu, J.; Boyer, C. Photocatalysis in Organic and Polymer Synthesis. *Chem. Soc. Rev.* **2016**, *45* (22), 6165–6212.

(28) Kottisch, V.; Michaudel, Q.; Fors, B. P. Photocontrolled Interconversion of Cationic and Radical Polymerizations. *J. Am. Chem. Soc.* **2017**, *139* (31), 10665–10668.

(29) Xiao, P.; Zhang, J.; Dumur, F.; Tehfe, M. A.; Morlet-Savary, F.; Graff, B.; Gigmes, D.; Fouassier, J. P.; Lalevée, J. Visible Light Sensitive Photoinitiating Systems: Recent Progress in Cationic and Radical Photopolymerization Reactions under Soft Conditions. *Prog. Polym. Sci.* **2015**, *41* (C), 32–66.

(30) Zhang, X.; Xi, W.; Huang, S.; Long, K.; Bowman, C. N. Wavelength-Selective Sequential Polymer Network Formation Controlled with a Two-Color Responsive Initiation System. *Macromolecules* **2017**, *50* (15), 5652–5660.

(31) Irie, M.; Fukaminato, T.; Matsuda, K.; Kobatake, S. Photochromism of Diarylethene Molecules and Crystals: Memories, Switches, and Actuators. *Chem. Rev.* **2014**, *114* (24), 12174–12277.

(32) Herder, M.; Schmidt, B. M.; Grubert, L.; Pätzel, M.; Schwarz, J.; Hecht, S. Improving the Fatigue Resistance of Diarylethene Switches. *J. Am. Chem. Soc.* **2015**, *137* (7), 2738–2747.

(33) Herder, M.; Eisenreich, F.; Bonasera, A.; Grafl, A.; Grubert, L.; Pätzel, M.; Schwarz, J.; Hecht, S. Light-Controlled Reversible Modulation of Frontier Molecular Orbital Energy Levels in Trifluoromethylated Diarylethenes. *Chem. - A Eur. J.* **2017**, *23* (15), 3743–3754.

(34) Briscoe, B. J.; Fiori, L.; Pelillo, E. Nano-Indentation of Polymeric Surfaces. *J. Phys. D. Appl. Phys.* **1998**, *31* (19), 2395–2405.

(35) Rinaldi, R. G.; Bernal-Ostos, J.; Hammetter, C. I.; Jacobsen, A. J.; Zok, F. W. Effects of Material Heterogeneities on the Compressive Response of Thiol-Ene Pyramidal Lattices. *J. Mater. Sci.* **2012**, *47* (18), 6621–6632.

(36) Masci, G.; Giacomelli, L.; Crescenzi, V. Atom Transfer Radical Polymerization Of. *Macromolecules* **2004**, *32* (15), 559–564.

(37) Tadayon, M.; Amini, S.; Masic, A.; Miserez, A. The Mantis Shrimp Saddle: A Biological Spring Combining Stiffness and Flexibility. *Adv. Funct. Mater.* **2015**, *25* (41), 6437–6447.

(38) Yaraghi, N. A.; Guarín-Zapata, N.; Grunenfelder, L. K.; Hintsala, E.; Bhowmick, S.; Hiller, J. M.; Betts, M.; Principe, E. L.; Jung, J. Y.; Sheppard, L.; et al. Biocomposites: A Sinusoidally Architected Helicoidal Biocomposite (Adv. Mater. 32/2016). *Adv. Mater.* **2016**, *28* (32), 6769.

## Chapter 5: Conclusion

In summary, light-mediated chemical transformations have a wide range of applications in soft materials, and through understanding the underlying mechanics of these chemistries, new processes and synthetic systems can be developed. The fiber-coupled NMR technique described in Chapter 2 demonstrated a long-lived photobleaching front phenomenon for optically dense solutions of photochromic molecules. While these fronts have great potential for the direct measurement of quantum yield for challenging T-type negative photochromes, they also showed great promise for controlling photochemistry through the depth of a reaction. The *in situ* fiber-coupled technique was then applied to a variety of state-of-the-art photo-meidated controlled radical polymerizations to assess their temporal control in Chapter 3. Of the catalytic systems studied, it was demonstrated that the current generation of Cu-mediated ATRP photopolymerizations demonstrated nonideal growth during dark periods. By isolating these catalytic systems, the underlying mechanism of the dark growth could be investigated, identifying residual Cu(I) activator species as the likely cause of the undesirable growth. While this result is intriguing, this Chapter was the first to compare vastly different polymerization approaches operating through a wide range of wavelengths under unified reaction conditions (fixed photon flux, monomer concentration, etc). The concepts learned in the preceding Chapters, photobleaching fronts and the use of different wavelengths to induce dissimilar polymerization mechanisms, were then combined to develop a novel approach to multimaterial 3D printing. By pairing photochromic molecules with light-sensitive initiating systems with similar absorbances, different wavelengths of light could be used to continuously cure parts with color-specified mechanical properties using a simple office-style projector. This technique (Solution Mask Liquid Lithography) was then used to produce high resolution parts with a variety of useful bio-inspired motifs. Moving forward, these techniques have great promise in a variety of applications across the broad field of photochemistry.

The rapid development of negative photochromic systems, particularly Donor Acceptor Stenhouse Adducts (DASA) at UCSB, requires effective procedures for the determination of quantum yield. While the fiber-coupled technique was used to obtain the quantum yield of a single Gen2 DASA species, without comparison across several species this information does little to enhance our understanding of the impacts of electronics on switching efficiency. Similarly, although fiber-coupled NMR was used to identify the potential cause of dark growth in Cu-mediated ATRP, further experimentation is necessary to address the underlying mechanism. While reducing the Cu loading is an obvious route to reducing dark growth, this approach will likely significantly reduce the rate of polymerization. An ideal approach will likely include an additional reactant that can selectively react with residual Cu species in dark periods to retain fast kinetics while acting to eliminate dark growth.

The use of simple colored light to define mechanical properties in DLP printing represents a large advance in multimaterial printing, with a vast range of opportunities. As currently formulated, SMaLL resins are able to define regions of radically-cured and radically/cationically cured materials. While an innumerable variety of resins with interesting properties could be formulated using this approach, further development of orthogonal chemistries will lead to increased flexibility for future additive manufacturing approaches. Additionally, the incorporation of a range of filler particles, from expandable microspheres to conducting particles, would add an extra dimension of materials properties to wavelength specific resins. However, to best take advantage of wavelength selective resins, they must be used in conjunction with dynamic printing setups such as more traditional DLP systems and potentially a continuous CLIP-like approach. To accomplish this, significant effort will have to be placed in finding robust, photostable dyes to mask the photosensitizing systems without interfering with the curing chemistry.

In closing, this thesis demonstrates that thorough investigation of underlying photochemical mechanisms can lead directly to the development of new techniques and processes for polymeric materials engineering.

# Appendix A: Supporting Information for Chapter 2

The content of Appendix A was originally published in *ChemPhotoChem*. Reproduced with permission from *ChemPhotoChem* **2017**, 1, 4, 125–131.

## Materials

All materials were purchased from Sigma Aldrich and used as received unless otherwise stated. All solvents were purchased from Fisher Scientific and used as received. Methyl acrylate was passed through a column of basic alumina (~150 mesh, Brockmann I grade) prior to use in order to remove the inhibitor. Tetrahydroquinoline barbituric acid DASA (**1**) was synthesized according to a literature procedure.[1] The Teflon insert was machined in house (for engineering drawing see Fig S1). The optical fiber (FT1000UMT; End A flat cleave; End B- SMA adapter; Furcation Tubing-FT038), and the five fiber-coupled LEDs, warm white (MWWHF2), 405 nm (M405FP1), 470 nm (M470F3), 530 nm (M530F2), and 617 nm (M617F2), were purchased from Thorlabs. A 1 mm hole was drilled into a standard polyethylene NMR tube cap using a lathe to guide the fiber.

### Instrumentation

All nuclear magnetic resonance spectra were recorded on a Varian 600 MHz spectrometer with a regulated temperature of 25 °C. Size exclusion chromatography (SEC) for molecular weight analysis, relative to linear polystyrene standards, was performed on a Waters 2690 separation module equipped with Waters 2414 refractive index and 2996 photodiode array detectors using $CHCl_3$ containing 0.25% triethylamine as eluent at a flow rate of 1 mL/min. For photochemical transformations in the NMR the LED was coupled into a multimode optical fiber terminated with a flat cleave and the intensity and 'on'/'off' cycles were controlled through a digital-to-analog converter (National Instruments USB-6009) using LabVIEW, which was connected to a T-cube LED driver (LEDD1B) from Thorlabs. A spectrophotometer with cosine corrector and radiometric calibration (Ocean Optics, model USB 4000) was used to measure LED emission profiles and calculate the power density of emission coming out of the fiber tip.

Video analysis was carried out by filming a propagating front with a suitable scale bar and measuring the front position as a function of time to determine velocity. A sample video is included with the supplemental materials.

## Synthesis

The synthesis of *1,2-bis(2-methylbenzo[b]thiophen-3-yl)hexafluorocyclopentene* (**S1**) was accomplished according to previously reported protocols.[2,3]

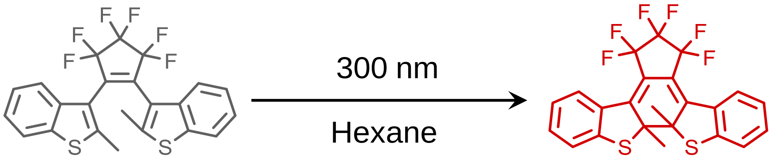

**S1** **S2**

A solution of **S1** (2.272 g, 4.85 mmol) in 2.0 L of hexane was added to a 2.5 L quartz container and placed in a Rayonet Photochemical Reactor equipped with 11x 300 nm lamps. The solution was irradiated for 25 min while stirring vigorously. After evaporation of the solvent the residue was purified by column chromatography (hexane) affording **S2** as a dark red solid (0.591 g, 1.26 mmol, 26%).

### Sample preparation for *in situ* NMR analysis

Photoswitches:

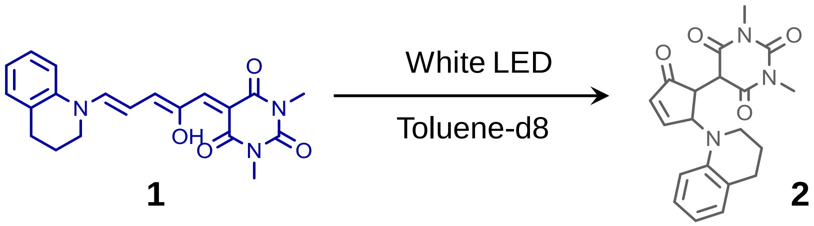

**1** **2**

A 10 mM solution of **1** (open DASA) in toluene-d8 was prepared in the dark and added to a 5 mm NMR tube such that the solution was ~2 mm above the measurement region. The optical fiber and Teflon insert were placed into the NMR tube such that the fiber was ~2 mm above the solution. All NMR measurements were performed as an array and the intensity of the white LED was controlled by a LabVIEW program connected to a T-cube LED driver. The $^1$H-NMR measurements were taken every 30 seconds, monitoring methyl protons corresponding to the two valence tautomers **1** and **2** to determine front propagation (Figure A4).

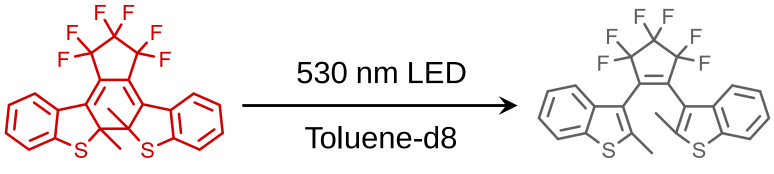

**S2** **S1**

A 30 mM solution of **S2** (closed DAE) in toluene-d8 was prepared in the dark and added to a 5 mm NMR tube such that the solution was ~2 mm above the measurement region. The optical fiber and Teflon insert were placed into the NMR tube such that the fiber was ~2 mm above the solution. All NMR measurements were performed as an array and the intensity of the green (530 nm) LED was controlled by a LabVIEW program connected to a T-cube LED driver. The $^1$H-NMR measurements were taken every 30 seconds, monitoring methyl protons corresponding to the two valence tautomers **S1** and **S2** to determine front propagation (Figure A5).

Photopolymerizations:

(i) Polymerization of methyl acrylate (MA) by PET-RAFT

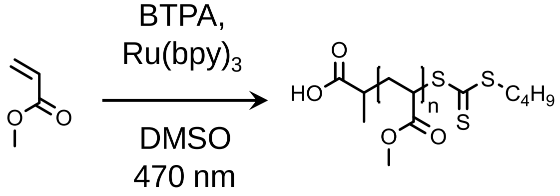

Methyl acrylate (1 mL, 11.2 mmol), DMSO-d6 (3.38 mL), 2-(((butylthio)carbonothioyl)thio)propanoic acid (13.3 mg, 56 µmol) and Ru(bpy)$_3$ (84 µL of a 1 mg/mL solution in DMSO-d6, 0.11 µmol, 87 ppm relative to monomer) were mixed to generate a stock solution that was used for all NMR experiments (2.5 M MA, target DP = 200). A fraction of the mixture was added to a 5 mm NMR tube so that the solution was ~2 mm above the measurement region. The optical fiber and Teflon insert were placed into the NMR tube such that the fiber was ~2 mm above the solution. All NMR measurements were performed as an array and a LabVIEW program connected to a T-cube LED driver was used to automate both intensity and ‘on’/’off’ times of a 470 nm LED.

Bench scale polymerizations of (i):

(a) Small scale benchtop reaction: Methyl acrylate (0.1 g, 1.16 mmol), DMSO (0.35 mL), 2- (((butylthio)carbonothioyl)thio)propanoic acid (1.4 mg, 5.8 µmol), and Ru(bpy)3Cl2 (8.7 µL of a 1 mg/mL solution in DMSO, 0.012 µmol, 87 ppm relative to monomer) were mixed in a 2 mL glass vial equipped with a magnetic stir bar and threaded septum cap (2.5 M MA, target DP = 200). An optical fiber (1 mm diameter) was inserted through the septum and placed above the solution. The mixture was degassed with argon for 5 minutes, the vial was wrapped in aluminum foil, and the solution was illuminated using a 470 nm LED (140 mW/cm2 ) coupled to the optical fiber. Aliquots were removed via syringe at 5, 10, and 15 minutes and the conversion was checked with 1H NMR, providing 27, 49, and 71 % conversion, respectively. (b) Medium scale benchtop reaction: Methyl acrylate (0.6 g, 6.97 mmol), DMSO (2.11 mL), 2- (((butylthio)carbonothioyl)thio)propanoic acid (8.3 mg, 34.8 µmol), and Ru(bpy)3Cl2 (52.2 µL of a 1 mg/mL solution in DMSO, 0.070 µmol, 87 ppm relative to monomer) were mixed in a 4 mL glass vial equipped with a magnetic stir bar and threaded septum cap (2.5 M MA, target DP = 200). An optical fiber (1 mm diameter) was inserted through the septum and placed above the solution. The mixture was degassed with argon for 5 minutes, the vial was wrapped in aluminum foil, and the solution was illuminated using a 470 nm LED (140 mW/cm2 ) coupled to the optical fiber. Aliquots were removed via syringe at 15, 30, 45, and 60 minutes and the conversion was checked with 1H NMR, providing 26, 59, 79, and 90 % conversion, respectively. (c) Large scale benchtop reaction: Methyl acrylate (3.0 g, 34.8 mmol), DMSO (10.54 mL), 2-(((butylthio)carbonothioyl)thio)propanoic acid (41.5 mg, 174 µmol), and Ru(bpy)3Cl2

(260.9 µL of a 1 mg/mL solution in DMSO, 0.348 µmol, 87 ppm relative to monomer) were mixed in a 20 mL glass vial equipped with a magnetic stir bar and threaded septum cap (2.5 M MA, target DP = 200). An optical fiber (1 mm diameter) was inserted through the septum and placed above the solution. The mixture was degassed with argon for 5 minutes, the vial was wrapped in aluminum foil, and the solution was illuminated using a 470 nm LED (140 mW/cm2 ) coupled to the optical fiber. Aliquots were removed via syringe at 30, 60, 90, and 120 minutes and the conversion was checked with 1H NMR, providing 16, 49, 65, and 79 % conversion, respectively.

(ii) Polymerization of dimethylacrylamide (DMA) by PET-RAFT

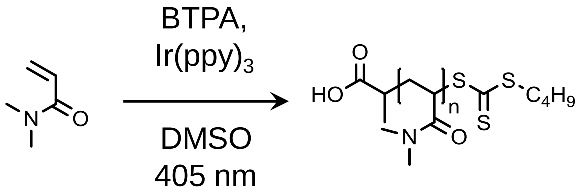

*N*,*N*-Dimethylacrylamide (0.77 mL, 7.5 mmol), DMSO-d6 (2.13 mL), 2-(((butylthio)carbonothioyl)thio)propanoic acid (8.9 mg, 37.5 µmol), and Ir(ppy)$_3$ (98 µL of a 0.5 mg/mL solution in DMSO-d6, 0.075 µmol, 66 ppm relative to monomer) were mixed to generate a stock solution that was used for all NMR experiments (2.5 M MMA, target DP = 200). A fraction of the mixture was added to a 5 mm NMR tube so that the solution was ~2 mm above the measurement region. The optical fiber and Teflon insert were placed into the NMR tube such that the fiber was ~2 mm above the solution. All NMR measurements were performed as an array and a

LabVIEW program connected to a T-cube LED driver was used to automate both intensity and ‘on’/’off’ times of a 405 nm LED.

(iii) Polymerization of methylmethacrylate (MMA) by photo-ATRP

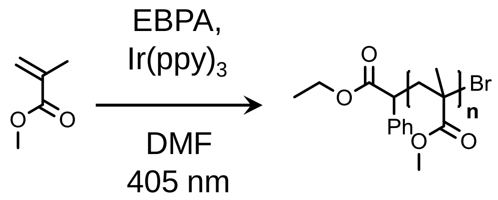

Methyl methacrylate (0.53 mL, 5.0 mmol), DMF-d7 (1.43 mL), methyl α-bromophenylacetate (3.9 µL, 25 µmol), and Ir(ppy)3 (33 µL of a 1 mg/mL solution in DMF-d7, 0.05 µmol, 66 ppm relative to monomer) were mixed to generate a stock solution that was used for all NMR experiments (2.5 M MMA, target DP = 200). A fraction of the mixture was added to a 5 mm NMR tube so that the solution was ~2 mm above the measurement region. The optical fiber and Teflon insert were placed into the NMR tube such that the fiber was ~2 mm above the solution. All NMR measurements were performed as an array and a LabVIEW program connected to a T-cube LED driver was used to automate both intensity and ‘on’/’off’ times of a 405 nm LED.

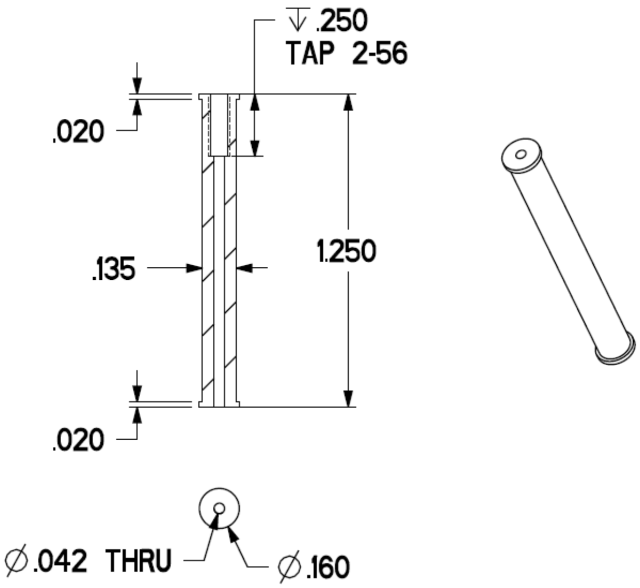

Figure A1: Engineering schematic of insert used to center fiber in NMR tube. Teflon was used as the insert material for this work. The tap shown is recommended for insert retrieval from the tube. Dimensions provided are in inches.

# CHARACTERIZATION

## Photoswitch front propagation

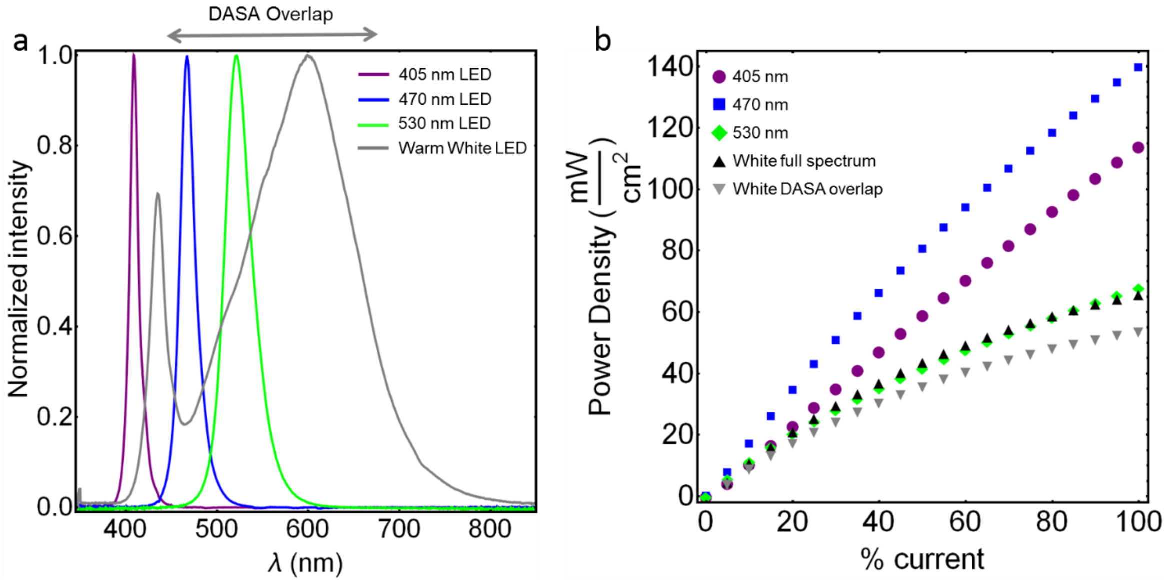

Figure A2: a) Intensity profiles of exchangeable fiber-coupled LEDs. This data was collected using an Ocean Optics USB 4000. The resulting spectra had units of W/cm$^2$/nm, allowing for power density determination via integration of the spectra. DASA overlap (460-660 nm) was used to determine effective power for Fig 3. b) Power densities measured from the tip of the optical fiber connected to the various LEDs as a function of percent current.

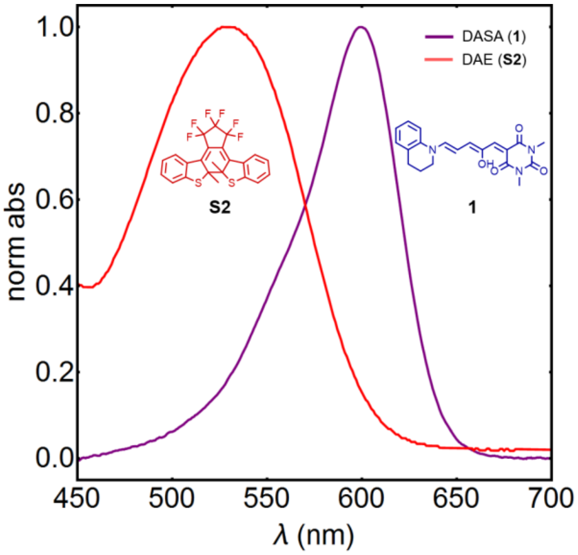

Figure A3: Absorption profiles for DAE and DASA photoswitches measured in toluene.

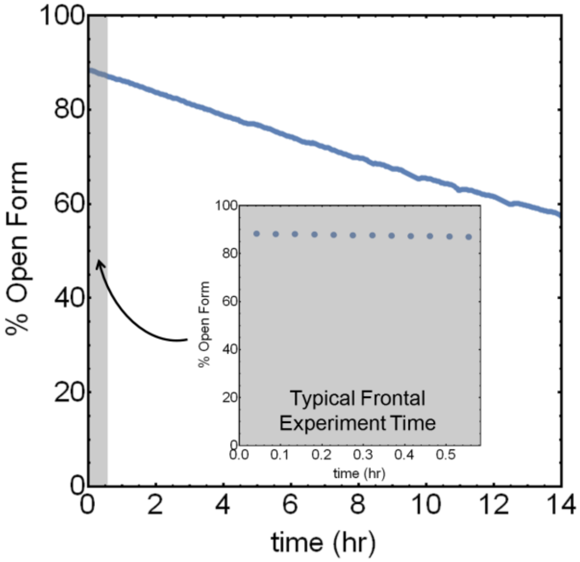

Figure A4: Thermal equilibration of closed form DASA in toluene at 45C. Even at an elevated temperature (frontal experiments held at 25C) thermal relaxation is a negligible process in the typical frontal experiment time of ~30 minutes. Data was collected via *in situ* NMR at a constant temperature of 45C, the sample was equilibrated for ten minutes at 45C before data acquisition. Data points determined by the ratio of open/closed methyl peaks as shown in Figure A6.

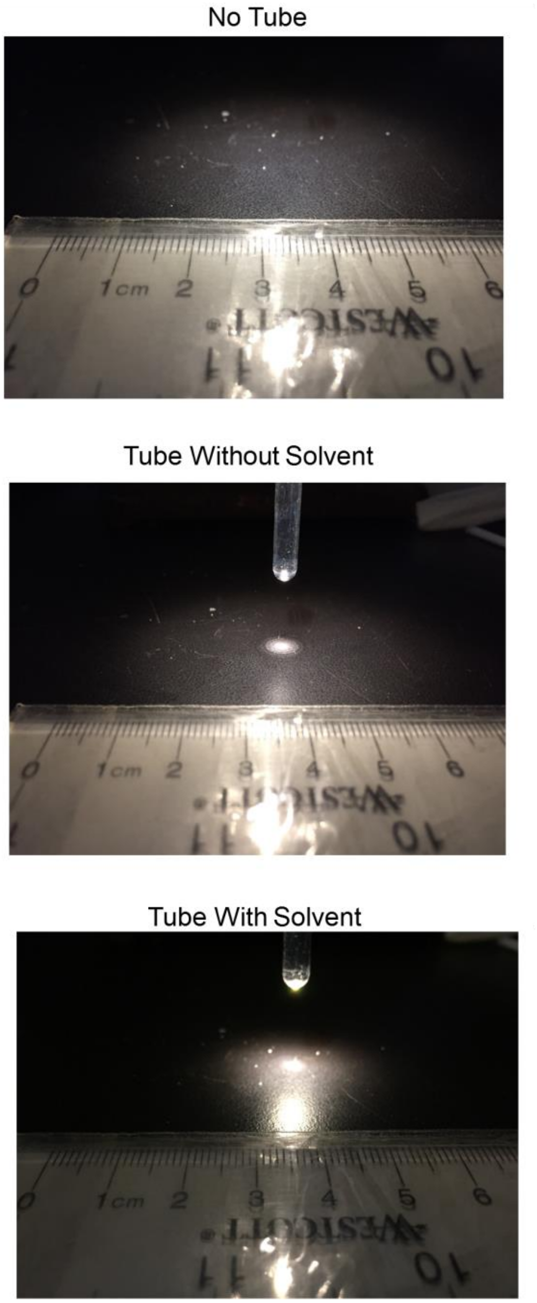

Figure A5: Example of waveguiding provided by the combination of the NMR tube containing solvent, this is a similar phenomenon to the internal reflection occurring within the fiber optic cable. This behavior enables the generation of a coherent front with linear propagation.

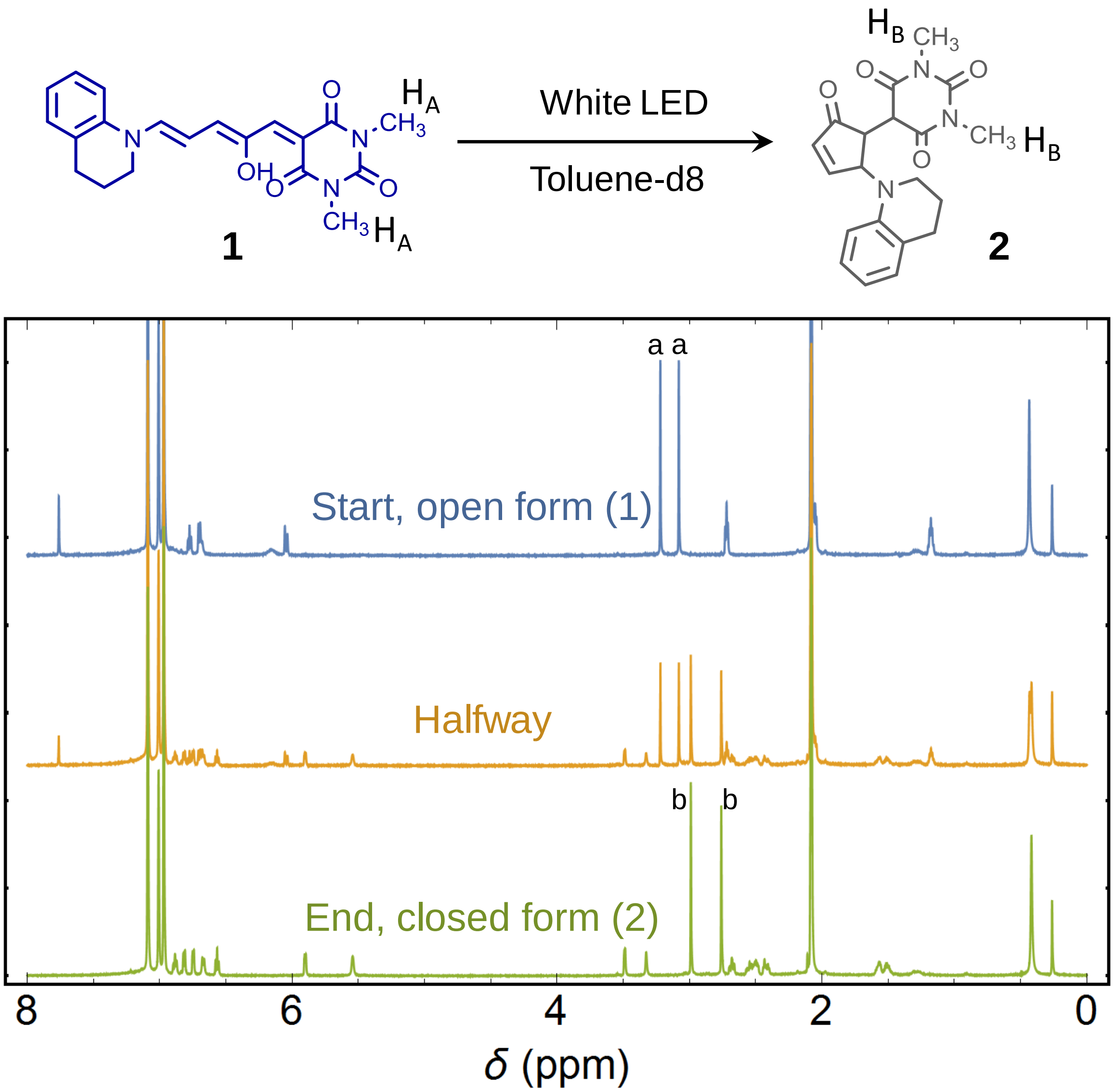

$$\% \, Open = 100 * \frac{\int Peaks \; a}{\int Peaks \; b + \int Peaks \; a}$$

Figure A6: Stack of $^{1}$H-NMR spectra showing various stages of switching from the open to the closed form of THQ DASA. Peaks labeled a and b, respectively, were used for calculations according to the formula shown on the bottom.

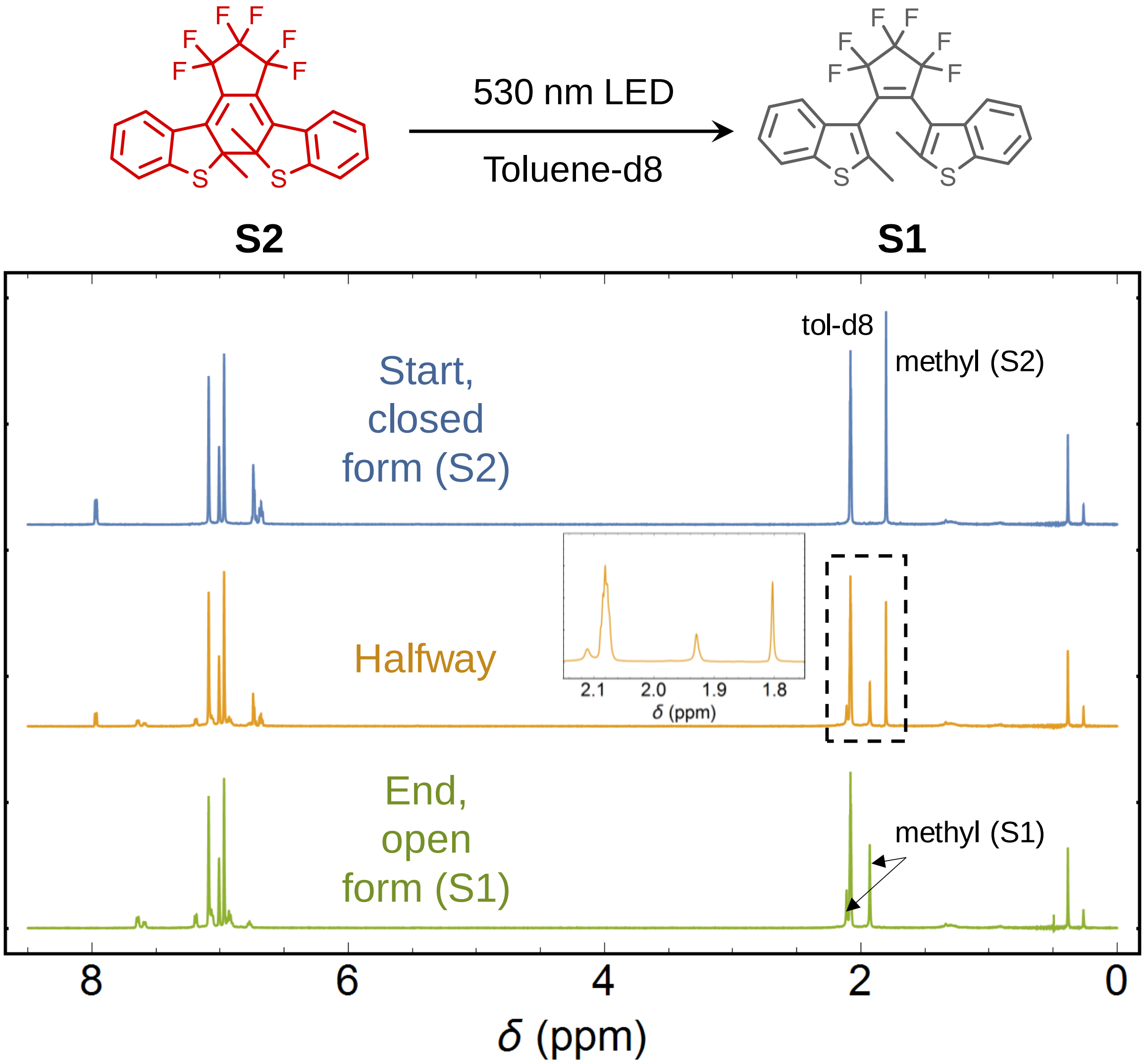

$$\%\,Closed = 100 * \frac{\int Methyl\;S2\;peaks}{\int Methyl\;S1\;peaks + \int Methyl\;S2\;peaks}$$

Figure A7: Stack of $^1$H-NMR spectra showing various stages of switching from the closed to the open form of DAE. Inset shown for the region of the methyl protons. Note that the open isomer at room temperate exists as a mixture of two non-interconverting conformers, i.e. antiparallel and parallel, each with one distinct methyl proton signal. Peaks labeled S1 and S2, respectively, were used for calculations according to the formula shown on the bottom.

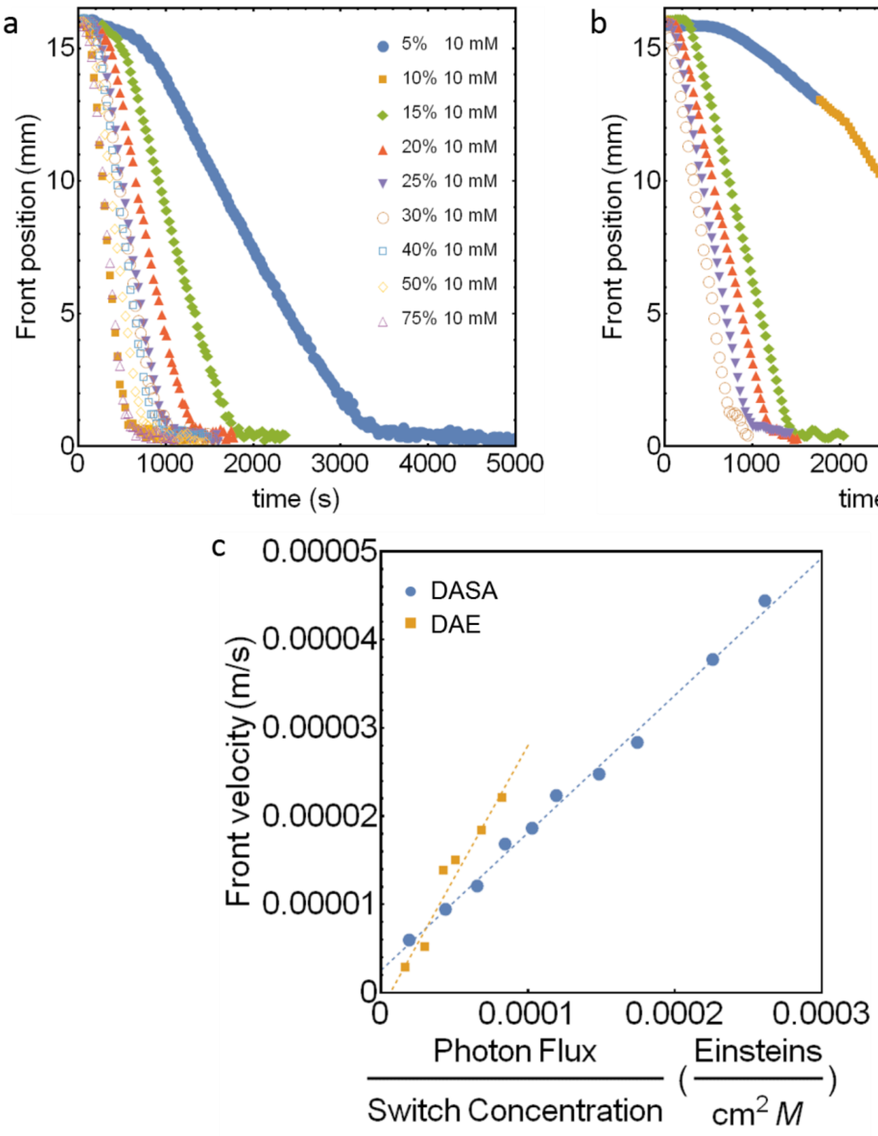

Figure A8: a) NMR data (as shown in Fig 3a) converted to distance for DASA samples, this is done by normalizing the first data point to 1 and multiplying by the size of the measurement window (in this case 16 mm). b) Front position data for DAE samples. c) Front velocity vs incident light for determination of quantum yield, where light intensity is converted to photon flux for the calculation. Photon energy given by $E = \frac{hc}{\lambda}$ where h is Planck's constant, c is the speed of light, and λ is the wavelength.

**Controlled photopolymerizations**

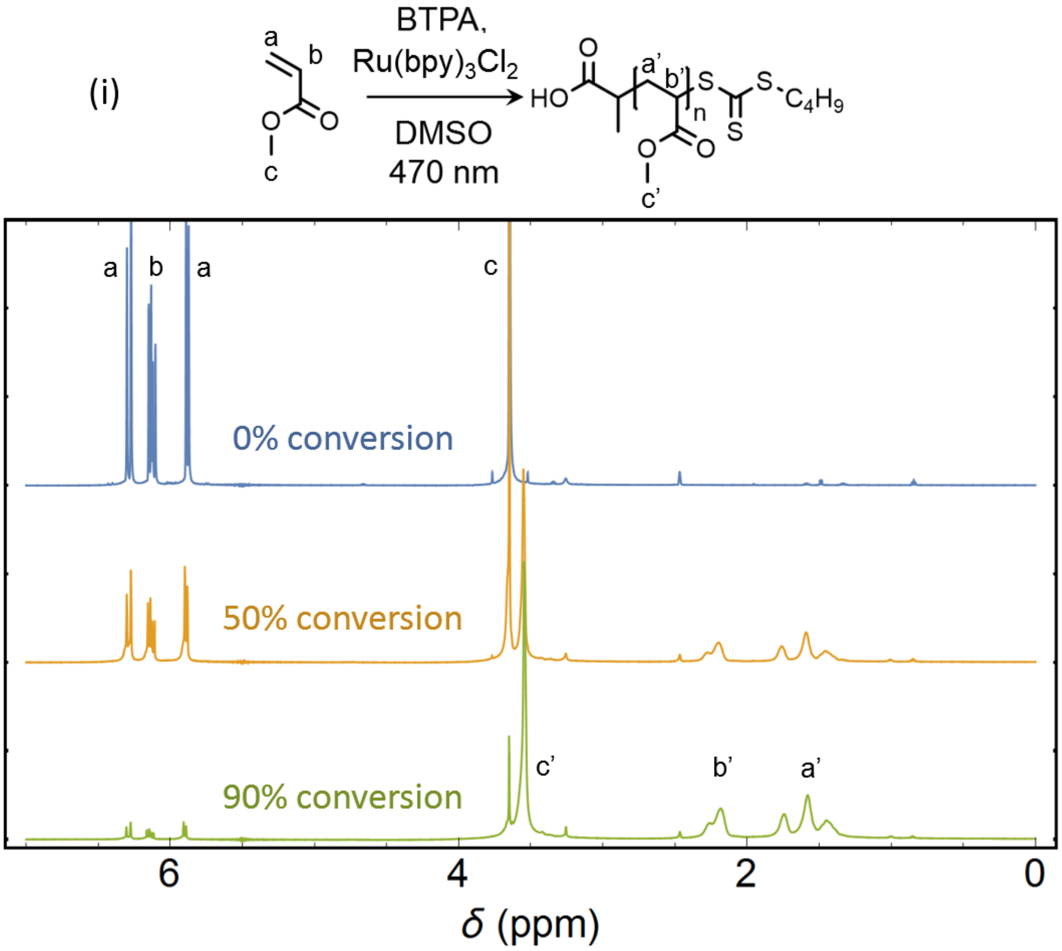

$$Conversion = \frac{\int Peaks\ a', b'}{\int Peaks\ a, b + \int Peaks\ a', b'}$$

Figure A9: Stack of $^1$H-NMR spectra of PET-RAFT of MA at various stages of conversion. Peaks labeled a,b and a',b', respectively, were used for calculations according to the formula shown on the bottom.

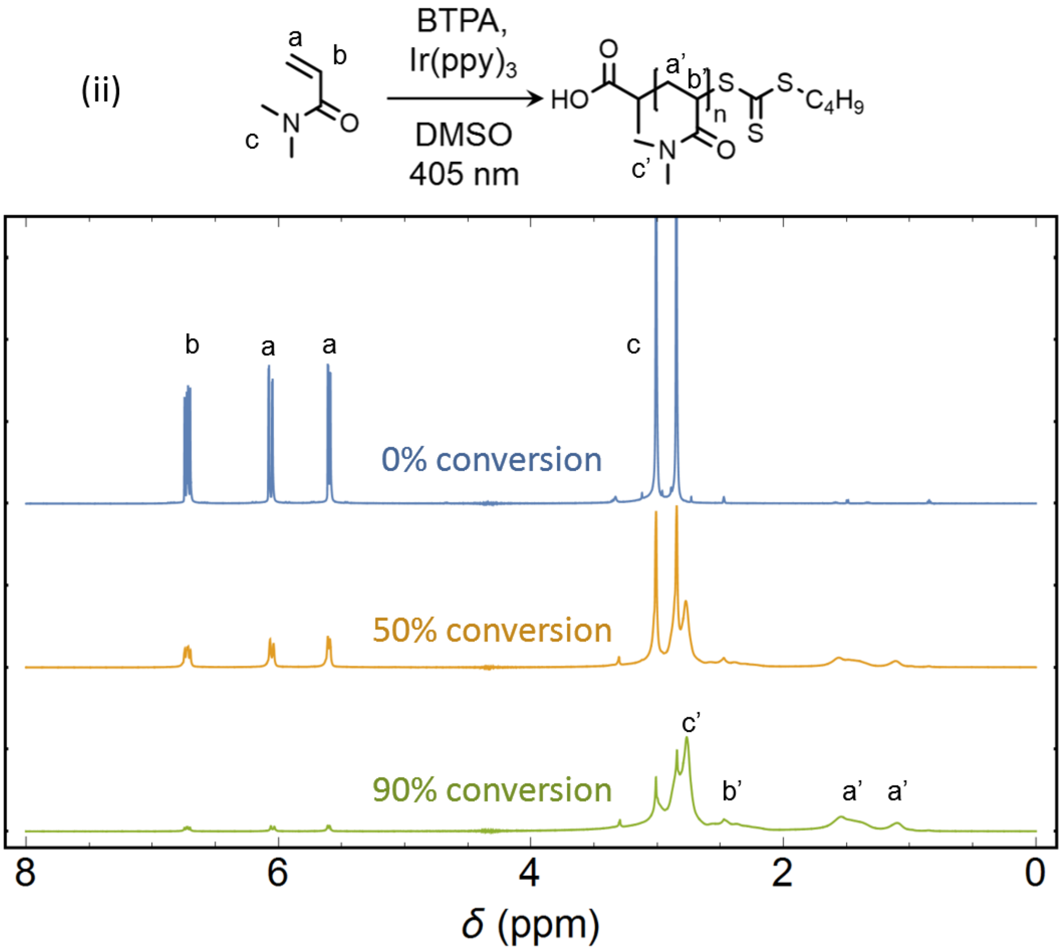

$$Conversion = \frac{\frac{3}{2}\int Peaks\ a'}{\int Peaks\ a,b + \frac{3}{2}\int Peaks\ a'}$$

Figure A10: Stack of $^1$H-NMR spectra of PET-RAFT of DMA at various stages of conversion. Peaks labeled a,b and a’,b’, respectively, were used for calculations according to the formula shown on the bottom.

(iii)

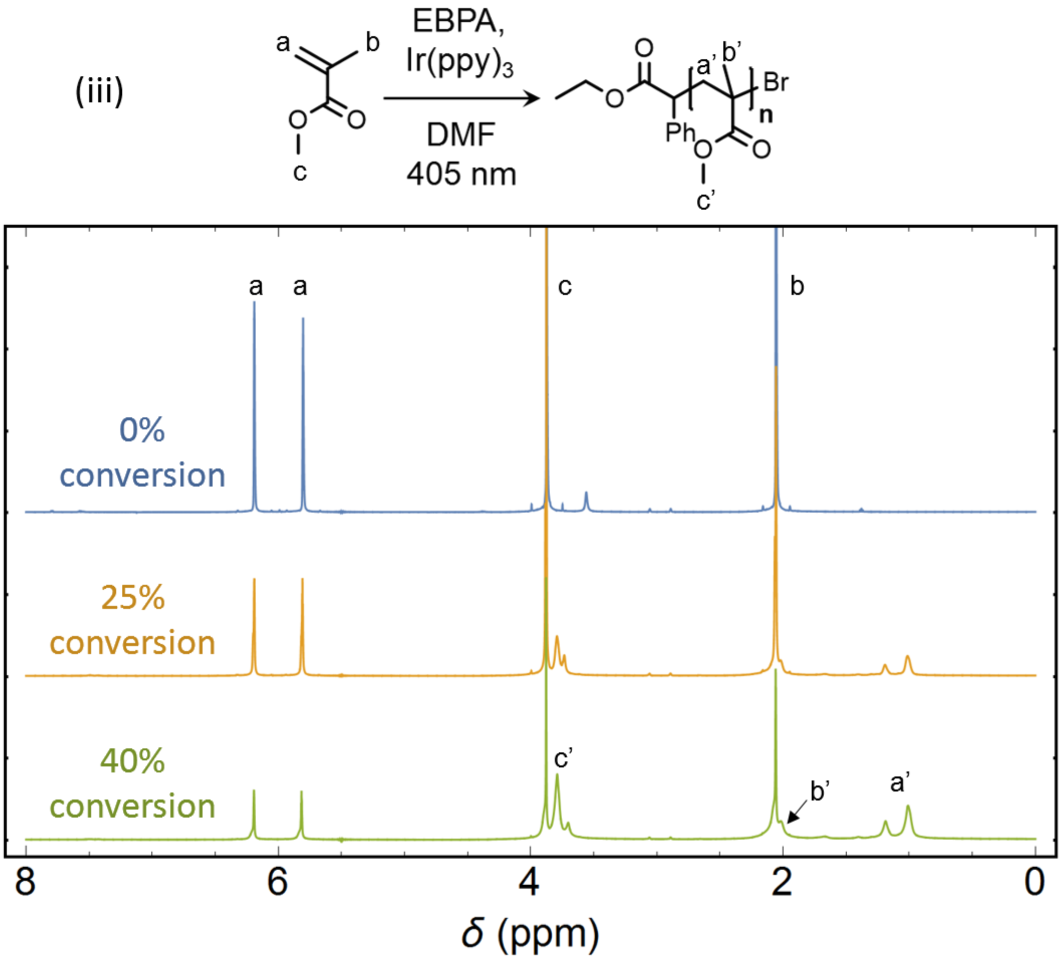

$$Conversion = \frac{\frac{2}{3}\int Peaks\ a', b'}{\int Peaks\ a + \frac{2}{3}\int Peaks\ a', b'}$$

Figure A11: Stack of $^1$H-NMR spectra of photo-ATRP of MMA at various stages of conversion. Peaks labeled a,b and a',b', respectively, were used for calculations according to the formula shown on the bottom.

Figure A12: Photograph of benchtop reaction of (i) using a 470 nm fiber-coupled LED.

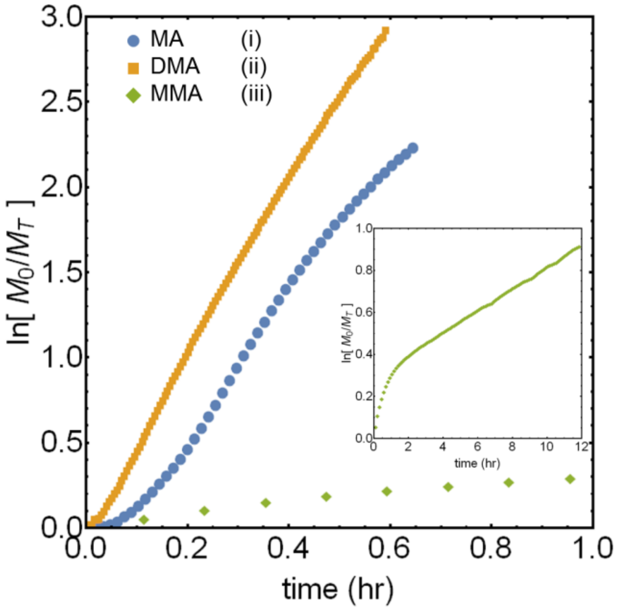

Figure A13: Kinetic traces of (i) under 470 nm irradiation at an intensity of 140 mW/cm$^2$ as well as (ii) and (iii) under 405 nm irradiation at an intensity of 114 mW/cm$^2$. Inset shows long-time kinetic profile of (iii).

Table A1: DOSY samples used to generate a calibration curve to determine DP.

| Mp | Mn | Mw | Đ | Relative Conversion (%) | Polymer added (mg/0.5 mL) | Monomer added (mg/0.5 mL) | Volume DMSO-d6 (µL) |
|---|---|---|---|---|---|---|---|
| 550 | 520 | 650 | 1.25 | 3.2 | 3.4 | 104.1 | 397 |
| 960 | 810 | 1000 | 1.23 | 5.6 | 6.0 | 101.5 | 396 |
| 1780 | 1430 | 1630 | 1.14 | 10.3 | 11.1 | 96.4 | 395 |
| 2880 | 2580 | 2790 | 1.08 | 16.7 | 18.0 | 89.5 | 394 |
| 4640 | 4060 | 4450 | 1.10 | 26.9 | 29.0 | 78.5 | 391 |
| 6850 | 5830 | 6380 | 1.09 | 39.8 | 42.8 | 64.7 | 388 |
| 10280 | 9800 | 10100 | 1.03 | 59.7 | 64.2 | 43.3 | 383 |

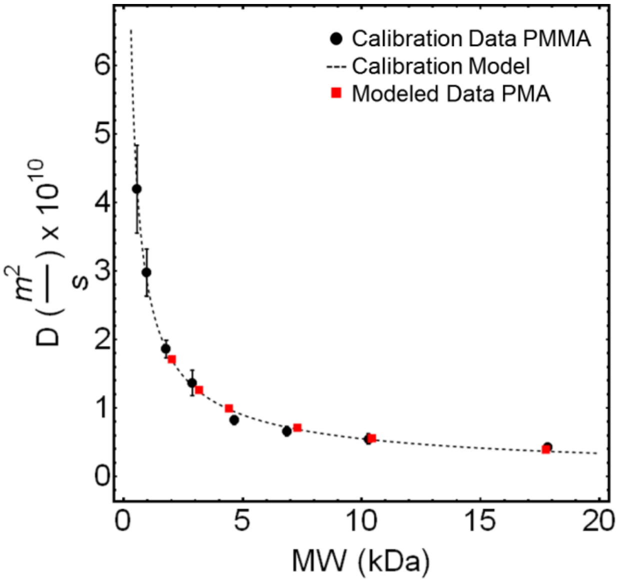

Figure A14: Diffusion vs molecular weight ($M_p$) plot for DOSY experiments using PMMA GPC standards. DOSY measurements used the factory standard Varian procedure, derived from literature procedures.[4] Dashed line represents model according to $D = A*MW^c$, where A and c are fitted parameters. Red squares represent the fitted experimental data for PMA by PET-RAFT using condition (i). Calibration sample compositions are provided in Table A1.

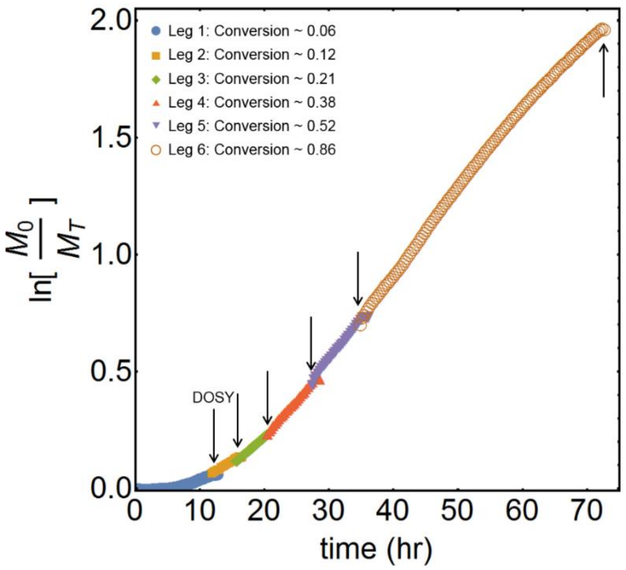

Figure A15: Results of $^{1}$H NMR scans taken between DOSY experiments (labelled with arrows). DOSY experiments were carried out with the light (LED) being turned off to ensure little to no growth during measurements.

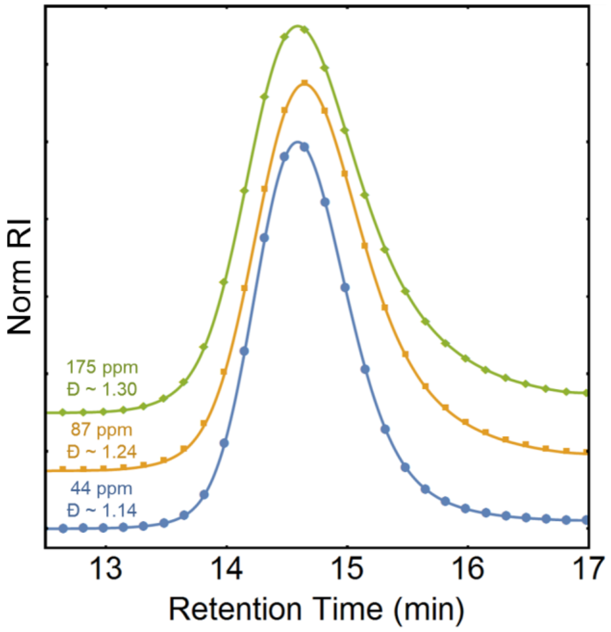

Figure A16: GPC traces of polymers shown in Figure 5. All peaks overlay, due to the in situ monitoring of conversion yielding polymers with similar molecular weights. As predicted by tracking the CTA, Đ values increase with increasing catalyst loading.

# REFERENCES

(1) Hemmer, J. R.; Poelma, S. O.; Treat, N.; Page, Z. A.; Dolinski, N. D.; Diaz, Y. J.; Tomlinson, W.; Clark, K. D.; Hooper, J. P.; Hawker, C.; et al. Tunable Visible and Near Infrared Photoswitches. *J. Am. Chem. Soc.* **2016**, *138* (42), 13960–13966.

(2) Mamiya, J. I.; Kuriyama, A.; Yokota, N.; Yamada, M.; Ikeda, T. Photomobile Polymer Materials: Photoresponsive Behavior of Cross-Linked Liquid-Crystalline Polymers with Mesomorphic Diarylethenes. *Chem. - A Eur. J.* **2015**, *21* (8), 3174–3177.

(3) Hanazawa, M.; Sumiya, R.; Horikawa, Y.; Irie. Thermally Irreversible Photochromic Systems. Reversible Photocyclization of 1,2-Bis( 2-Methyl Benzo[b]Thiophen-3-Yl)Perfluorocycloal Kene Derivatives. *J. Chem. Soc., Chem. Commun.* **1992**, *0*, 206–207.

(4) Jerschow, A.; Müller, N. Suppression of Convection Artifacts in Stimulated-Echo Diffusion Experiments. Double-Stimulated-Echo Experiments. *J. Magn. Reson.* **1997**, *125* (2), 372–375.

# Appendix B: Supporting Information for Chapter 3

The content of Appendix B was originally published in the *Journal of Polymer Science Part A*. Reproduced with permission from *J. Polym. Sci. Part A: Polym. Chem.* **2019**, 57, 3, 268–273. Copyright 2019, John Wiley and Sons

## Materials

All materials were purchased from Sigma Aldrich and used as received unless otherwise stated. All deuterated solvents were purchased from Fisher Scientific and used as received. Methyl acrylate (MA), methyl methacrylate (MMA), and polyethyleneglycol acrylate ($M_n$ ~400) were passed through a column of basic alumina (~150 mesh, Brockmann I grade) prior to use in order to remove the inhibitor. 3,7-di(4-biphenyl) 1-naphthalene-10-phenoxazine (PhenBP)[1], 10-phenylphenothiazine (PTH)[2], and [Cu(Me6-Tren)(O2CH)](ClO4)[3] were synthesized according to literature procedures. The Teflon insert was machined in house according to literature.[4] The optical fiber (FT1000UMT; End A flat cleave; End BSMA adapter; Furcation Tubing-FT038), and the fiber-coupled LEDs 365 nm (M365FP1), 405 nm (M405FP1), 470 nm (M470F3), 530 nm (M530F2), were purchased from Thorlabs.

## Instrumentation

All nuclear magnetic resonance spectra were recorded on a Varian 600 MHz spectrometer with a regulated temperature of 25 °C. Size exclusion chromatography (SEC) for molecular weight analysis, relative to linear polystyrene standards, was performed on a Waters 2690 separation module equipped with Waters 2414 refractive index and 2996 photodiode array detectors using $CHCl_3$-containing 0.25%

triethylamine as eluent at a flow rate of 1 mL/min. For photopolymerizations in the NMR spectrometer, the LED was coupled into a multimode optical fiber terminated with a flat cleave and the intensity and ‘on’ / ‘off’ cycles were controlled through methods described previously.[4]

### Sample preparation

Polymerizations were prepared in 1 dram vials with 33% monomer targeting 150 repeat units (~1.5 mL batches). Catalytic loadings were chosen as appropriate from the corresponding literature. After mixing, the samples were sparged with Ar for 5 minutes prior to transfer into a foiled NMR tube (Ar atmosphere provided via balloon). The foil was removed and the NMR tube was then quickly loaded with the optical fiber and inserted into the NMR for measurement.

## LED selection

Excitation wavelengths were chosen such that the calculated absorbance for a sample at 1 cm (using Beer's Law) was maximized, but below 0.25, as recommended in previous work[4] to ensure even irradiation conditions. In the case of highly absorbing catalysts, or the presence of a large UV shoulder, LEDs with output maxima slightly shifted from the peak/shoulder were chosen to satisfy the absorbance requirements.

**Table B1**: LEDs used for each catalyst studied

| **Catalyst System** | **Solvent** | **LED (nm)** |
|---|---|---|
| $Ru(bpy)_3Cl_2$ | DMSO-$d_6$ | 470 |
| ZnTPP | DMSO-$d_6$ | 530 |
| PTH | DMF-$d_7$ | 405 |
| $Ir(ppy)_3$ | DMF-$d_7$ | 405 |
| PhenBP | DMF-$d_7$ | 470 |
| $CuBr_2/Me_6TREN$ | DMSO-$d_6$/DMF-$d_7$ | 405 |
| $CuBr_2/Me_6TREN$ | $D_2O$ | 365 |
| Cu-Formate Complex | DMSO-$d_6$ | 365 |
| $CuBr_2$/TPMA | DMSO-$d_6$ | 405 |

## Fiber-coupled NMR setup

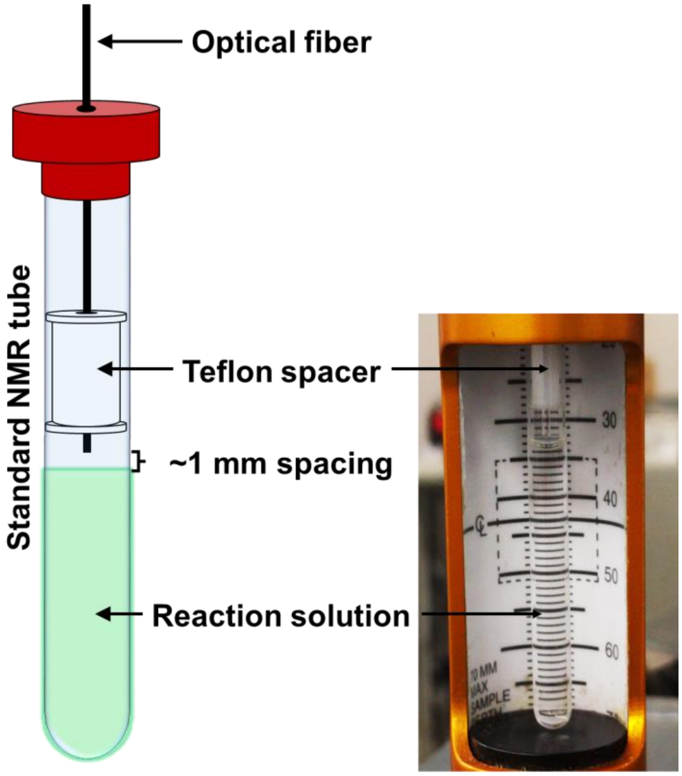

**Figure B1**: (Left) Cartoon schematic of the fiber-coupled NMR setup. (Right) Photograph of the ‘active’ portion of the setup, where the Teflon spacer centers the tip of the optical fiber ~1 mm from the top of the reaction solution. Full details on spacer dimensions and necessary hardware for operation given in previous work.[4]

## NMR processing

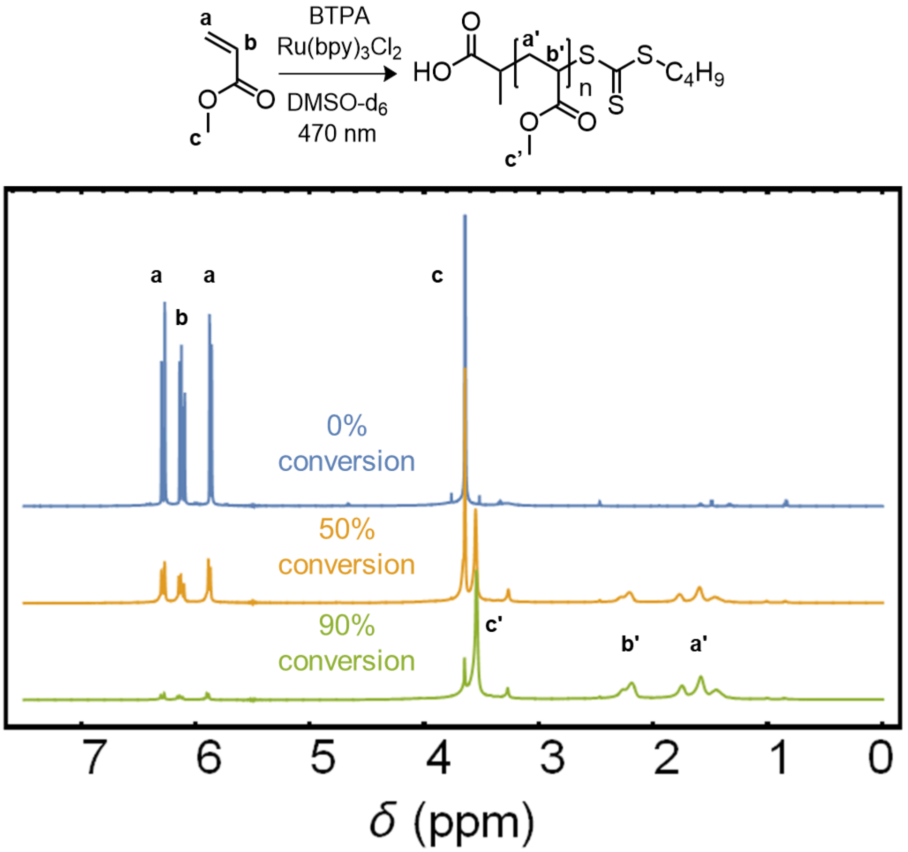

**Figure B2**: Representative $^1$H-NMR spectra for the polymerization of MA by PET-RAFT at various stages of conversion. Peaks labeled a, a’, b, and b’ were used for calculations according to the formula shown below. Additional peaks are labeled for completion.

$$Conversion = \frac{\int Peaks\ a', b'}{\int Peaks\ a, b + \int Peaks\ a', b'}$$

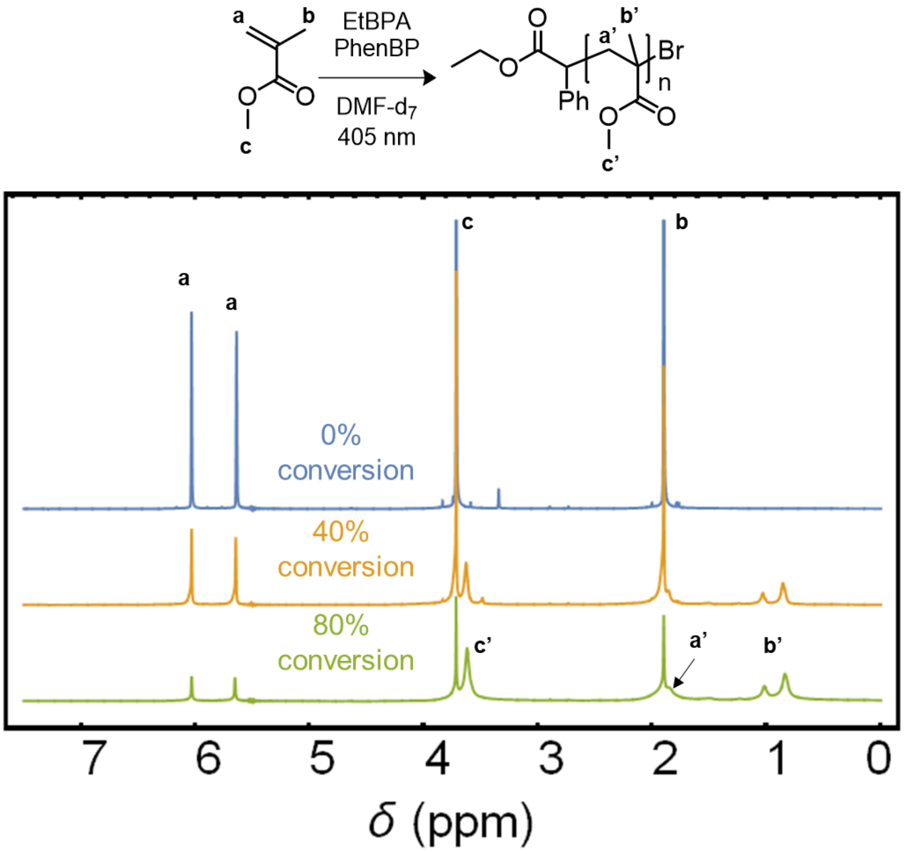

**Figure B3**: Representative $^1$H-NMR spectra for the polymerization of MMA by Cu-free ATRP at various stages of conversion. Peaks labeled a and b' were used for calculations according to the formula shown below. Additional peaks are labeled for completion.

$$Conversion = \frac{\frac{2}{3}\int Peaks\ b'}{\int Peaks\ a + \frac{2}{3}\int Peaks\ b'}$$

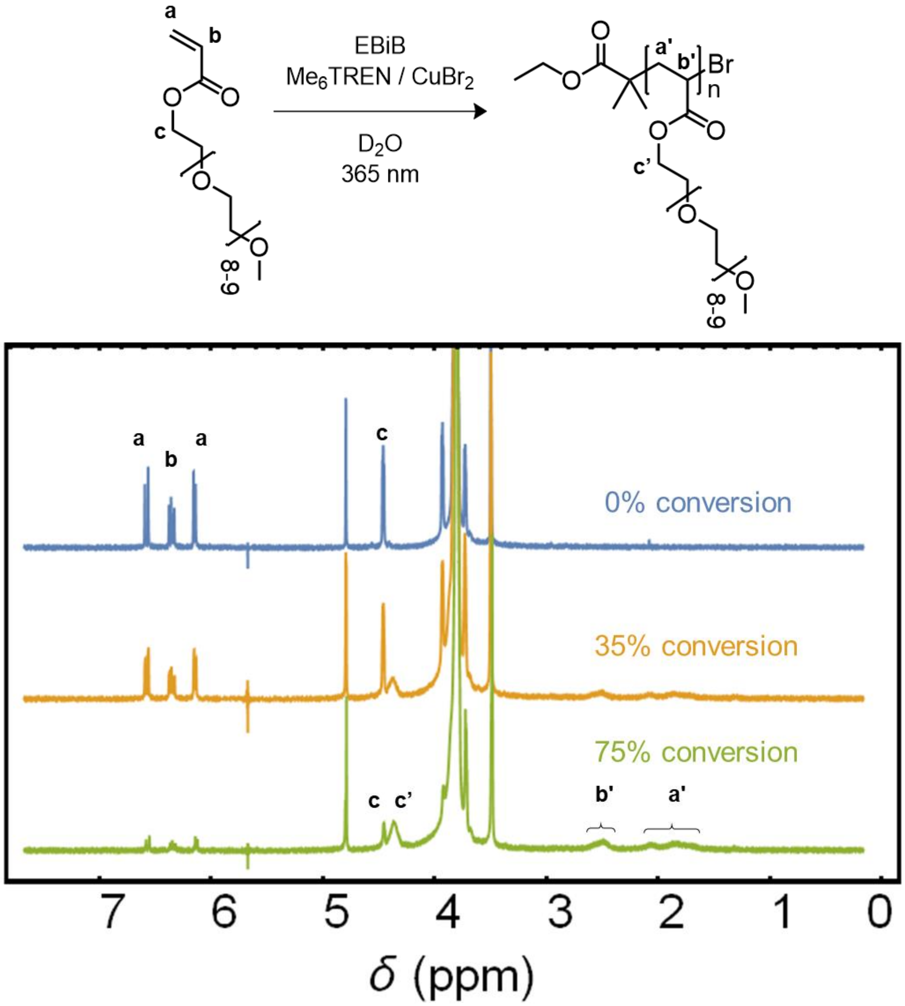

**Figure B4**: Representative $^1$H-NMR spectra for the polymerization of PEGA by Cu-mediated RDRP (aqueous) at various stages of conversion. Peaks labeled a, b, c, and c' were used for calculations according to the formula shown below. Additional peaks are labeled for completion.

$$Conversion = 1 - \frac{\frac{2}{3}\int Peaks\ a, b}{\int Peaks\ c, c'}$$

# Characterization

## LED outputs

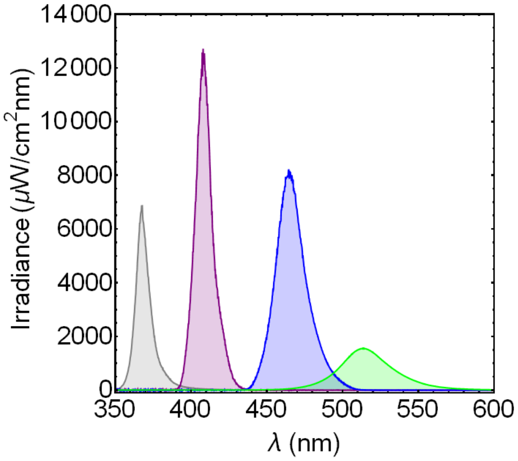

**Figure B5**: Irradiance measurements of the various LEDs (365, 405, 470, and 530 nm) used in this work at 100% current.

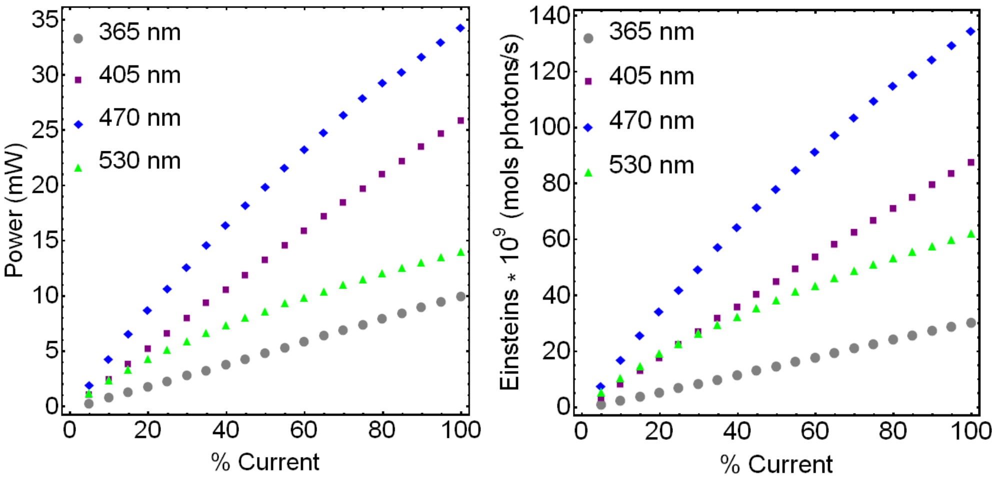

**Figure B6**: (Left) Power measurements for the fiber coupled LEDs at various supplied currents. (Right) The power measurements converted to photon flux (see equation below). All experiments were run such that the photon flux was constant (using the value for the weakest LED at 100% current).

$$Photon\ flux\ (Einsteins) = \frac{P * \lambda}{h * c * N_A}$$

Where P is LED power (W), λ is peak LED wavelength (m), h is Planck's constant (J·s), c is the speed of light (m/s), and $N_A$ is Avogadro's Number

**Table B2**: Irradiation conditions used in this study with constant photon flux

| LED Wavelength (nm) | Current for equal photon flux (%) |
|---|---|
| 365 | 100 |
| 405 | 34.0 |
| 470 | 17.7 |
| 530 | 36.6 |

## Catalyst absorption profiles

### PET-RAFT

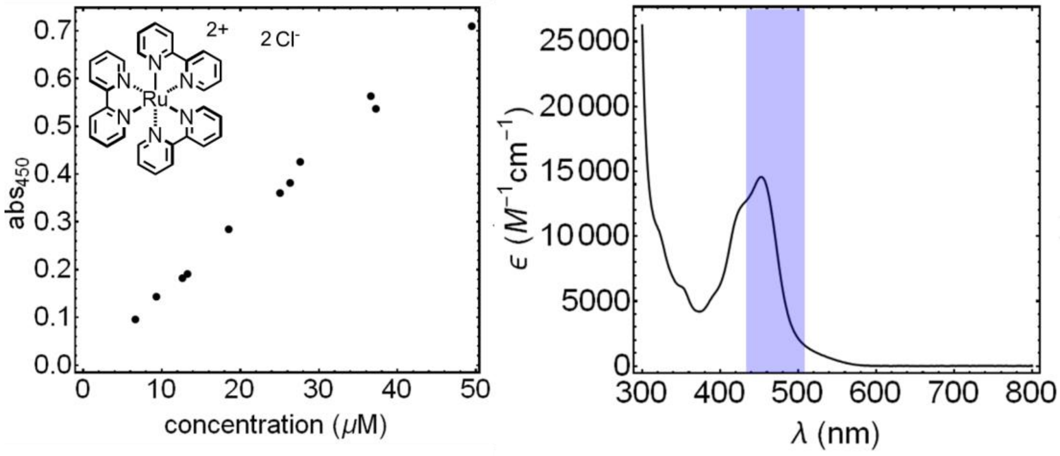

**Figure B7**: (Left) UV-vis measurements to determine the molar extinction coefficient of $Ru(bpy)_3Cl_2$ in DMSO. (Right) Trace of the calculated extinction for $Ru(bpy)_3Cl_2$ and overlap with 470 nm light.

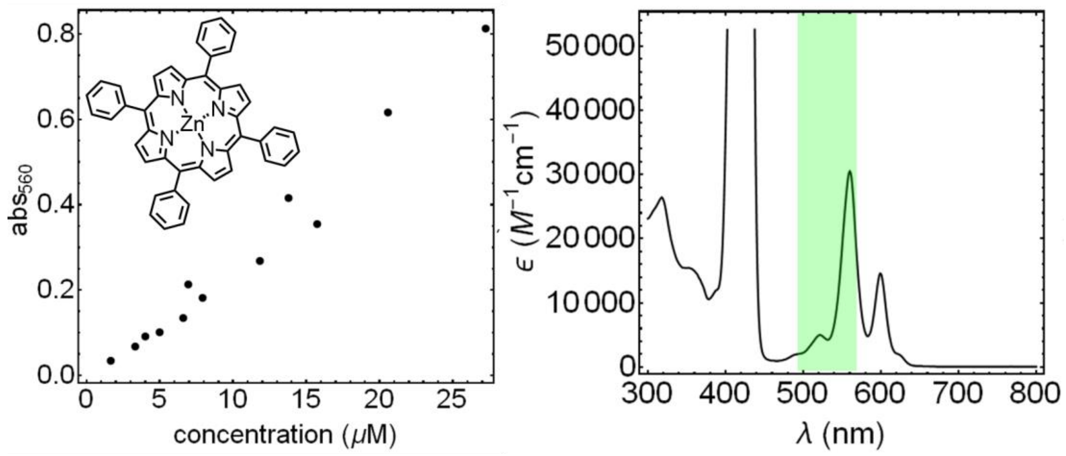

**Figure B8**: (Left) UV-vis measurements to determine the molar extinction coefficient of ZnTPP in DMSO. (Right) Trace of the calculated extinction for ZnTPP and overlap with 530 nm light.

## Cu-free ATRP

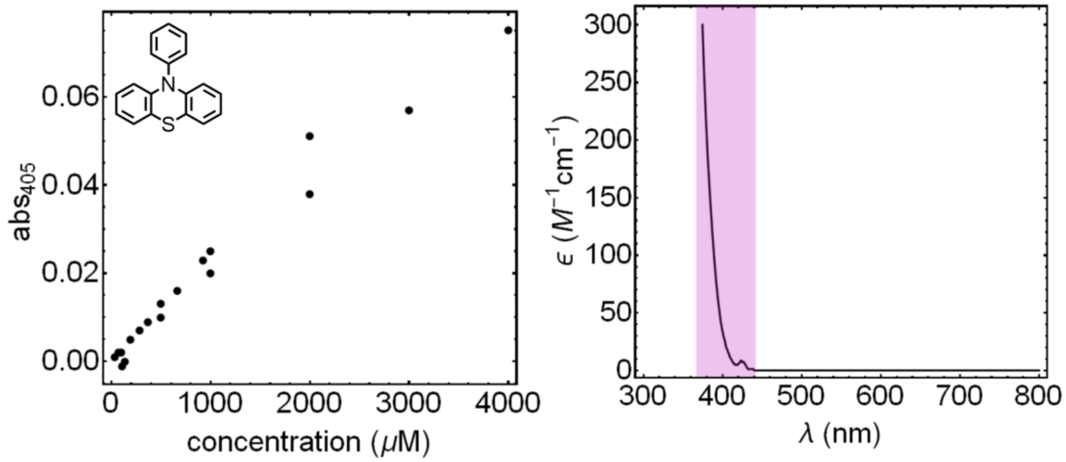

**Figure B9**: (Left) UV-vis measurements to determine the molar extinction coefficient of PTH in DMF. (Right) Trace of the calculated extinction for PTH and overlap with 405 nm light.

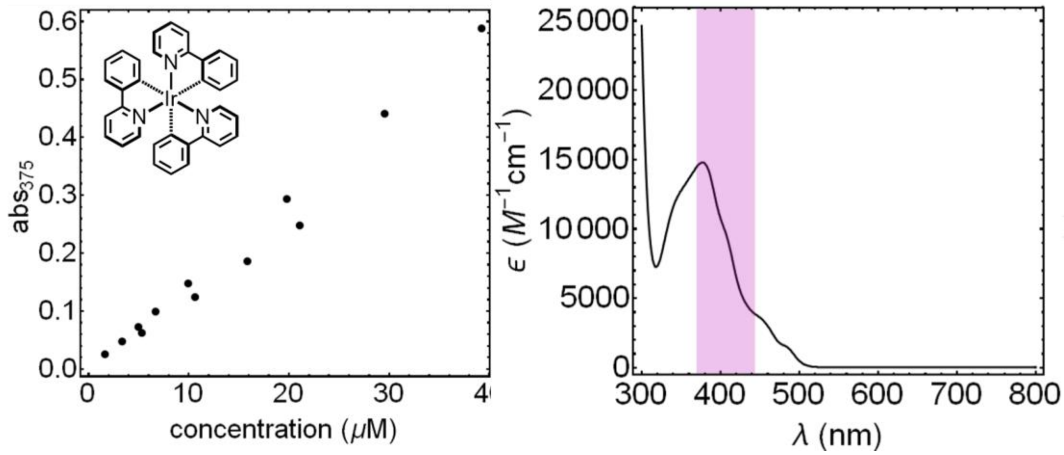

**Figure B10**: (Left) UV-vis measurements to determine the molar extinction coefficient of Ir(ppy)$_3$ in DMF. (Right) Trace of the calculated extinction for Ru(bpy)$_3$Cl$_2$ and overlap with 405 nm light.

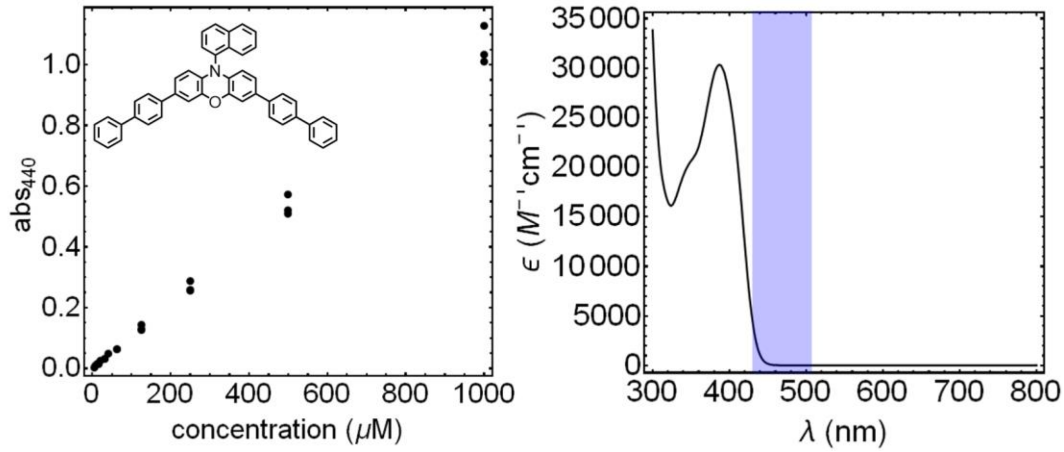

**Figure B11**: (Left) UV-vis measurements to determine the molar extinction coefficient of PhenBP in DMF. (Right) Trace of the calculated extinction for PhenBP and overlap with 470 nm light.

## Cu-mediated RDRP

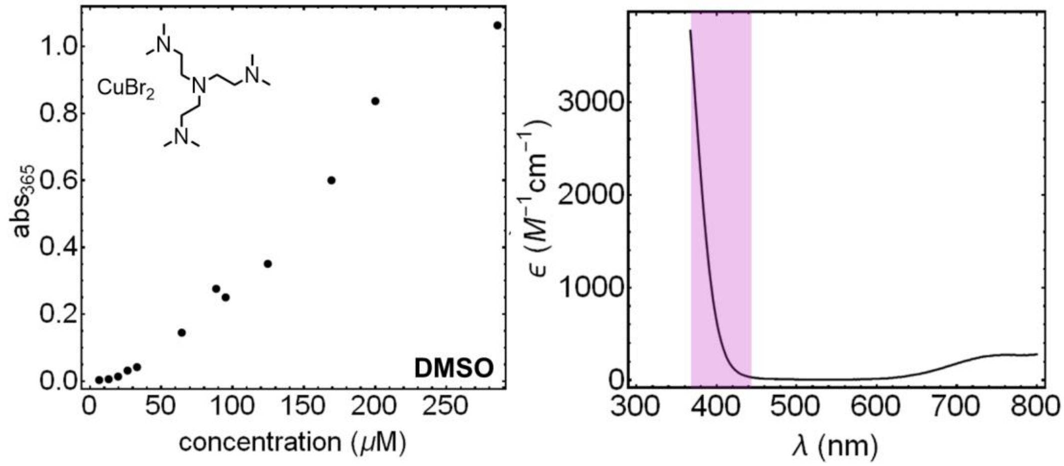

**Figure B12**: (Left) UV-vis measurements to determine the molar extinction coefficient of $CuBr_2$ / $Me_6TREN$ in DMSO. (Right) Trace of the calculated extinction for $CuBr_2$ / $Me_6TREN$ and overlap with 405 nm light.

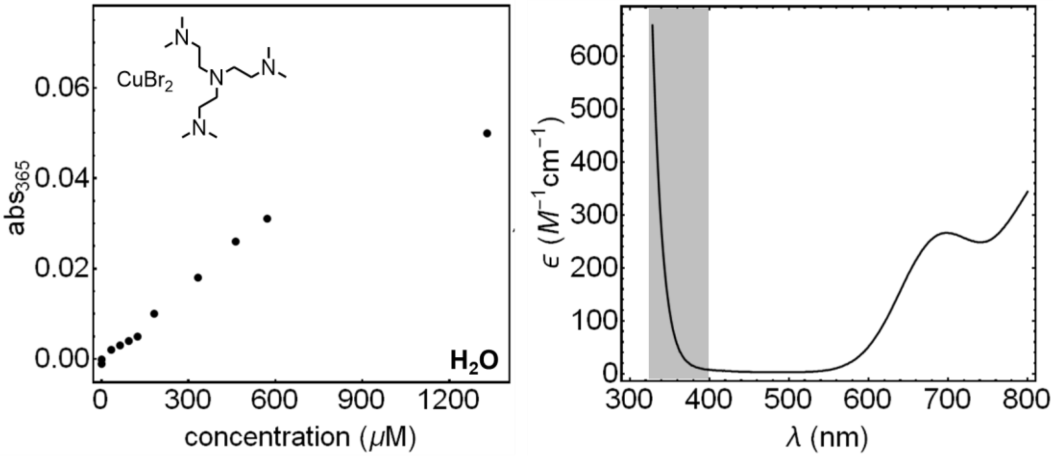

**Figure B13**: (Left) UV-vis measurements to determine the molar extinction coefficient of $CuBr_2$ / $Me_6TREN$ in $H_2O$. (Right) Trace of the calculated extinction for $CuBr_2$ / $Me_6TREN$ and overlap with 365 nm light. It should be noted that moving to water significantly shifted the absorbances relative to DMSO, necessitating the use of 365 nm light.

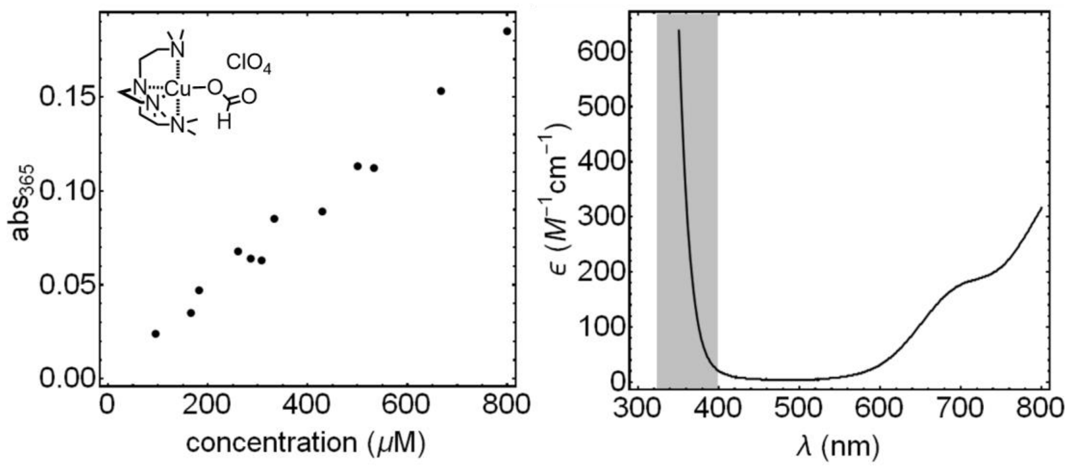

**Figure B14**: (Left) UV-vis measurements to determine the molar extinction coefficient of [Cu(Me6-Tren)(O2CH)](ClO4), the Cu-formate complex, in DMSO. (Right) Trace of the calculated extinction for the Cu-formate complex and overlap with 365 nm light.

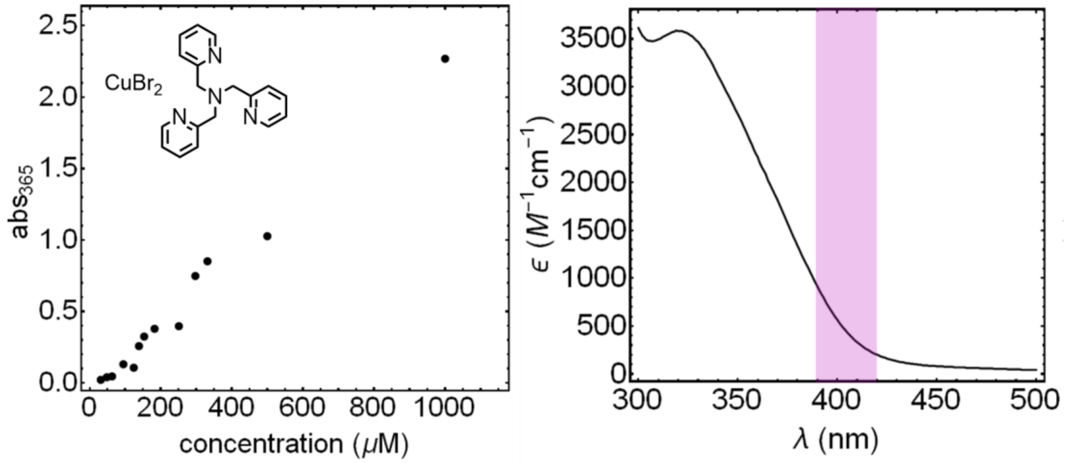

**Figure B15**: (Left) UV-vis measurements to determine the molar extinction coefficient of $CuBr_2$ / TPMA in DMSO. (Right) Trace of the calculated extinction for $CuBr_2$ / TPMA and overlap with 405 nm light.

## Polymerization kinetics, cycling experiments, and extended 'off' periods

### PET-RAFT (MA)

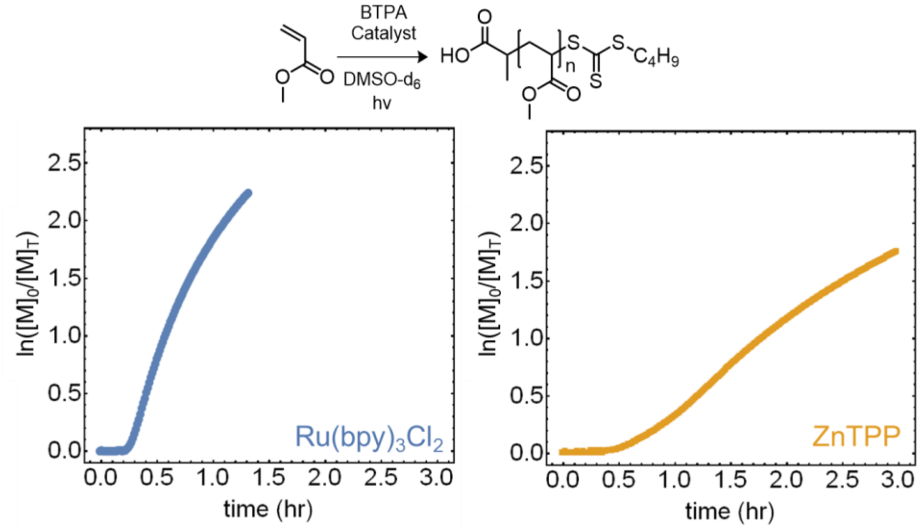

**Figure B16**: Kinetic traces of PET-RAFT polymerizations of MA using Ru(bpy)$_3$Cl$_2$ (left) and ZnTPP (right) under 470 and 530 nm irradiation, respectively.

**Table B3**: Summary of PET-RAFT polymerizations of MA and results

| catalyst | λ (nm) | [M]:[I]:[catalyst] | time (hr) | conversion | $M_{n,theo}$ | $M_{n,exp}$ (SEC) | Đ |
|---|---|---|---|---|---|---|---|
| Ru(bpy)$_3$Cl$_2$ | 470 | 150 : 1 : 0.002 | 1.3 | 0.89 | 11700 | 14300 | 1.16 |
| ZnTPP | 530 | 150 : 1 : 0.005 | 3 | 0.83 | 11000 | 13400 | 1.15 |

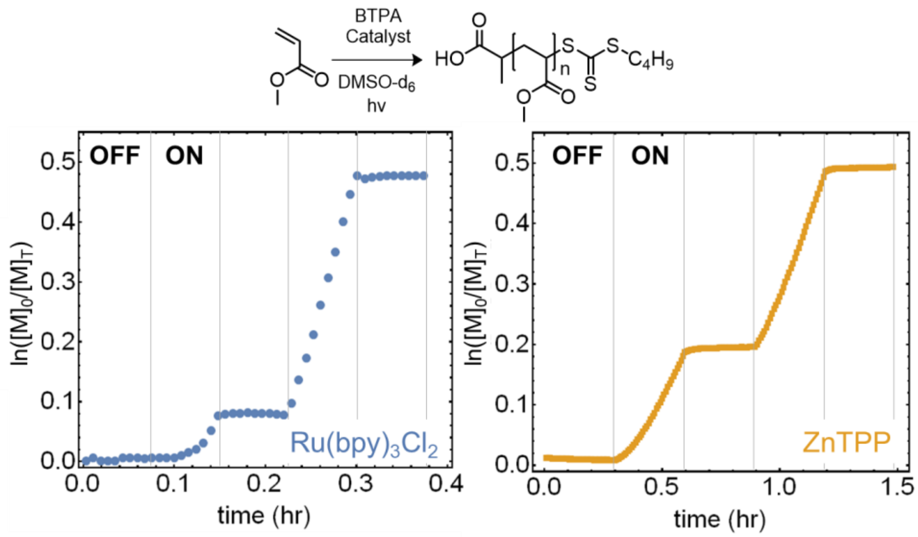

**Figure B17**: Temporal control cycles for PET-RAFT polymerizations of MA using Ru(bpy)$_3$Cl$_2$ (left) and ZnTPP (right) under 470 and 530 nm irradiation, respectively. Both polymerizations demonstrate rapid and ideal halting of conversion upon turning off the light.

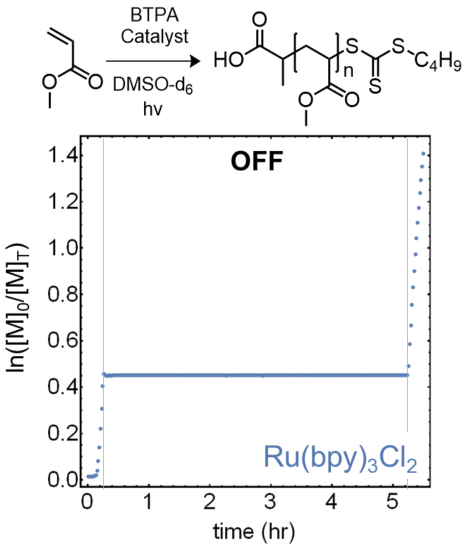

**Figure B18**: An extended off cycle for the PET-RAFT polymerization of MA using Ru(bpy)$_3$Cl$_2$ under 470 nm irradiation, clearly demonstrating ideal temporal control over the polymerization. Furthermore, the polymerization could be readily re-started upon further irradiation.

## Cu-free ATRP (MMA)

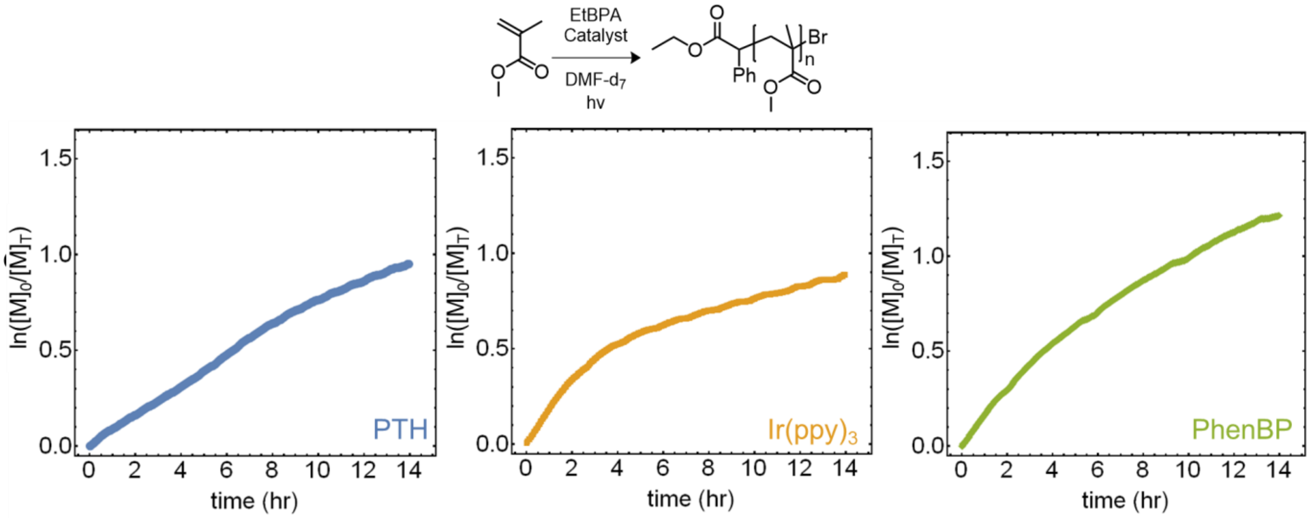

**Figure B19**: Kinetic traces of Cu-free ATRP of MMA using PTH (left), $Ir(ppy)_3$ (center), and PhenBP under 405, 405, and 470 nm irradiation, respectively.

**Table B4**: Summary of Cu-free ATRP of MMA and results

| catalyst | λ (nm) | [M]:[I]:[catalyst] | time (hr) | conversion | $M_{n,theo}$ | $M_{n,exp}$ (SEC) | Đ |
|---|---|---|---|---|---|---|---|
| PTH | 405 | 150 : 1 : 0.1 | 14 | 0.61 | 9400 | 11100 | 1.83 |
| $Ir(ppy)_3$ | 405 | 150 : 1 : 0.02 | 14 | 0.58 | 9000 | 7000 | 1.77 |
| PhenBP | 470 | 150 : 1 : 0.1 | 14 | 0.70 | 10800 | 17700 | 1.55 |

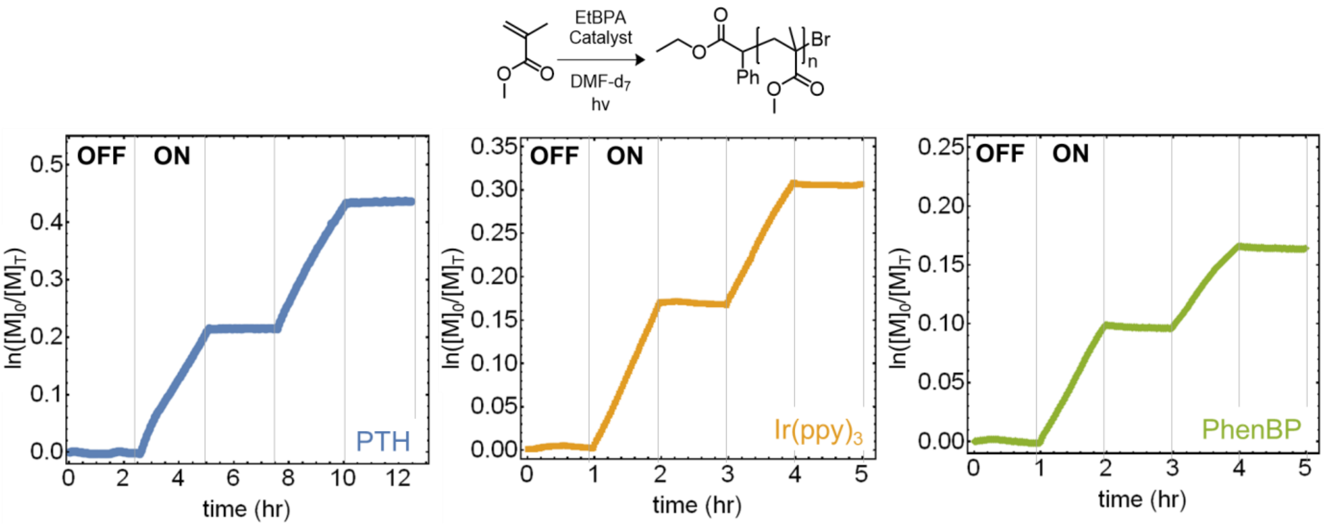

**Figure B20**: Temporal control cycles of Cu-free ATRP of MMA using PTH (left), Ir(ppy)$_3$ (center), and PhenBP under 405, 405, and 470 nm irradiation, respectively. All three polymerizations demonstrate rapid and ideal halting of conversion upon turning off the light.

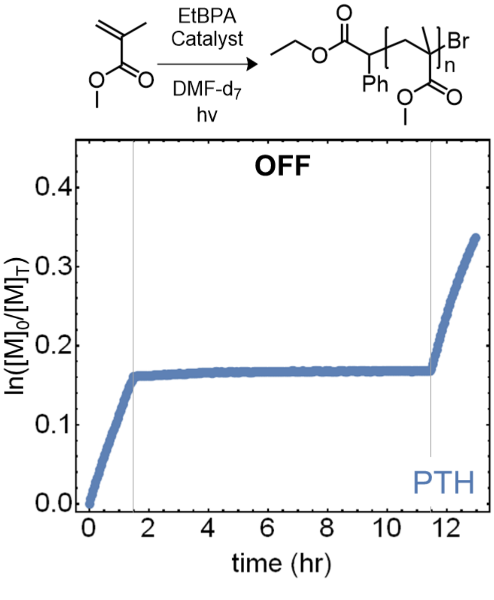

**Figure B21**: An extended off cycle for the Cu-free ATRP of MMA using PTH under 405 nm irradiation, clearly demonstrating ideal temporal control over the polymerization. Furthermore, the polymerization could be readily re-started upon further irradiation.

## Cu-mediated RDRP (MA)

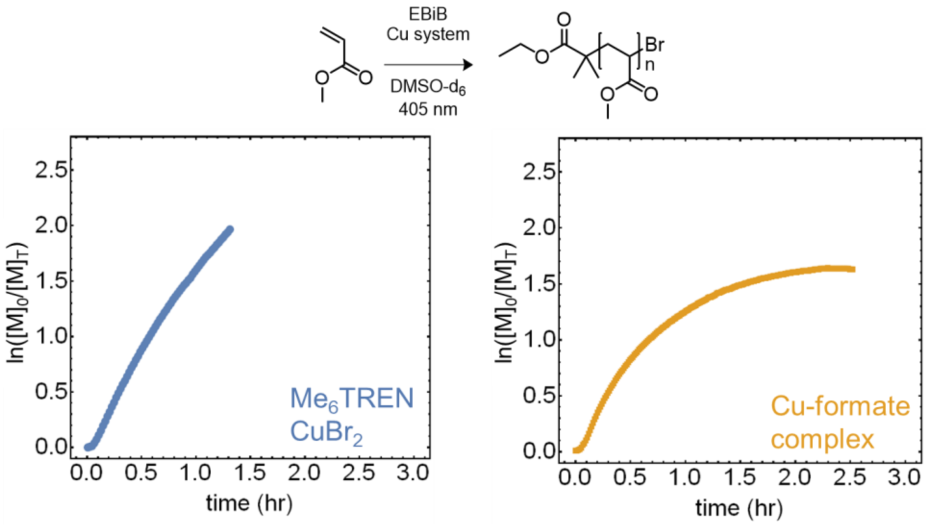

**Figure B22**: Kinetic traces of the Cu-mediated RDRP of MMA using $CuBr_2$/$Me_6$TREN (left) and the discrete Cu-formate complex (right) under 405 nm irradiation. Significant termination events can be seen in the case of the complex after ~75% conversion.

**Table B5**: Summary of Cu-mediated RDRP of MA and results

| ligand/catalyst | λ (nm) | [M]:[I]:[$CuBr_2$]:[ligand] | time (hr) | conversion | $M_{n,theo}$ | $M_{n,exp}$ (SEC) | Đ |
|---|---|---|---|---|---|---|---|
| $Me_6$TREN | 405 | 150 : 1 : 0.02 : 0.12 | 1.3 | 0.86 | 11300 | 11000 | 1.09 |
| Cu-formate complex | 365 | 150 : 1 : 0.08 : ----- | 2.5 | 0.80 | 10500 | 9000 | 1.15 |

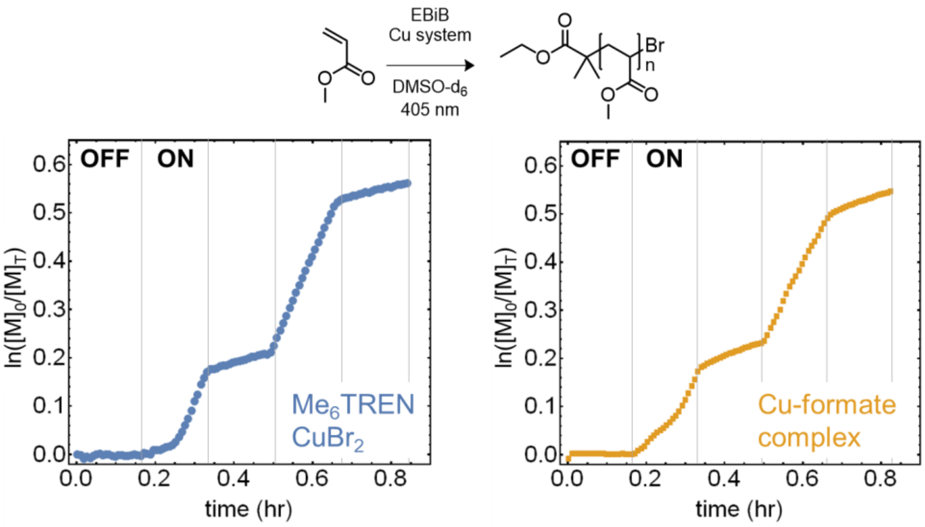

**Figure B23**: Temporal control cycles for the Cu-mediated RDRP of MMA using $CuBr_2$/$Me_6$TREN (left) and the discrete Cu-formate complex (right) under 405 nm irradiation. Both Cu-mediated RDRP reactions demonstrate significant and linear growth during off periods after initial irradiation, corresponding to ~10% and ~15% of the on rate, respectively.

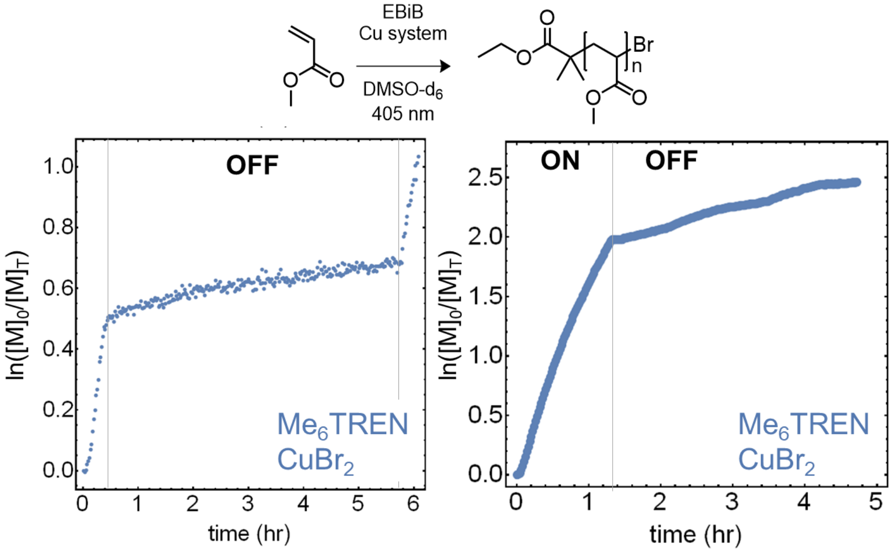

**Figure B24**: Extended off cycles for the Cu-mediated RDRP of MMA using $CuBr_2$/$Me_6$TREN under 405 nm irradiation, clearly demonstrating extended linear growth during off periods at intermediate (left) and high (right) conversions. Upon reirradiation, polymerization resumes at a rate comparable to the initial rate (left).

## Cu-mediated RDRP (MMA)

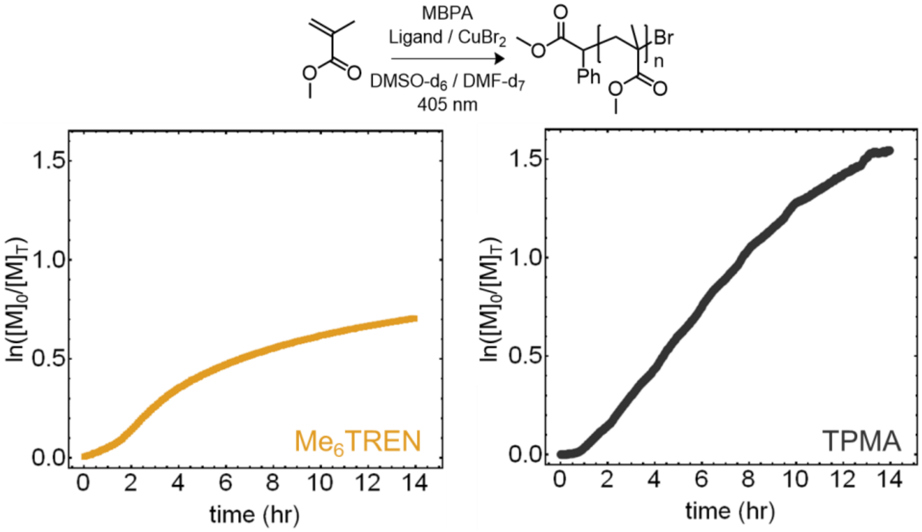

**Figure B25**: Kinetic traces of the Cu-mediated RDRP of MMA using $CuBr_2$/$Me_6TREN$ (left) in DMF-$d_7$ and $CuBr_2$/TPMA (right) in DMSO-$d_6$ under 405 nm irradiation. Both systems demonstrated similar growth at low conversions (below ~35%) making them ideal for comparison in temporal studies.

**Table B6**: Summary of Cu-mediated RDRP of MMA and results

| **ligand** | **λ (nm)** | **[M]:[I]:[CuBr$_2$]:[ligand]** | **time (hr)** | **conversion** | **$M_{n,theo}$** | **$M_{n,exp}$ (SEC)** | **Đ** |
|---|---|---|---|---|---|---|---|
| $Me_6TREN$ | 405 | 150 : 1 : 0.03 : 0.18 | 14 | 0.50 | 7700 | 5200 | 1.42 |
| TPMA | 405 | 150 : 1 : 0.03 : 0.18 | 14 | 0.79 | 12100 | 9400 | 1.15 |

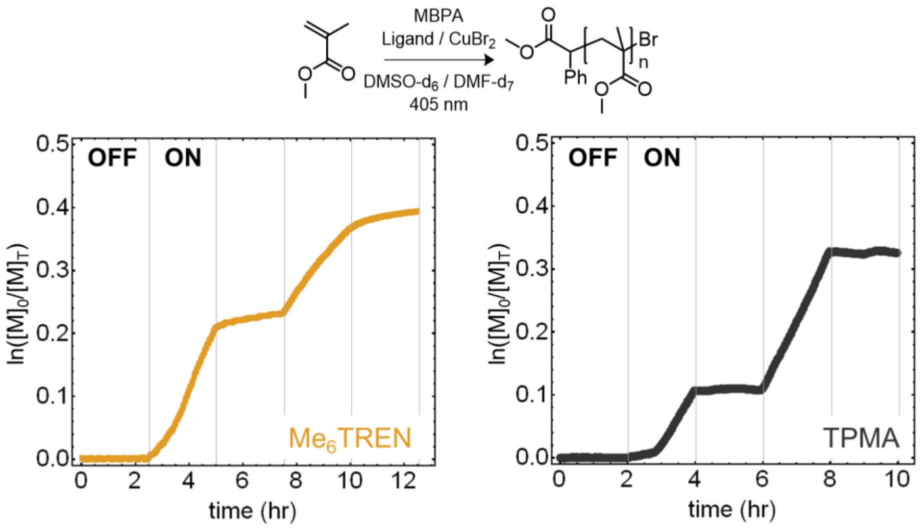

**Figure B26**: Temporal control of the Cu-mediated RDRP of MMA using $CuBr_2$/$Me_6$TREN (left) in DMF-$d_7$ and $CuBr_2$/TPMA (right) in DMSO-$d_6$ under 405 nm irradiation. Both Cu-mediated RDRP reactions demonstrate growth during off periods after initial irradiation, although in the case of $CuBr_2$/TPMA, this growth only corresponds to ~2% of the on rate.

## Cu-mediated RDRP (PEGA)

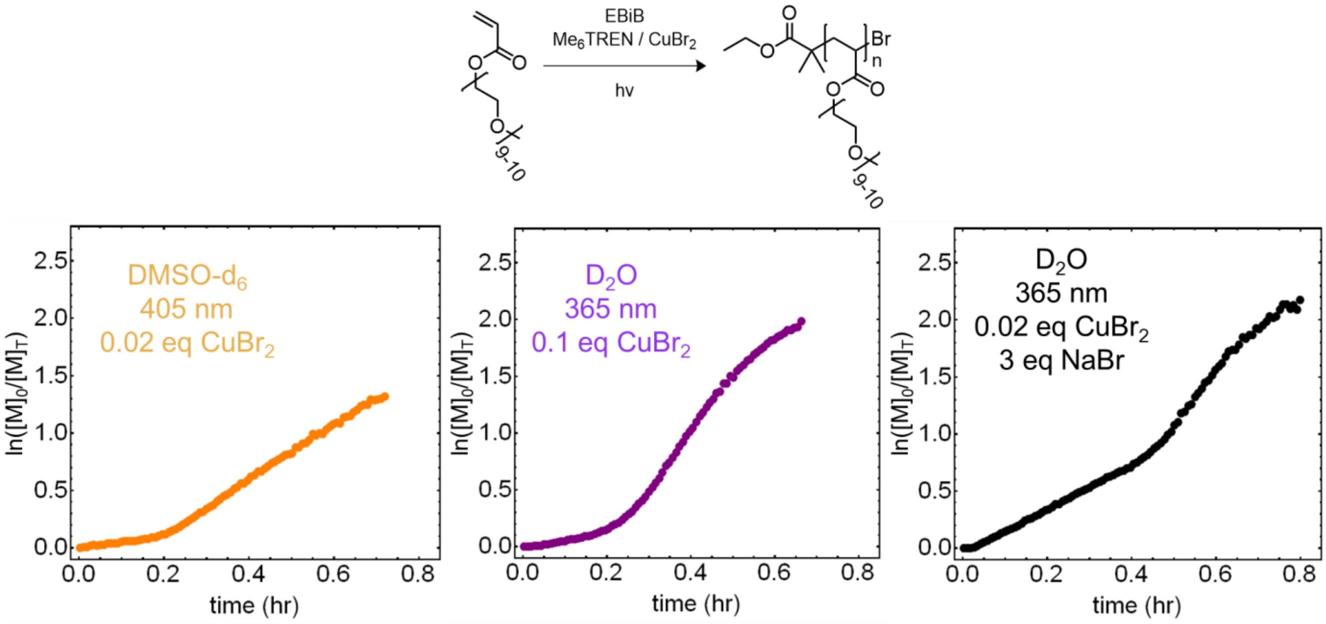

**Figure B27**: Kinetic traces of the Cu-mediated RDRP of PEGA in DMSO-$d_6$ and $D_2O$ using $CuBr_2$/$Me_6TREN$ under various conditions.

**Table B7**: Summary of Cu-mediated RDRP of PEGA and results

| solvent | λ (nm) | [M]:[I]:[$CuBr_2$]:[ligand]:[NaBr] | time (hr) | conversion | $M_{n,theo}$ | $M_{n,exp}$ (SEC) | Đ |
|---|---|---|---|---|---|---|---|
| DMSO-$d_6$ | 405 | 150 : 1 : 0.02 : 0.12 : - | 0.7 | 0.73 | 53000 | 45500 | 1.20 |
| $D_2O$ | 365 | 150 : 1 : 0.10 : 0.12 : - | 0.7 | 0.86 | 62400 | 48100 | 1.22 |
| $D_2O$ | 365 | 150 : 1 : 0.02 : 0.12 : 3 | 0.8 | 0.89 | 64600 | 53200 | 1.19 |

## References

(1) Pearson, R. M.; Lim, C. H.; McCarthy, B. G.; Musgrave, C. B.; Miyake, G. M. Organocatalyzed Atom Transfer Radical Polymerization Using N-Aryl Phenoxazines as Photoredox Catalysts. *J. Am. Chem. Soc.* **2016**, *138* (35), 11399–11407.

(2) Treat, N. J.; Sprafke, H.; Kramer, J. W.; Clark, P. G.; Barton, B. E.; Read De Alaniz, J.; Fors, B. P.; Hawker, C. J. Metal-Free Atom Transfer Radical Polymerization. *J. Am. Chem. Soc.* **2014**, *136* (45), 16096–16101.

(3) Anastasaki, A.; Nikolaou, V.; Brandford-Adams, F.; Nurumbetov, G.; Zhang, Q.; Clarkson, G. J.; Fox, D. J.; Wilson, P.; Kempe, K.; Haddleton, D. M. Photo-Induced Living Radical Polymerization of Acrylates Utilizing a Discrete Copper(II)-Formate Complex. *Chem. Commun.* **2015**, *51* (26), 5626–5629.

(4) Dolinski, N. D.; Page, Z. A.; Eisenreich, F.; Niu, J.; Hecht, S.; Read de Alaniz, J.; Hawker, C. J. A Versatile Approach for In Situ Monitoring of Photoswitches and Photopolymerizations. *ChemPhotoChem* **2017**, *1* (4), 125–131.

## Appendix C: Supporting Information for Chapter 4

The content of Appendix C was originally published in *Advanced Materials*.
Reproduced with permission from *Adv. Mater.* **2018**, 30, 31, 1800364.

### Materials

Chemicals. All chemicals were used as received unless otherwise noted. Aluminum oxide activated (basic, Brockmann I), methyl acrylate (MA, 99%, contains ≤100 ppm monomethyl ether hydroquinone as inhibitor), tetra(ethylene glycol) diacrylate (TEGDA, technical grade, contains 150-200 ppm MEHQ as inhibitor, 100-150 ppm HQ as inhibitor), *N,N*-dimethylacrylamide (DMA, 99%, contains 500 ppm monomethyl ether hydroquinone as inhibitor), 1,4-butanediol diacrylate (BDA, technical grade, contains ~75 ppm hydroquinone as inhibitor, 90%), 3,4-epoxycyclohexylmethyl 3,4-epoxycyclohexanecarboxylate (ECC), acryloyl chloride (≥97%, contains ~400 ppm phenothiazine as stabilizer), and triethylamine (TEA, ≥99.5%) were purchased from Sigma Aldrich and inhibitors were removed by running through a plug of basic alumina for all monomers apart from acryloyl chloride. Dichloromethane (99.8%, extra dry) and DL-camphorquinone (CQ, 99%), benzothiophene (97%), methyliodide (99%, stabilized with copper), and *n*-butyllithium (2.3 M solution in cyclohexane) were purchased from ACROS organics™. (3-ethyloxetan-3-yl)methanol (OXA. 98%) was purchased from Arc Pharm Inc. and used as received. Ethyl 4-(dimethylamino)benzoate (EDMAB, 99%) was purchased from Alfa Aesar. [4-[Octyloxy]phenyl]phenyliodonium hexafluoroantimonate (H-Nu 254), 2-(butyryloxy)-*N*,*N*,*N*-trimethylethan-1-aminium butyltriphenylborate (Borate), and 6-hydroxy-2,4,5,7-tetraiodo-3*H*-xanthen-3-one (H-Nu 535) were purchased from Spectra group limited. 3-methyl-1-benzothiophene (>96%) and octafluorocyclopentene (>98%) were purchased from TCI. N-bromosuccinimide (99%) was purchased from ABCR. XHT-500 fluorinated oil was purchased from Grainger.

LEDs: 470 nm (M470F3), 530 nm (M530F2), collimated 530 nm (M530L3-C1) were purchased from Thorlabs.

### Instrumentation

Nanoindenation was performed on an iMicro Nanoindenter (Nanomechanics, Inc., Oak Ridge, TN, USA). A 10 μm radius sphero-conical tip was used. Tests went to a maximum load of 5 mN at a loading and unloading rate of 1 mN/s. A 10 second hold at the maximum load was used to avoid the "nose" problem which occurs due to the visco-elastic nature of polymers[1]. The hardness and modulus were obtained from the compliance method as described by Briscoe et al[1] using the area function for a spherical tip.

Tensile tests on the stiffer materials (**G1, B1, Blue cured B1:G2 blends**) were performed on a displacement-controlled tensile tester with a 100-lb load cell. The strain rate was $8 \cdot 10^{-4}$ $s^{-1}$. Strains were measured by digital image correlation (DIC), using Vic-2D software (Correlated Solutions, Inc., Columbia, SC, USA). A digital camera (Point Grey Research Grasshopper, Richmond, BC, Canada) with a CCD resolution of 2448x2048 pixels and a 70-180 mm lens (Nikon ED AF Micro Nikkor) was used for imaging. The magnification of these images was 7.5 μm/pixel. Speckle patterns for DIC were made by painting a white base coat on the samples followed by speckling with black spray paint. The strain resolution was found to be $5 \cdot 10^{-6}$ for this method.

Tensile tests on softer materials (**G2, B2, Green cured B1:G2 blends**) were performed on a displacement-controlled tensile tester (MTS Bionix2000) with a 10-lb load cell. Strains were calculated as a function of displacement.

Profilometry was performed using a Bruker DektakXT Stylus Profilometer for 1 mm lengths on printed cone samples held in a custom printed holder to ensure flat surfaces.

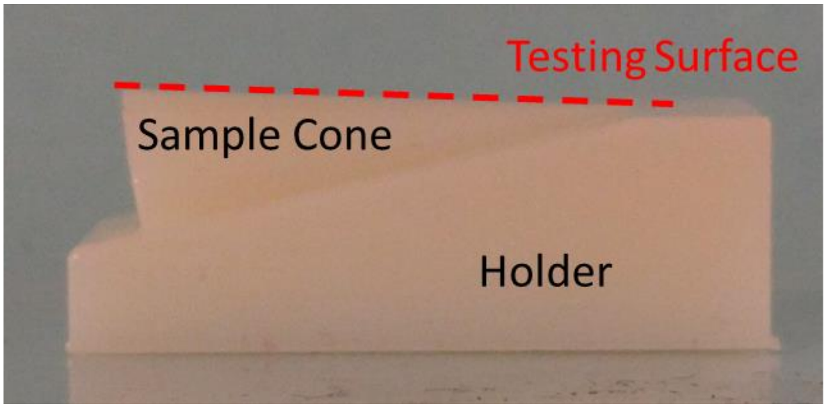

**Figure C1**: Photograph of sample holder for profilometry / Scanning Electron Microscopy (dashed red line 2.2 cm)

Scanning electron microscopy was performed using FEI Nova Nano 650 FEG SEM.

A spectrophotometer with cosine corrector and radiometric calibration (Ocean Optics, model USB 4000) was used to measure LED emission profiles and calculate the power density of emissions from all light sources. For particularly intense sources (focused LCD projector) an OD-1 filter was used.

Absorption profiles were measured on a home built pump-probe setup. The pump beam was generated by fiber coupled LED sources (Thorlabs) coupled into a multimode optical fiber terminated with an output collimator. The probe beam was produced by an incandescent light bulb source (Ocean Optics LS1) coupled into a multimode fiber with an output collimator for the light delivery to CCD collector. The pump beam was blocked after passing through the sample and the probe beam was directed by a system of lenses onto an input slit of a spectrometer (Princeton Instruments Acton SP 2150) equipped with a charge coupled device (CCD) detector (Andor Idus DV420AOE), which acquired spectra of the probe light.

Optical microscopy was performed on a Keyence VHX-5000 Microscope at 10x magnification.

Solution $^{1}H$ and $^{13}C$ nuclear magnetic resonance spectra were recorded on a Varian 600 MHz spectrometer with a regulated temperature of 25 °C.

$^{13}C$ CP-MAS nuclear magnetic resonance spectra were recorded on a Bruker 300 MHz spectrometer.

UPLC/MS was performed with a Waters UPLC Acquity equipped with a Waters LCT Premier XE Mass Detector for UPLC-HR-MS, with Waters Alliance systems (consisting of a Waters Separations Module 2695, a Waters Diode Array Detector 996 and a Waters Mass Detector ZQ 2000). Masses were recorded with a Thermo scientific LTQ Orbitrap XL mass spectrometer.

1 cm base x 2.2 cm height reference cones were printed using a variety of traditional systems:

***Stereolithography*****:** FormLabs Form 2 – Clear FLGPCL02.

***Fused Deposition Modeling*****:** Ultimaker 3 – PLA stock.

***Inkjet*****:** Stratasys Objet 30 Pro – RGD450 (matte finishing).

# Printer Setup

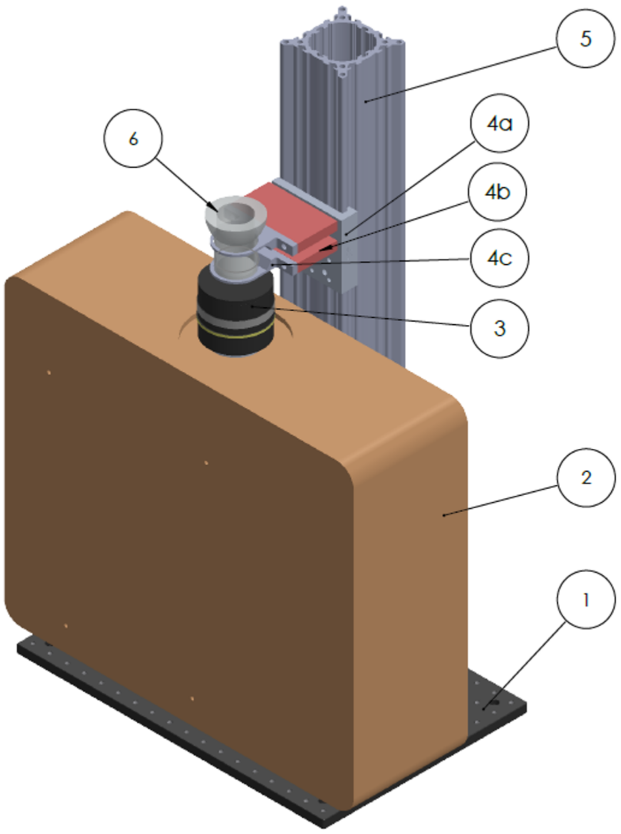

1. Aluminum Breadboard 18" x 24" x 1/2", MB1824
2. Epson 5040UB 3 LCD projector with 2.1x zoom lens *f*22.48 – 46.74
3. Zeiss Bronica Zenzanon-S lens, 105mm *f*3.5

4a. Thorlabs Drop-On Rail Carriage for 95 mm Rails, XT95P11

4b. Aluminum spacer blocks (see below, mm)

4c. 3D printed sample holder (**build models available on request**)

5. Thorlabs 95 mm Construction Rail, L = 750 mm, XT95-750 with Thorlabs Base Plate for 95 mm Rails, XT95P3
6. Glass build chamber (see below, mm)

4b

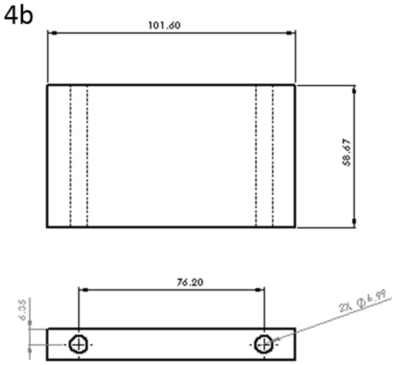

6

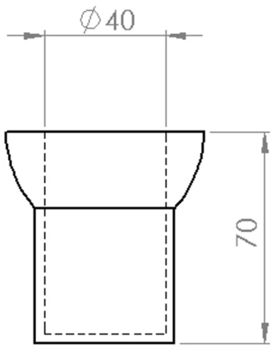

# Synthesis

## Synthesis of 1,2-bis(2-methyl-1-benzothiophen-3-yl)perfluorocyclopentene ($\text{DAE}_{530}$)

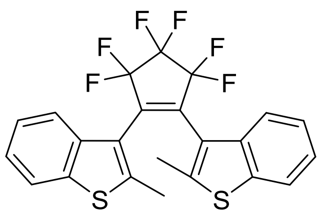

open isomer (colorless)

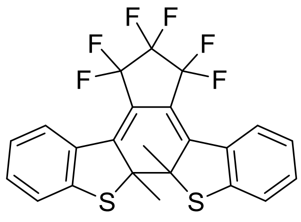

closed isomer (red color)

The synthesis of the open isomer and the corresponding closed isomer of $\text{DAE}_{530}$ was conducted according to previously reported protocols.[2–4]

## Synthesis of 1,2-bis(3-methyl-1-benzothiophen-2-yl)perfluorocyclopentene ($\text{DAE}_{470}$) – open isomer

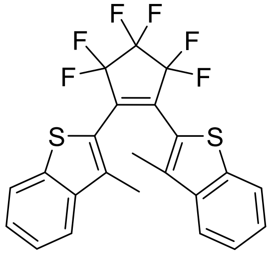

Under an argon atmosphere, 3-methyl-1-benzothiophene (0.65 mL, 5.0 mmol, 2.0 eq.) was dissolved in 20 mL of dry THF and cooled to -78 °C. After adding n-butyllithium (2.3 M solution in cyclohexane, 2.39 mL, 2.2 eq.) dropwise to the solution, the mixture was stirred for 30 min at -78 °C. Subsequently, the mixture was treated with octafluorocyclopentene (0.34 mL, 2.5 mmol, 1.0 eq.) and stirred for further 60 min at -78 °C before the reaction was quenched with 2 mL of ethanol. The crude reaction mixture was washed twice with brine (10 mL) and the organic phase was dried over $MgSO_4$. Purification by flash column chromatography ($SiO_2$; cyclohexane) provided the product (0.88 g, 1.88 mmol, 75%) as a yellow solid.

**$^1$H NMR** (500 MHz, $CDCl_3$, 25 °C): δ = 7.84–7.81 (m, 2H), 7.63–7.60 (m, 2H), 7.43–7.35 (m, 4H), 1.99 (s, 6H) ppm. **$^{13}$C{1H} NMR** (126 MHz, $CDCl_3$, 25 °C): δ = 140.87 (s), 139.28 (s), 136.11 (s), 126.32 (s), 124.71 (s), 123.16 (s), 123.10 (s), 122.49 (s), 115.76 (s), 13.39 (s) ppm. *Two carbon atoms could not be detected due to low intensity of fluorine splitting and low signal to noise ratio.* **$^{19}$F NMR** (471 MHz, $CDCl_3$, 25 °C): δ = –109.42 (t, $^3J$(F,F) = 5.4 Hz, 4F), –131.39 (p, $^3J$(F,F) = 5.4 Hz, 2F) ppm. **MS** (ESI+): m/z calculated for $C_{23}H_{14}F_6S_2$ $[M+H]^+$: 469.051, found: 469.047.

## Synthesis of 1,2-bis(3-methyl-1-benzothiophen-2-yl)perfluorocyclopentene ($DAE_{470}$) – closed isomer

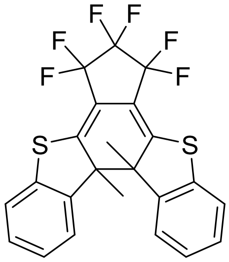

A solution of open isomer $DAE_{470}$ (2.58 g, 5.5 mmol) in 1.0 L of cyclohexane was added to a 1.5 L quartz container and placed in a Rayonet Photochemical Reactor equipped with 11x 350 nm lamps. The solution was irradiated for 40 min while stirring vigorously. After vaporation of the solvent, the residue was purified by flash column chromatography ($SiO_2$; cyclohexane) affording the closed isomer (1.20 g, 2.59 mmol, 47%) as a dark orange solid.

**$^1$H NMR** (500 MHz, $CDCl_3$, 25 °C): δ = 7.53 (d, $^3J$(H,H) = 7.81 Hz, 2H), 7.34–7.30 (m, 2H), 7.27–7.21 (m, 4H), 1.65 (s, 6H) ppm. **$^{13}$C{1H} NMR** (126 MHz, CDCl3, 25 °C): δ = 147.91 (s), 138.96 (s), 138.42 (s), 129.67 (s), 127.68 (s), 125.73 (s), 122.75 (s), 110.12 (s), 63.00 (s), 23.04 (s) ppm. *Two carbon atoms could not be detected due to fluorine splitting and low signal to noise ratio.* **$^{19}$F NMR** (471 MHz, $CDCl_3$, 25 °C): δ = –115.9 (ddt, $^2J$(F,F) = 253 Hz, $^3J$(F,F) = 5.3 Hz, $^4J$(F,F) = 5.3 Hz, 2F), –118.4 (ddt, $^2J$(F,F) = 253 Hz, $^3J$(F,F) = 5.3 Hz, $^4J$(F,F) = 5.3 Hz, 2F), –133.4 (q, $^3J$(F,F) = 5.3 Hz) ppm. **MS** (ESI+): m/z calculated for $C_{23}H_{14}F_6S_2$ $[M+H]^+$: 469.051, found: 469.052.

**General procedure for perfluoroalkyl salinization of glass:**

Glass growth chambers and slides were coated with a perfluoroalkyl self-assembled monolayer to minimize adhesion of parts. Base Piranha (2:3 Ammonium hydroxide:$H_2O_2$/30wt%$_{(aq)}$) treatment at 80 °C was accomplished for surface cleaning, followed by rinsing with MilliQ water, and drying under a stream of nitrogen. To the nitrogen flushed chamber was added toluene (40 mL, anh), followed by trimethylamine (144 µL, 1.0 mmol, anh), and trichloro(3,3,4,4,5,5,6,6,7,7,8,8,9,9,10,10,10-heptadecafluorodecyl)silane (130 µL, 0.3 mmol). A white precipitate was immediately observed, and the solution was left at room temperature of 16 hours, followed by rinsing with toluene and ethanol, sonicating in ethanol for 1 minute, and drying under a stream of nitrogen.

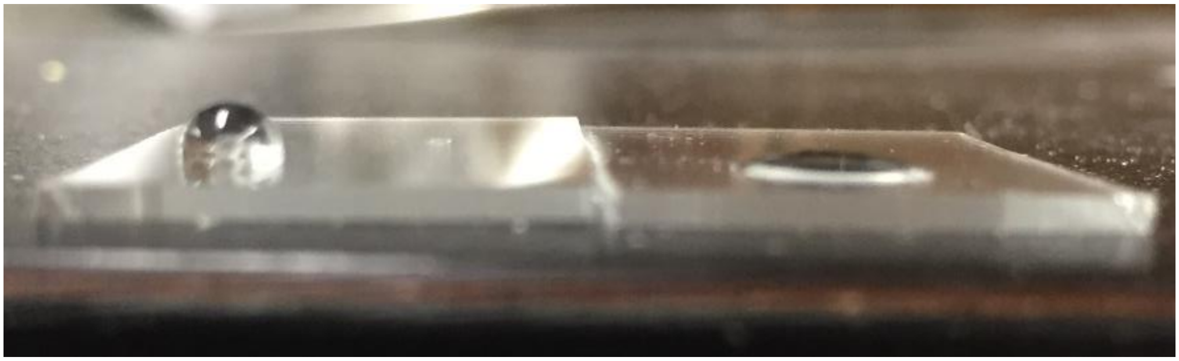

**Figure C3**. Images showing a water droplet on perfluoroalkyl functionalized (left) and bare (right) glass substrates. Contact angle for the coated surface was measured to be approximately 115°.

**Synthesis of (3-ethyloxetan-3-yl)methyl acrylate:**

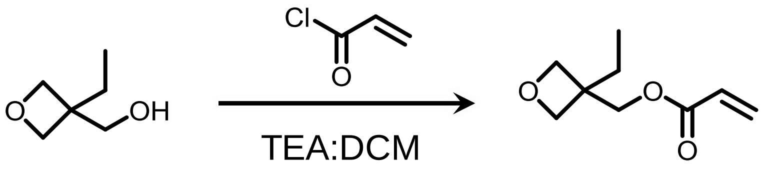

OXA OXA-acrylate

To a dry 2-neck 250 mL round bottom flask equipped with a magnetic stir bar and septum was added (3-ethyloxetan-3-yl)methanol (10 g, 86 mmol), dichloromethane(100 mL, anh) and triethylamine (24 mL, 172 mmol). The mixture was degassed with argon for 10 minutes and cooled to 0 °C, followed by addition of acryloyl chloride (8.4 mL, 103 mmol) using a syringe. The reaction mixture was stirred at 0 °C for 10 minutes under argon then allowed to warm to room temperature and stirred for an additional two hours. The reaction mixture was quenched with methanol, pured into diethyl ether, filtered, and distilled under reduced pressure (40 °C), providing the desired product as a clear, colorless liquid (12.8 g, 87% yield). **$^1$H NMR** (600 MHz, $CDCl_3$) δ 6.43 (dd, J = 17.3, 1.3 Hz, 1H), 6.15 (dd, J = 17.4, 10.4 Hz, 1H), 5.86 (dd, J = 10.5, 1.3 Hz, 1H), 4.50 (d, J = 6.1 Hz, 2H), 4.42 (d, J = 6.1 Hz, 2H), 4.30 (s, 2H), 1.77 (q, J = 7.5 Hz, 2H), 0.92 (t, J = 7.5 Hz, 3H). **$^{13}$C NMR** (101 MHz, $CDCl_3$) δ 166.19, 131.27, 128.09, 77.87, 66.38, 42.65, 26.89, 8.17. IR (ATR) v 2956, 2862, 1718, 1630, 1614, 1455, 1403, 1379, 1292, 1262, 1176, 1054, 976, 823, 806, 784 $cm^{-1}$. **LRMS** (+ESI): m/z calculated for $C_9H_{15}O_3$ $[M + H]^+$ 171.10, found 171.11.

## Resin formulations

The multi-component photoactive resin (monomer, crosslinker, photosensitizer, accelerator, initiator, and photoswitch) were mixed in an amber vial in the absence of light, and sonicated until the solution was homogeneous.

Note 1 – see above materials section for a full list of chemical names and acronyms.

Note 2 – all components are given as weight percent (wt%) relative to total monomer + crosslinker.

- Acrylamide formulation (**Resin G1**, Green LED): DMA:BDA (70:30), H-Nu 535 (0.04 wt%), Borate (0.2 wt%), H-Nu 254 (0.2 wt%), $DAE_{530}$ (8 mM).
- Methyl acrylate formulation (**Resin G2**,Green LED): MA:TEGDA (99.5:0.5), H-Nu 535 (0.02 wt%), Borate (0.1 wt%), H-Nu 254 (0.1 wt%), $DAE_{530}$ (8 mM).
- Epoxy formulation (**Resin B1**,Blue LED): ECC:OXA (80:20), CQ (0.4 wt%), EDMAB (0.4 wt%), H-Nu 254 (0.8 wt%), $DAE_{470}$ (10 mM).
- Butyl acrylate formulation (**Resin B2**, Blue LED): BA:TEGDA (99.5:0.5), CQ (0.4 wt%), EDMAB (0.4 wt%), H-Nu 254 (0.8 wt%), $DAE_{470}$ (10 mM).
- Methyl acrylate formulation (Blue LED): MA:TEGDA (99.5:0.5), CQ (0.4 wt%), EDMAB (0.4 wt%), H-Nu 254 (0.8 wt%), $DAE_{470}$ (10 mM).
- Epoxy-acrylate formulation (Blue or Green LED): Combination of **Resin G2** and **Resin B1**, except additional TEGDA crosslinker is added to achieve 0.5 wt% in the final resin.

## Curing and isolation procedures

A perfluoroalkyl functionalized glass slide is adhered to the bottom of the build chamber using a high viscosity fluorinated oil (XHT-500). The chamber is sealed with a septum and purged with Argon. The resin of interest is sparged with oxygen and ~3.5 mL of resin is transferred into the build chamber. The build chamber is placed over the projector and exposed to a digital image.

**G1:** 2 minute exposure to green light, followed by removal from the build plate with a razor blade. The specimen was retrieved and placed in an oxygen free environment and postcured under a compact fluorescent lamp for 30 minutes.

**G2:** 5 minute exposure to green light, followed by removal from the build plate with a razor blade. The specimen was retrieved and placed in an oxygen free environment and postcured under a compact fluorescent lamp for 30 minutes. Residual monomer was removed through Soxhlet extraction with acetone overnight and drying *in vacuo*.

**B1:** 2 minute exposure to blue light, followed by removal from build plate with razor blade. Retrieved specimen placed in oxygen free environment and postcured under a simple white light lamp for 30 minutes.

**B2:** 5 minute exposure to blue light, followed by removal from the build plate with a razor blade. The specimen was retrieved and placed in an oxygen free environment and postcured under a compact fluorescent lamp for 30 minutes. Residual monomer was removed through Soxhlet extraction with acetone overnight and drying *in vacuo*.

**B1:G2 mixed resins:** 8 minute exposure to blue segments (if applicable) and 2 minute exposure to entire image as a green block, followed by removal from the build plate with a razor blade. Residual monomer was removed through dialysis in 1:1 acetone:isopropanol followed by washing with isopropanol prior to drying in air. For mechanical studies, blue samples were postcured for 30 minutes under a compact fluorescent lamp.

## Characterization

### Spectral outputs of light sources

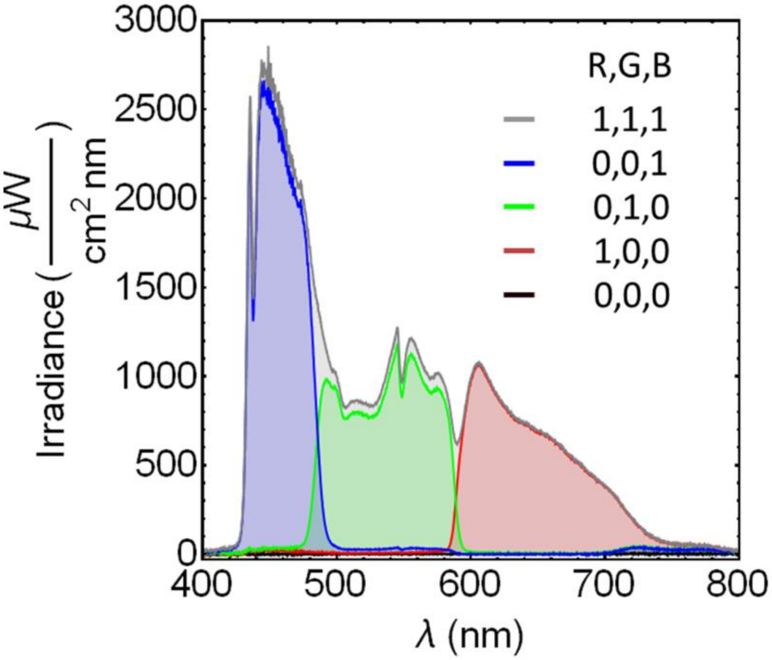

**Figure C4:** Projector outputs (measured through OD1 filter).

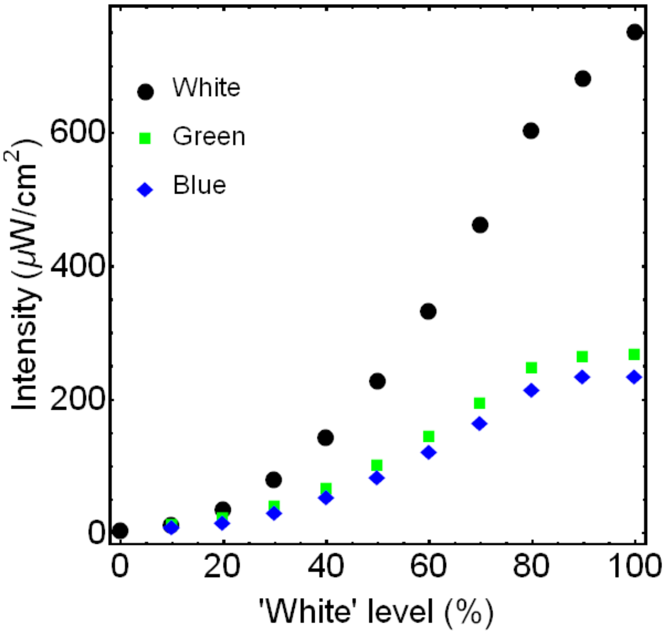

**Figure C5:** Integrated intensities of projector as a function of white level for different color objects impingent on growth chamber.

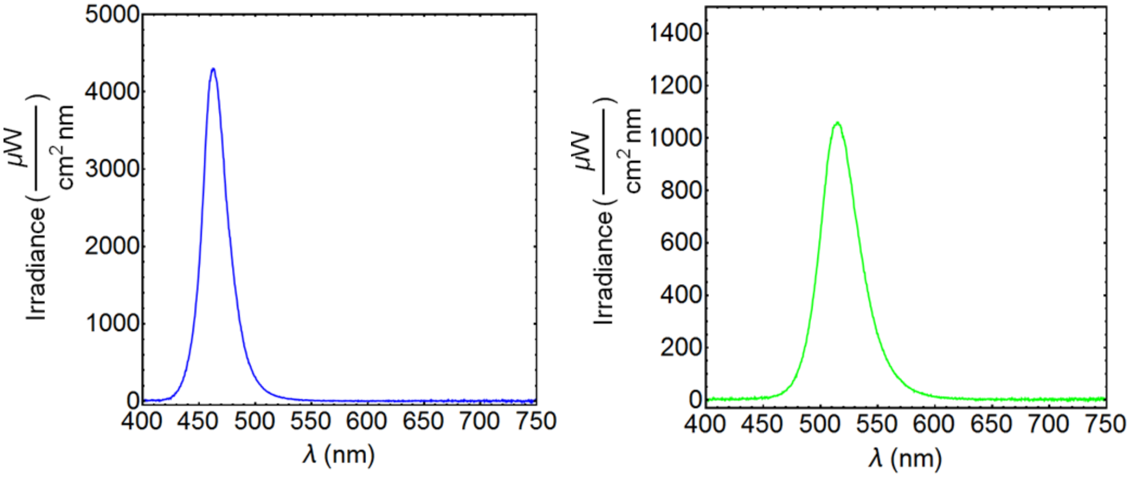

**Figure C6:** Spectral outputs of (left) 470 nm and (right) 530 nm fiber coupled LEDs.

| | |
|---|---|
| 470 nm | Integrated Intensity: 130 mW/cm$^2$ |
| 530 nm | Integrated Intensity: 48 mW/cm$^2$ |

### Relevant absorption profiles

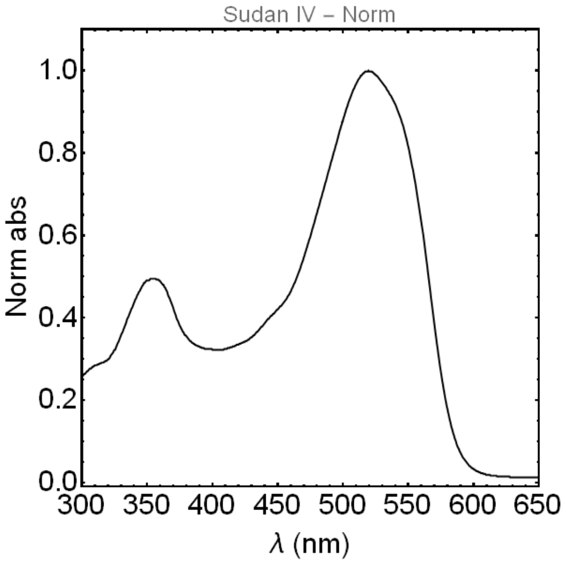

**Figure C7:** Normalized absorption profile for nonbleaching Sudan IV (nonbleaching control dye). Extinciton coefficient ~26000 $M^{-1}cm^{-1}$ at 520 nm.

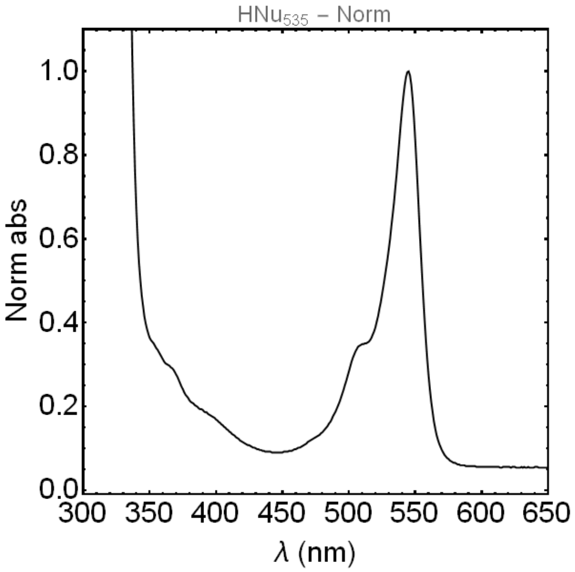

**Figure C8:** Normalized absorption profile for $HNu_{535}$ photoinitiator. Extinciton coefficient ~91000 $M^{-1}cm^{-1}$ at 545 nm.

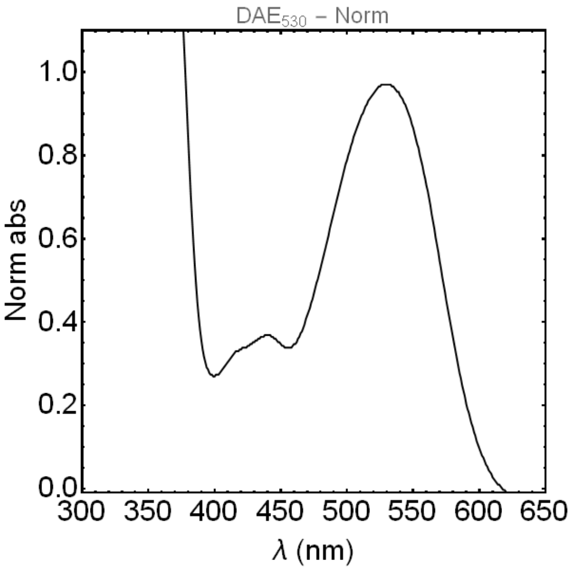

**Figure C9:** Normalized absorption profile for DAE530 photochromic molecule (solution mask). Extinciton coefficient ~30000 M$^{-1}$cm$^{-1}$ at 530 nm.

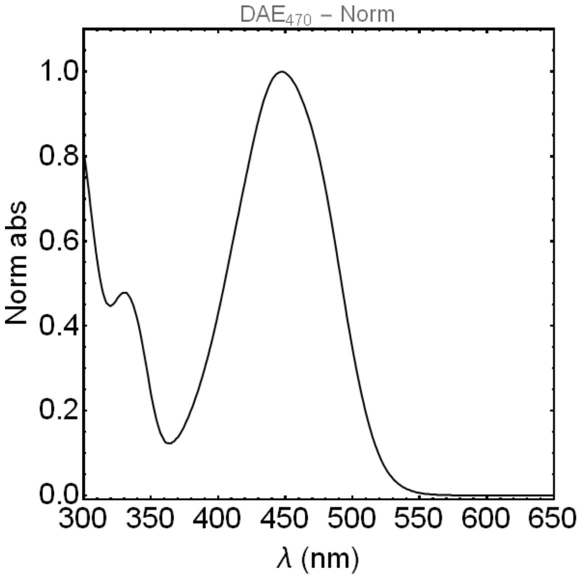

**Figure C10:** Normalized absorption profile for DAE470 photochromic molecule (solution mask). Extinciton coefficient ~9000 M$^{-1}$cm$^{-1}$ at 450 nm.

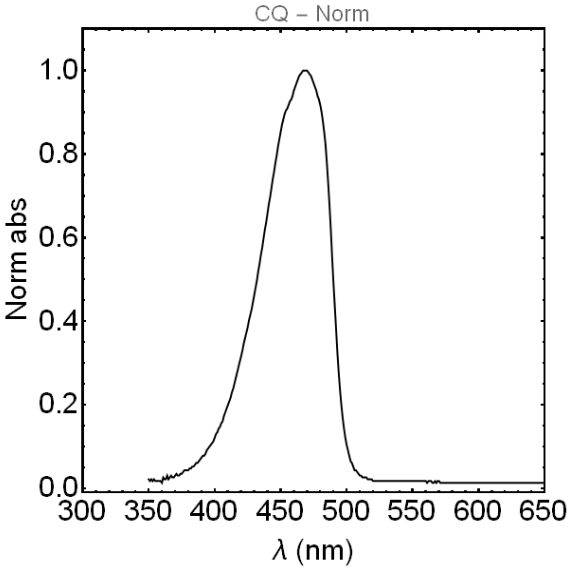

**Figure C11:** Normalized absorption profile for camphorquinone photoinitiator. Extinciton coefficient ~50 $M^{-1}cm^{-1}$ at 470 nm.

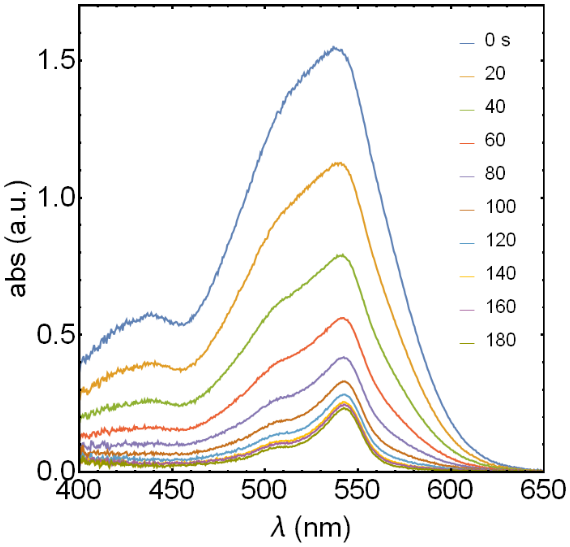

**Figure C12:** Time lapse absorption profiles for a 'masked' $HNu_{535}$ in the presence of $DAE_{530}$ exposed to fiber coupled 530 nm LED on a pump-probe setup. Complete switching of $DAE_{530}$ allows the $HNu_{535}$ photoinitiating system to absorb light.

## Frontal growth measurements

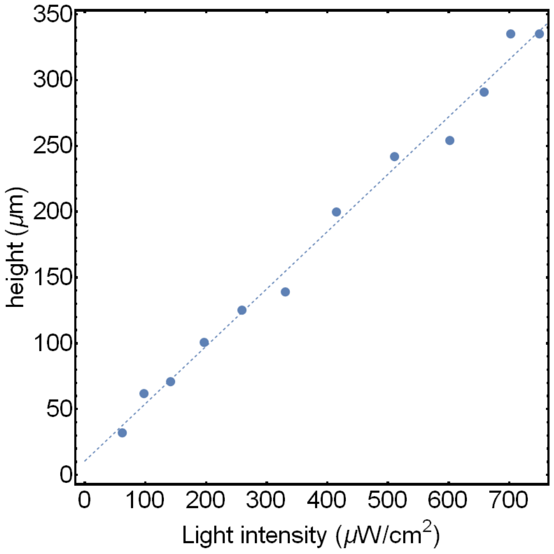

**Figure C13:** Heights of 5 mm diameter parts created by exposure to 800 ms of white projector light at various light intensities. Linear relationship expected from **Equation 1** (manuscript).

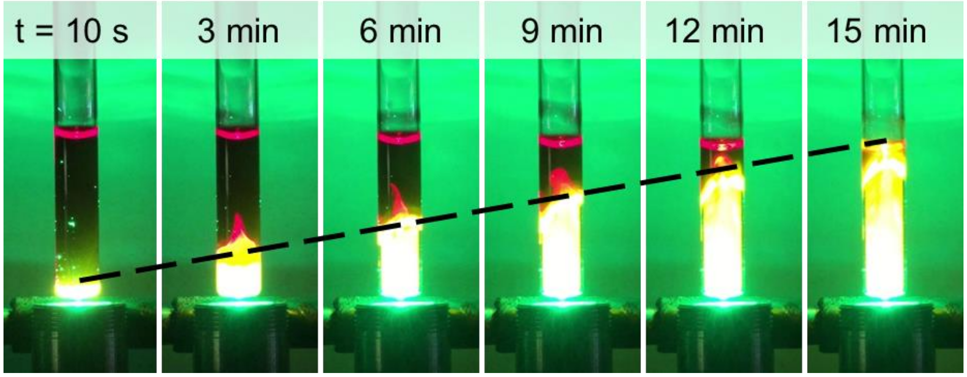

**Figure C14:** Sample of **G1** in a flat bottom NMR tube (5 mm tube diameter) exposed to a collimated fiber coupled 530 nm LED. Clear linear frontal behavior can be seen as predicted by **Equation 1** (manuscript).

### Dye controls, Cure Depth, and Resolution

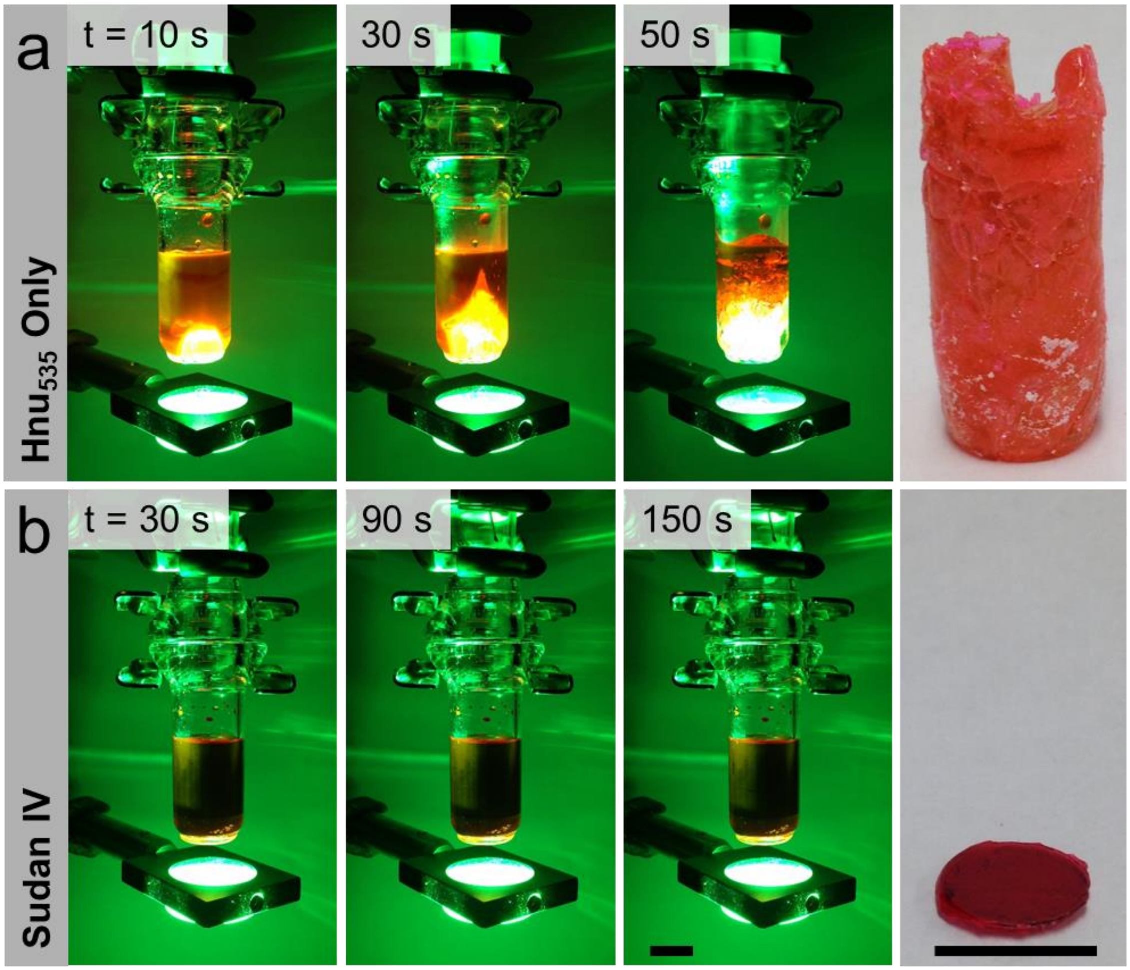

**Figure C15:** a) A control study where no photoabsorber is added to a HNu535 sensitized resin above a focusing lens. The reaction proceeds rapidly and exothermicaly, with no obervable spatial control. b) A control study where the photosTable Cudan IV dye is added to the same HNu535 sensitized resin. With the resulting attenuation of light, only a thin disc was cured.

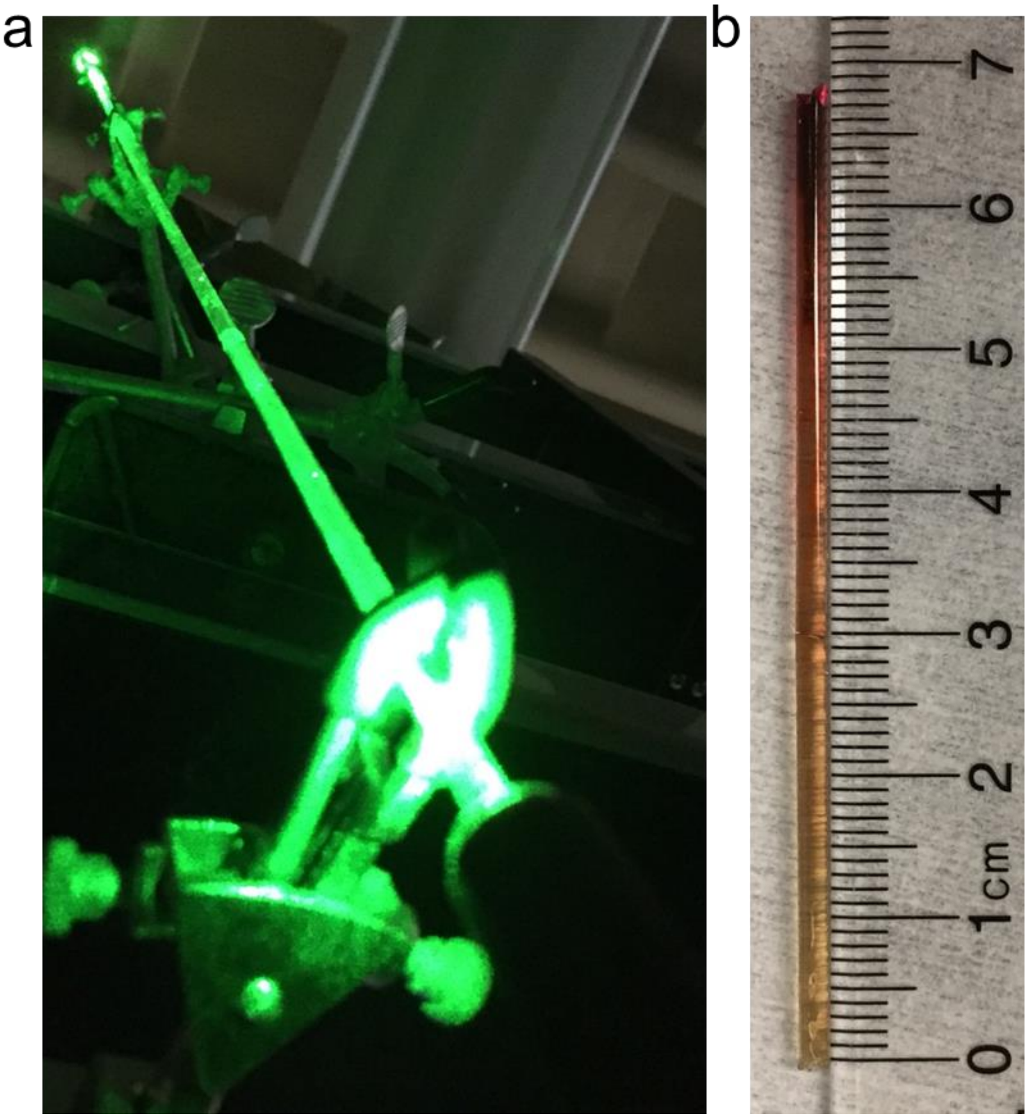

**Figure C16:** a) Experimental setup for cure depth experiment, a ~2 mm inner diameter tube filled with ~10 cm of resin is exposed to 532 nm light from a green laser pointer. b) Result after 6 hours of exposure, providing a depth of cure exceeding 6.5 cm.

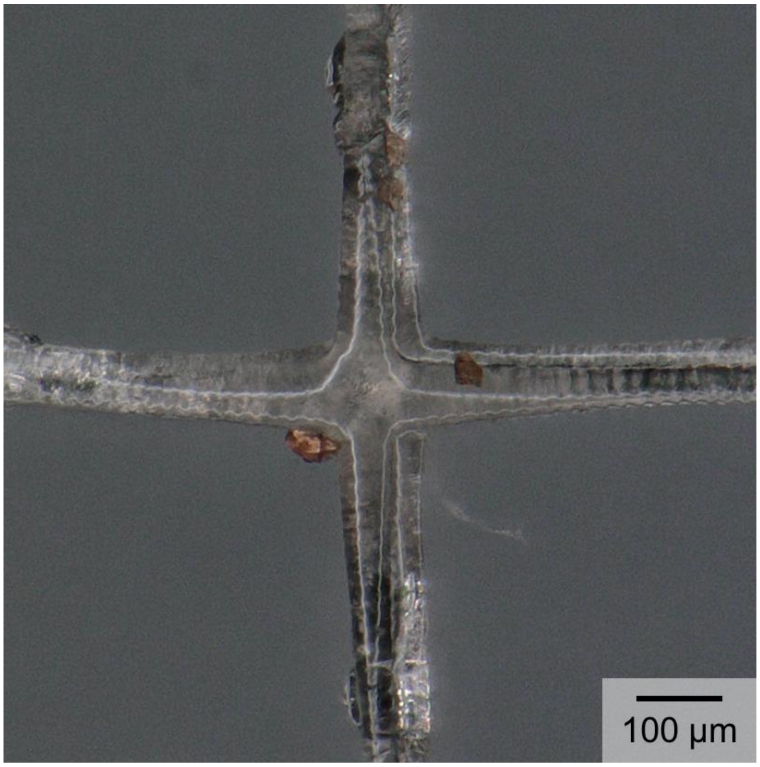

**Figure C17:** Cross pattern formed by exposure of **G1** to a cross of 0.1 pt lines using the setup outlined in **Figure C2**. The formed object demonstrates lateral resolution of 90 microns.

## Surface Characterization (Profilometry / SEM)

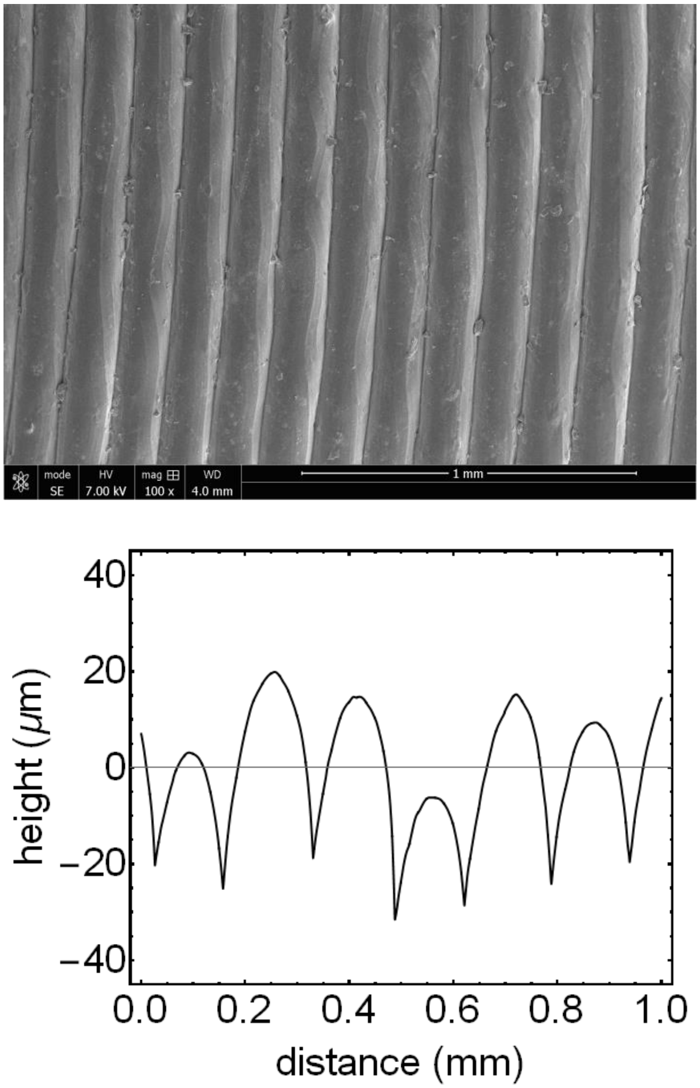

**Figure C18:** Surface analysis of fused deposition modeling – produced cone samples through Scanning Electron Microscopy (top) and profilometry (bottom). Build direction horizontal. FDM parts demonstrate large rounded layer features with regular periodicity.

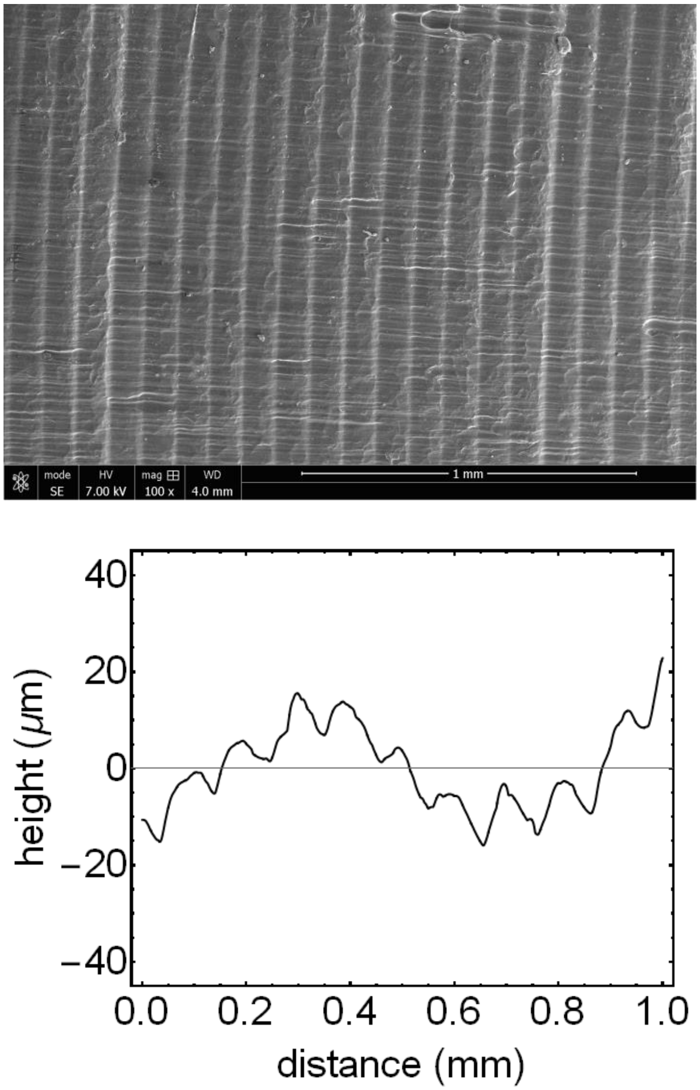

**Figure C19:** Surface analysis of stereolithography – produced cone samples through Scanning Electron Microscopy (top) and profilometry (bottom). Build direction horizontal. SLA parts demonstrate sharp layer features with regular periodicity. (Note: waviness due to difficulties aligning rounded cone sample for analysis)

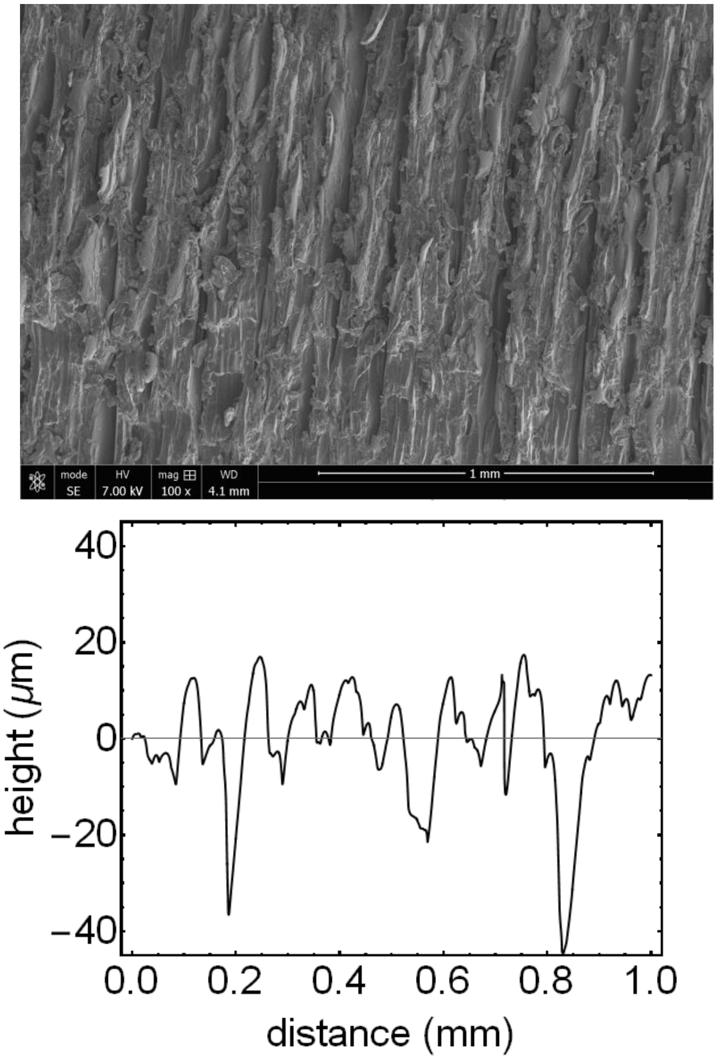

**Figure C20:** Surface analysis of inkjet – produced (using 'matte' setting) cone samples through Scanning Electron Microscopy (top) and profilometry (bottom). Build direction horizontal. FDM parts demonstrate large rounded layer features with regular periodicity.

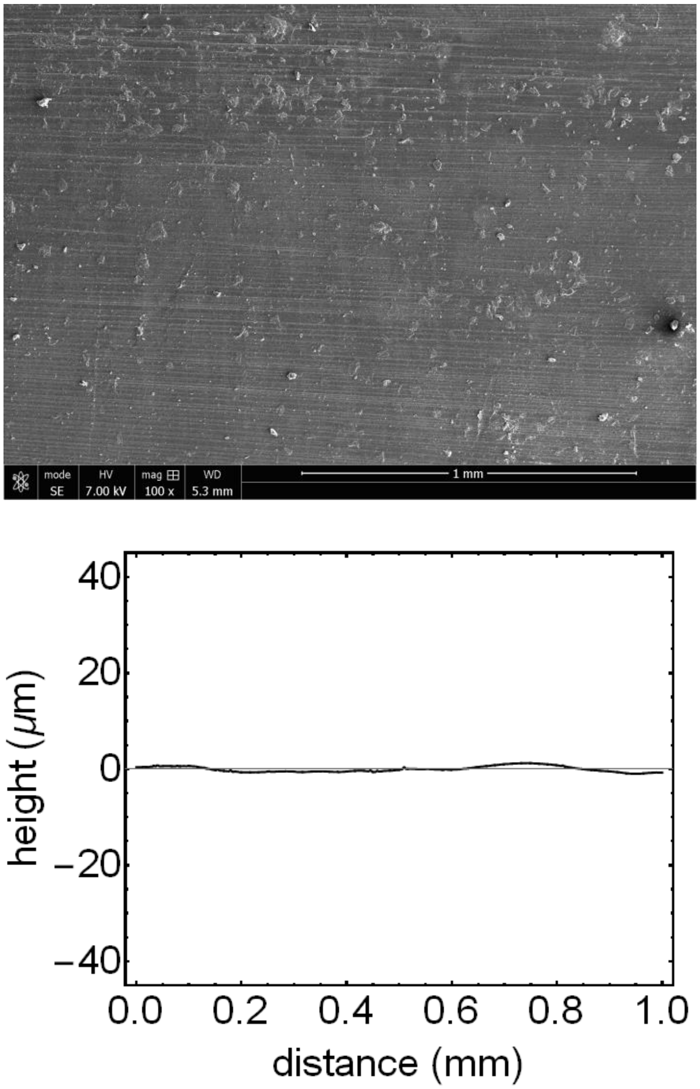

**Figure C21:** Surface analysis of SMaLL – produced cone samples through Scanning Electron Microscopy (top) and profilometry (bottom). Build direction horizontal. SMaLL parts show no observable layering in the build direction, but some evidence of parallel-running surface defects. See bulk images.

## Analysis of 3D printed parts (interior)

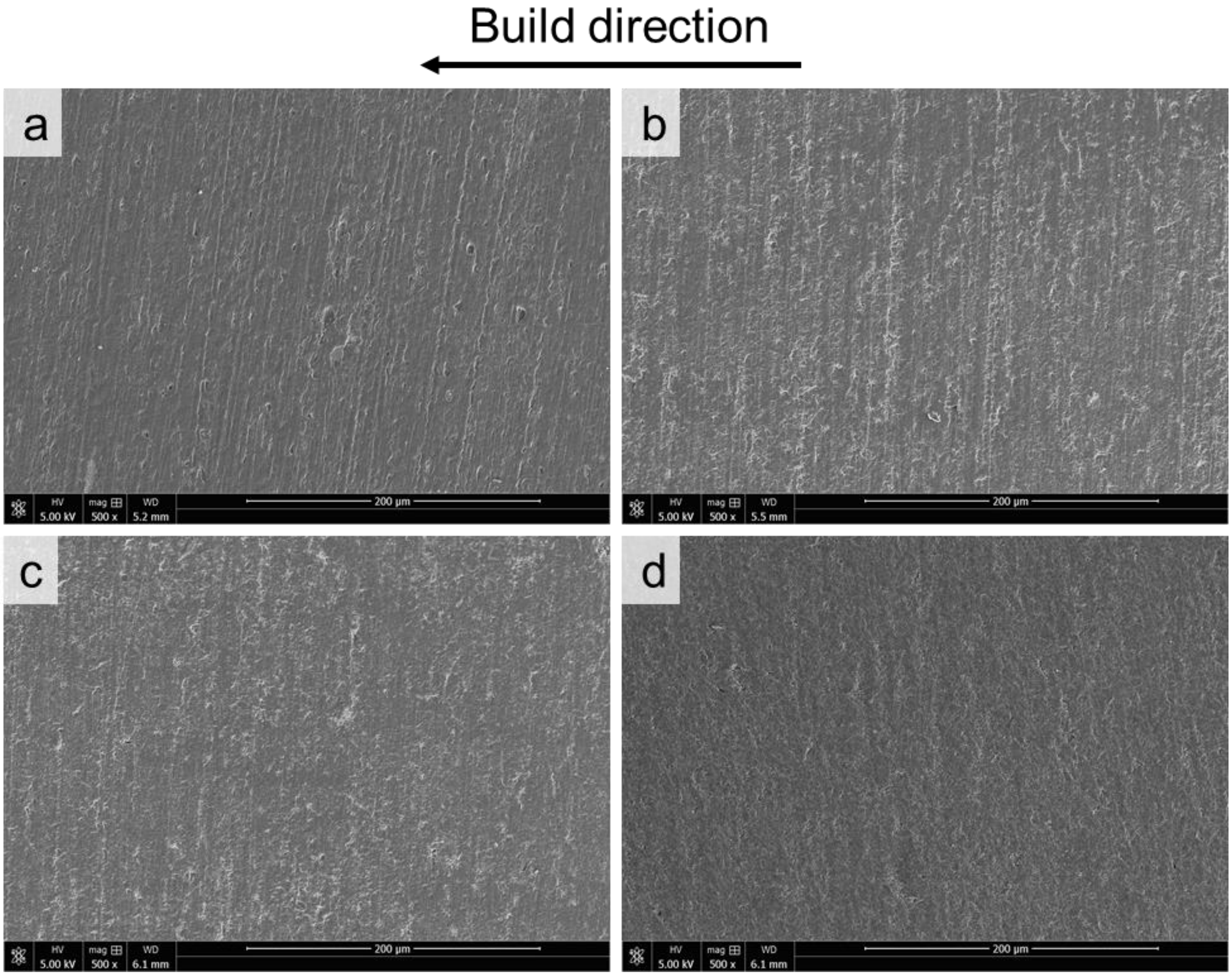

**Figure C22:** Scanning electron microscope images of bulk sample morphology of 3D printed cones (accomplished by polishing to a grit of 1200) by a) FDM, b) SLA, c) Inkjet, and d) SMaLL. Layering oriented perpendicular to build direction apparent for a-c but no discernable layering is observed for the SMaLL samples.

### Part growth using dynamic stage

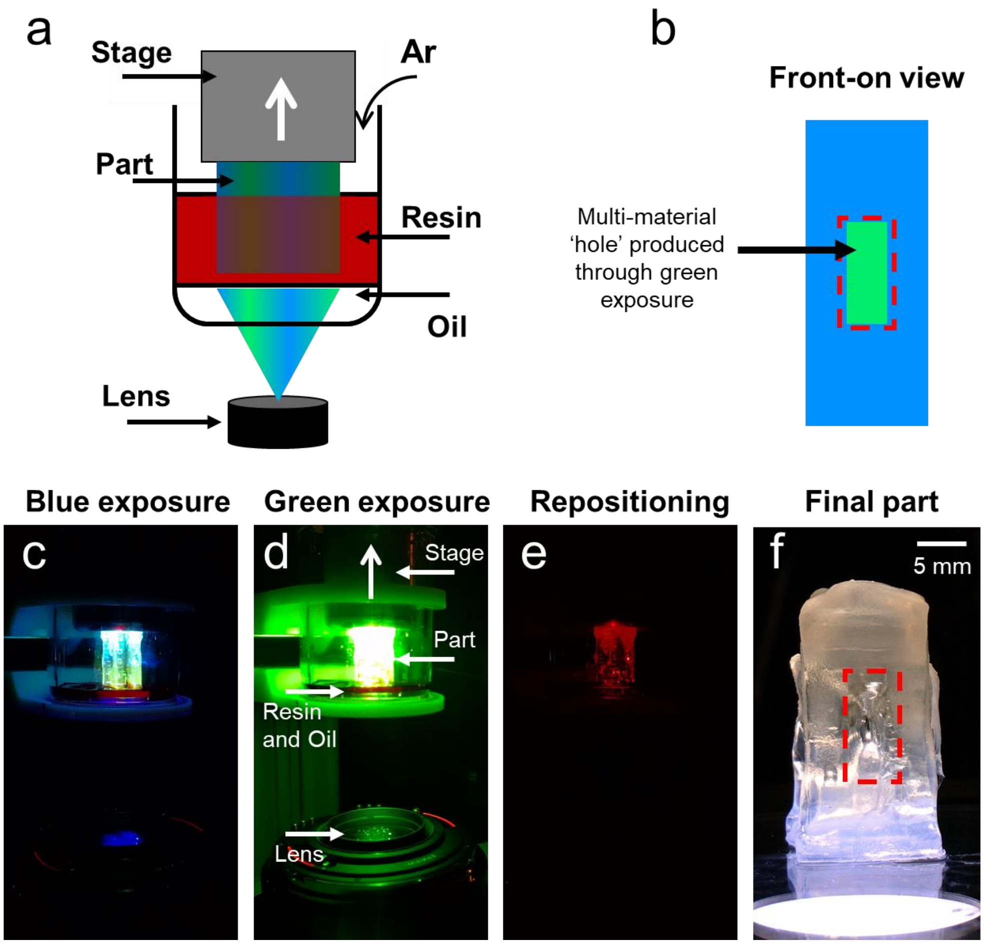

**Figure C23:** Dynamic printing of 1:1 **B1**:**G2** a) Schematic of setup used to produce parts using a mechanical stage. Stage was moved in 100 µm incremenets to produce a part with b) a central hole composed of **G2**. Photographs of c) blue exposure d) green exposure (labeled) and e) stage repositioning steps. f) The final multi-material part produced with a 'soft' green hole through the center of the face highlighted in dashed red box (swollen with acetone to accentuate **G2** regions).

## Mechanical Properties

### Hardness

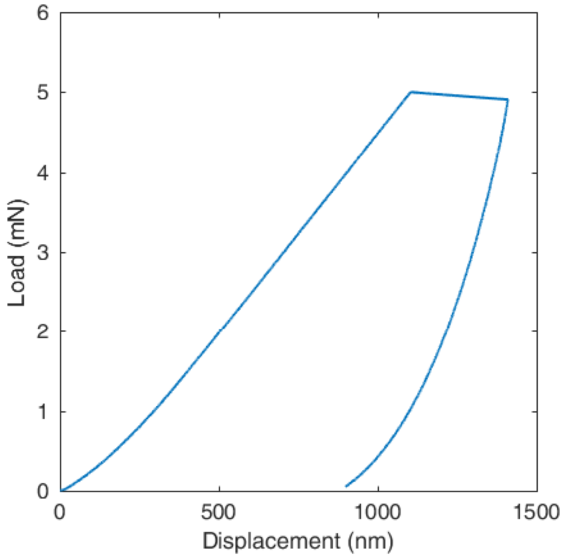

**Figure C24:** Representative hardness data from nanoindentation of **G1** samples.

> 30 individual indents measured

| | |
|---|---|
| Hardness: | 74 ± 3 MPa |
| Modulus: | 2.0 ± 0.1 GPa |

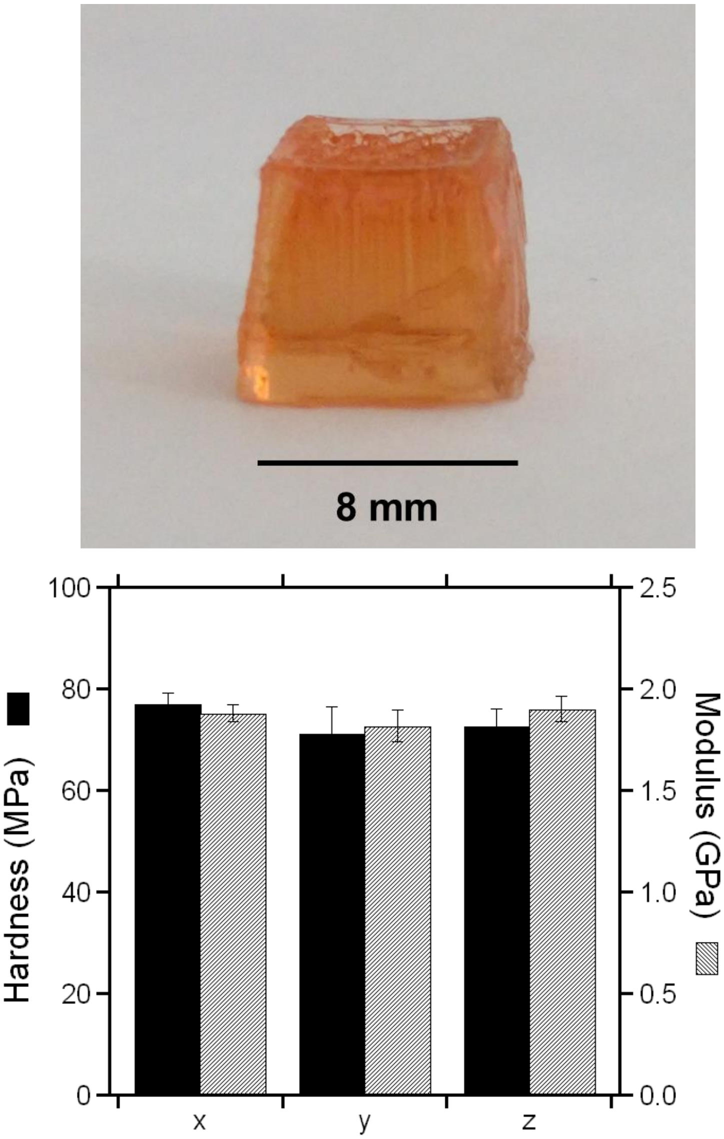

**Figure C25:**

Top) Photograph of 8 mm cube (**G1**) tested along faces *via* nanoindentation

Bottom) Hardness data from 3 directions along DMA cube produced via SMaLL after 30 minutes of postcuring. The data shows no significant variation in hardness or modulus along the faces (> 10 indents per face) and is consistent with previous DMA experiments.

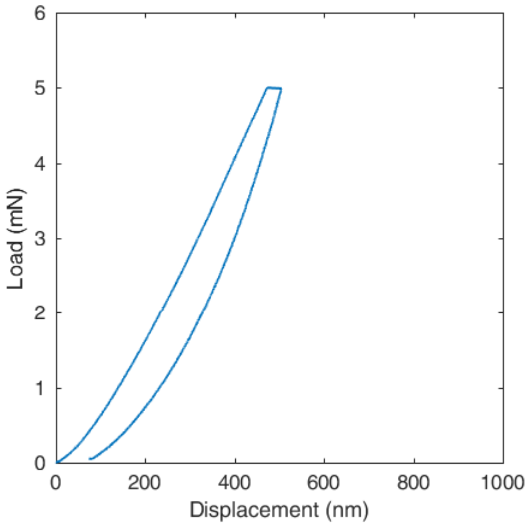

**Figure C26:** Representative hardness data from nanoindentation of **B1** samples.

> 30 individual indents measured

Hardness: 241 ± 4 MPa Modulus: 3.5 ± 0.2 GPa

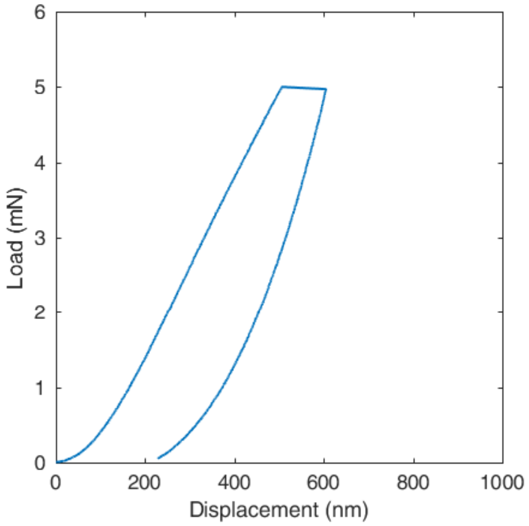

**Figure C27:** Representative hardness data from nanoindentation of 3:1 **B1:G2** samples after exposure to blue light and post curing for 30 minutes.

> 30 individual indents measured

Hardness: 175 ± 9 MPa Modulus: 3.5 ± 0.1 GPa

## Tensile measurements

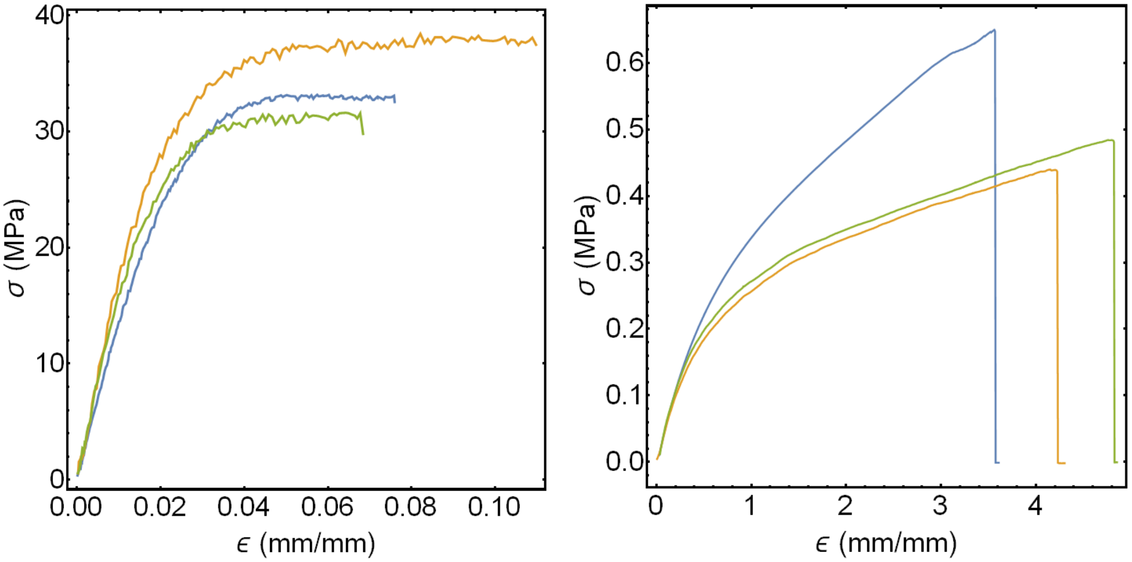

**Figure C28:** Tensile meaurements of **G1** (left) and **G2** (right) samples.

**G1**

Modulus: 1.6 ± 0.3 GPa

Ultimate Strain: 0.09 ± 0.02

**G2**

Modulus: 500 ± 5 kPa

Ultimate Strain: 4.2 ± 0.6

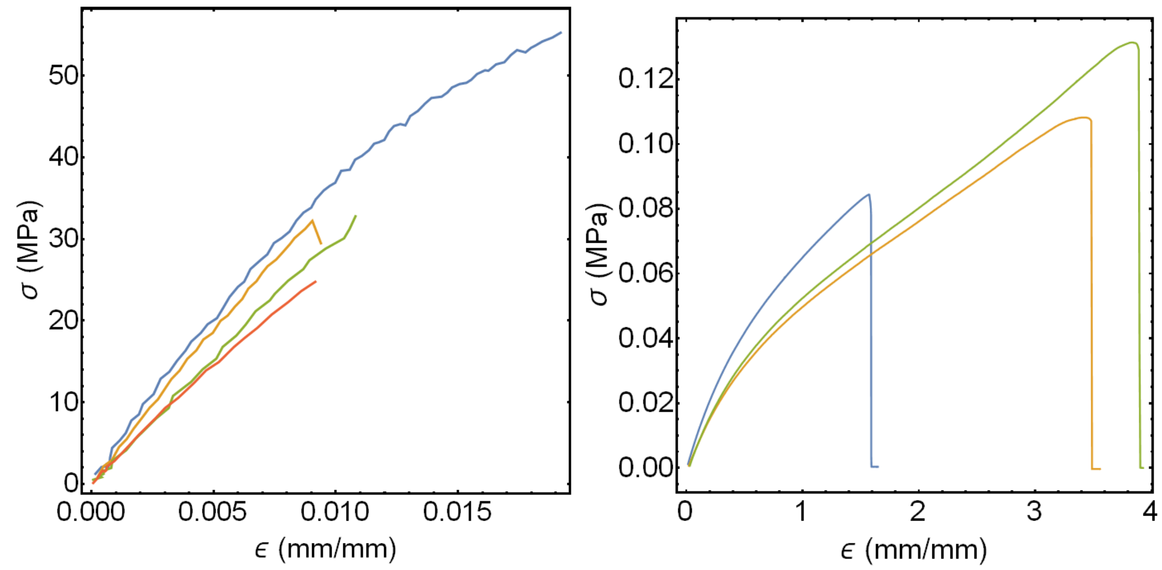

**Figure C29:** Tensile meaurements of **B1** (left) and **B2** (right) samples.

Modulus: 3.5 ± 0.6 GPa

Ultimate Strain: 0.013 ± 0.001

Modulus: 100 ± 15 kPa

Ultimate Strain: 3 ± 1.2

## Multi-material Properties

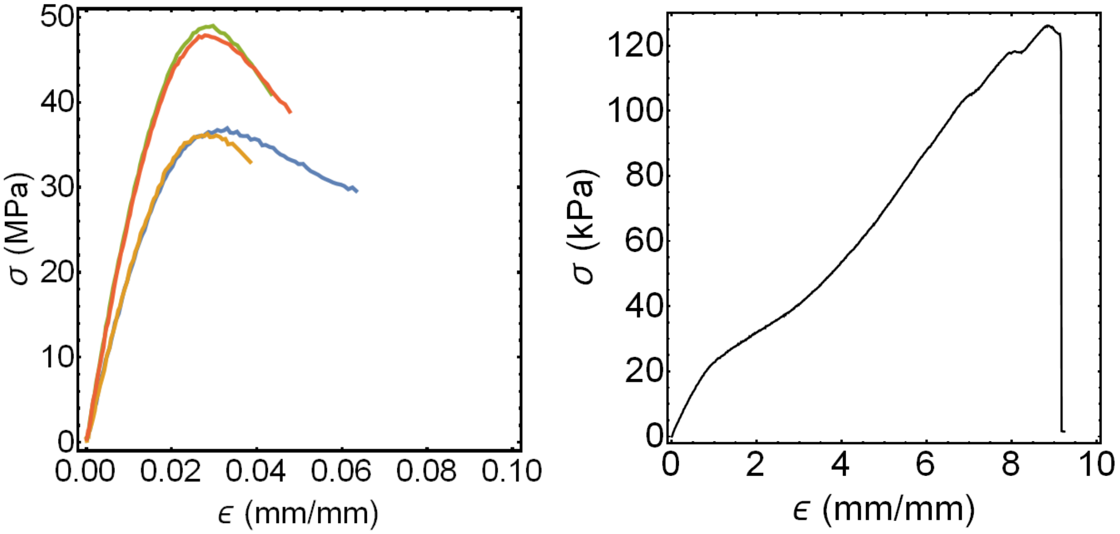

**Figure C30:** Left) Tensile meaurements of 3:1 **B1:G2** samples after 470 nm irradiation and 30 minutes of postcuring. The interpenetrating network produced from the blue exposure gives a signature yielding behavior for these samples. Right) Tensile meaurements of 3:1 **B1:G2** samples after 530 nm irradiation, yielding soft highly extensible materials.

470 nm irradiation

Modulus: 2.25 ± 0.37 GPa

Ultimate Strain: 0.05 ± 0.01

530 nm irradiation

Modulus: 28 kPa

Ultimate Strain: 9.1

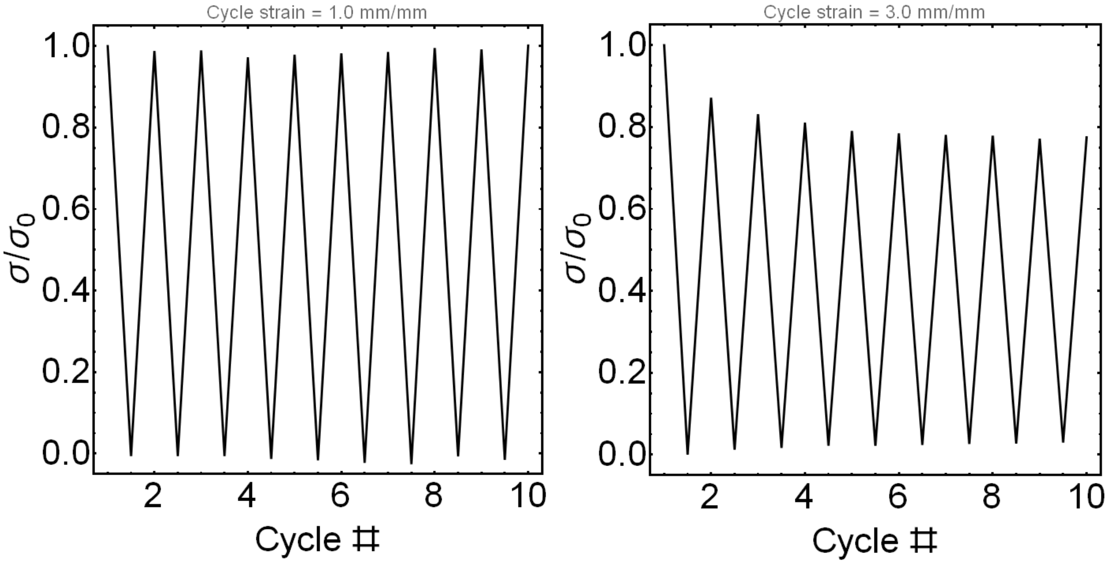

**Figure C31**: Results from cyclic tensile measurements to strains of left) 100% and right) 300%. Strains of 100% show ideal elastic behavior, however strains of 300% show initial losses, but level out to ~80% of initial stresses after 5 strain cycles.

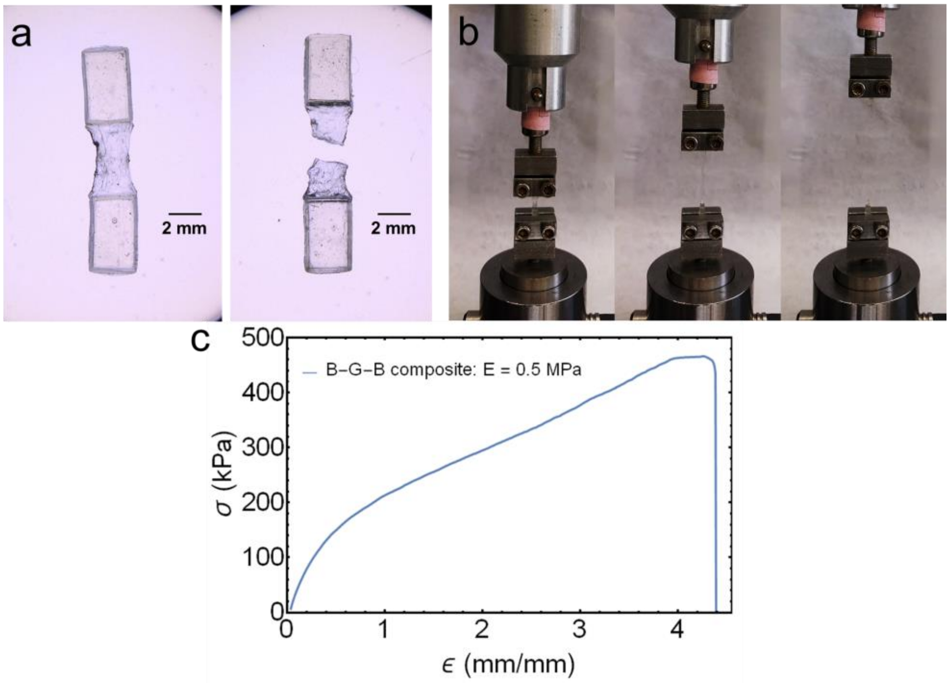

**Figure C32**: a) Micrographs of multimaterial tensile bars printed using a 1:1 **B1**:**G2** resin before (left) and after (right) testing demonstrating that failure does not occur at the blue-green interface. b) Photographs of tensile test to failure (far right). c) Stress-strain curve of the blue-green-blue material, demonstrating nearly identical properties to pure **G2**.

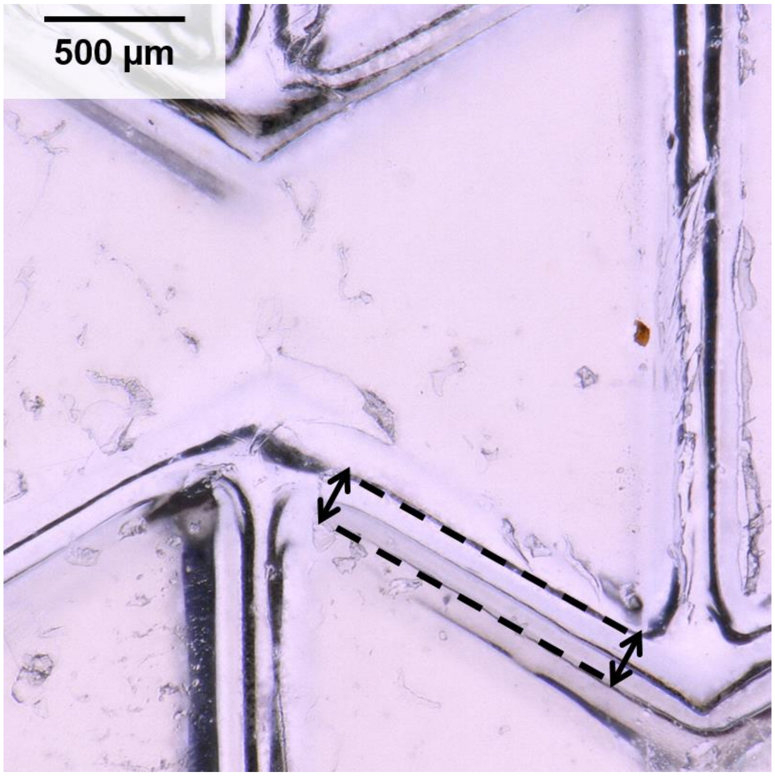

**Figure C33:** 100x optical micrograph of intermaterial gaps in a dried bowtie sample, demonstrating intermaterial resolution of approximately 200 microns (denoted by dashed lines and arrows).

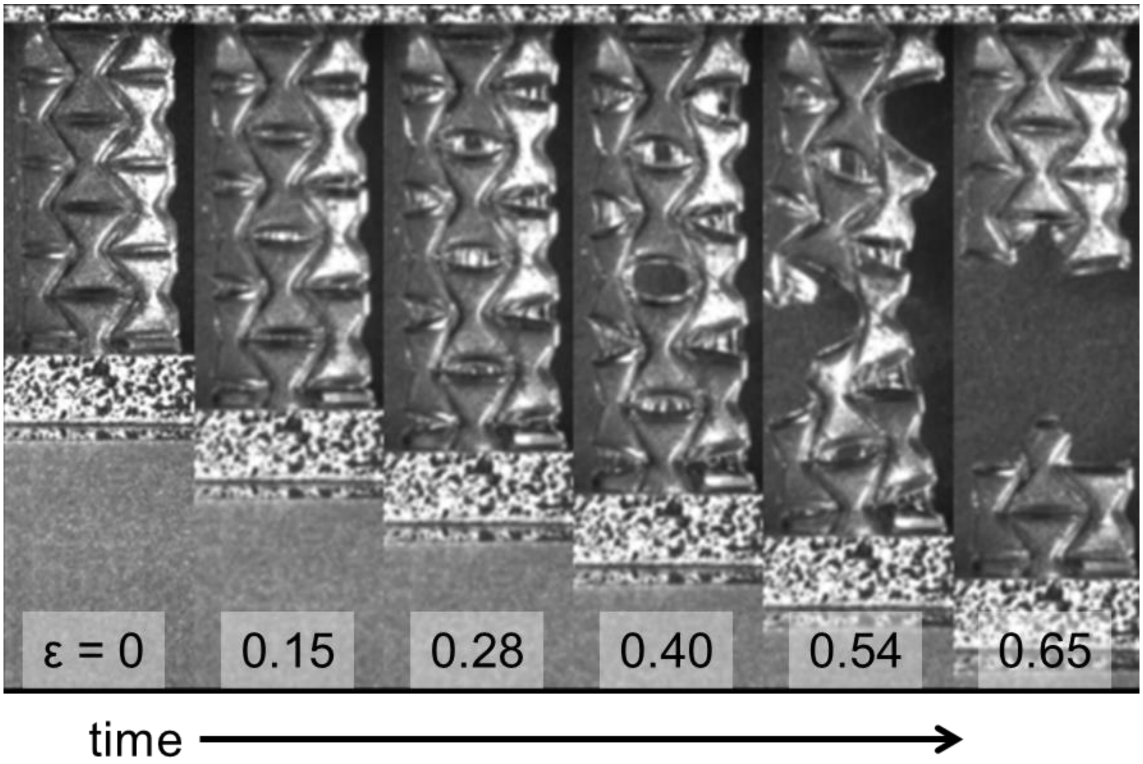

**Figure C34:** Images of brick-and-mortar bowtie material at various strains. Failures (voids and cracks) begin to occur at strains ~0.40 throughout the specimen, eventually bridging together to cause complete material failure.

## References

(1) Briscoe, B. J.; Fiori, L.; Pelillo, E. Nano-Indentation of Polymeric Surfaces. *J. Phys. D. Appl. Phys.* **1998**, *31* (19), 2395–2405.

(2) Hanazawa, M.; Sumiya, R.; Horikawa, Y.; Irie. Thermally Irreversible Photochromic Systems. Reversible Photocyclization of 1,2-Bis( 2-Methyl Benzo[b]Thiophen-3-Yl)Perfluorocycloal Kene Derivatives. *J. Chem. Soc., Chem. Commun.* **1992**, *0*, 206–207.

(3) Mamiya, J. I.; Kuriyama, A.; Yokota, N.; Yamada, M.; Ikeda, T. Photomobile Polymer Materials: Photoresponsive Behavior of Cross-Linked Liquid-Crystalline Polymers with Mesomorphic Diarylethenes. *Chem. - A Eur. J.* **2015**, *21* (8), 3174–3177.

(4) Dolinski, N. D.; Page, Z. A.; Eisenreich, F.; Niu, J.; Hecht, S.; Read de Alaniz, J.; Hawker, C. J. A Versatile Approach for In Situ Monitoring of Photoswitches and Photopolymerizations. *ChemPhotoChem* **2017**, *1* (4), 125–131.